WEAK-INTENSITY, BASALTIC, EXPLOSIVE VOLCANISM:

DYNAMICS OF HAWAIIAN FOUNTAINS

A DISSERTATION SUBMITTED TO THE GRADUATE
DIVISION OF THE UNIVERSITY OF HAWAIʻI AT MĀNOA IN
PARTIAL FULFILLMENT FOR THE DEGREE REQUIREMENTS OF

DOCTOR OF PHILOSOPHY

IN

GEOLOGY AND GEOPHYSICS

MAY 2013

By

Carolyn Parcheta

Dissertation committee:

Bruce Houghton (Chairperson)
Don Swanson
Sarah Fagents
Scott Rowland
Francis Sansone

Dedication

I would like to dedicate this dissertation to anyone who has had a long-term dream, and pushed to not only pursue it, but also achieve it. Since late childhood, I had wanted to earn a Ph. D., and during my early adolescence, I consciously chose to pursue volcanology as a career path. This dissertation is a testament to the dedication, determination, persistence, patience, enthusiasm, creativity, humbleness, and humility needed to achieve such a long-term goal. The qualities listed above are certainly not comprehensive, nor did I have all of them at the start of this endeavor… but they are the ones that I acquired along this journey and relied upon most frequently. The last five years have molded me in to a methodical, systematic scientist and allowed me to truly appreciate my environment, my colleagues, and the profoundness of passion. To those out there who have made their own dreams come true, you have been my inspiration and my guiding force. To those out there who are still dreaming, but ready to begin their journey, I believe that you can do it.

I would also like to dedicate this dissertation to my late uncle, Mike Parcheta, who passedaway a month after the oral defense of this work. He had plenty of enthusiasm and support for my degree. I appreciated that he brought to me his natural curiosity about how and why the earth does what it does. His constant dialogue and good humor will be missed.

Acknowledgements

Many people have helped me in achieving this degree, and I am truly appreciative of all the support, guidance, and inspiration.

First and foremost, I thank my adviser, Dr. Bruce Houghton, for teaching me about field, lab, and vesicle techniques in volcanolog. In addition, he provided opportunities and encouragement for volcanic applications of structural geology, infrasound, fluid dynamics, petrology, and social science. The opportunities to travel around the world gave me a broader view of volcanic systems and a greater appreciation for their variability. I thank him immensely for being patient with the development of my writing skills, and for guiding me towards the proper path when I hit dead ends. I sincerely appreciate his unending support for intellectual growth and expansion. His wisdom, compassion, and belief in my success allowed me to pursue this dissertation to its fullest capacity. His mentoring and facilitation in networking and collegial communication has provided me a solid foundation from which I will confidentially pursue a successful career.

My committee provided useful help, guidance, and support. Thank you to Dr. Don Swanson for teaching me about field techniques, writing style, and Kīlauea's history, as well as opening my mind to alternative interpretations of volcanic features I had not previously considered. His knowledge is immense, his heart is open, his kindness is encouraging, and his guidance is truly appreciated. Thank you to Dr. Sarah Fagents for seeing me through a second degree. Her rigor and level of excellence in both quantitative studies and editorial skills have made me a better scientist. Her advice is always sound, and I appreciate that she sets the bar high. She was a role model and inspiration for both my undergraduate work and my dissertation work. Thank you to Dr. Scott Rowland, who provided valuable discussions about Kīlauea, volcanology, field techniques, and writing style. Finally, a very sincere thank you to Dr. David Muenow and Dr. Francis Sansone, both of whom stepped up in a time of great need. I deeply appreciated the unquestioning generosity and enthusiasm both men displayed when I needed it most. The time they spent to urgently read and give advice on my written dissertation has my utmost gratitude.

The Hawaiian Volcano Observatory was crucial to the success of my doctoral studies, and I am grateful to them for their support, interest, and facilitation of this research. Thank you to Jim Kauahikaua, Tim Orr, Mike Poland, Steve Brantley, Jane Takahashi, and Matt Patrick.

This work was funded by the National Science Foundation, the Hawaiian Volcano Observatory, and the University of Hawaiʻi at Mānoa's department of Geology and Geophysics. Their financial support is sincerely appreciated.

An enthusiastic and heartfelt thank you goes to my family and close friends, who supported and encouraged me through every part of my degree.

Their unwavering belief in me was both priceless and wholly appreciated. Thank you Scott Parcheta, Debra Parcheta, Mark Parcheta, and Stephanie Parcheta for cheering me on and being my biggest fans. Thank you to Lisa Baldwin, Karina Geronilla, Ashley Harrison, and Jessica Shank for being my sisters through the thick and the thin that life has to offer. Their friendships mean the world to me, and they were always there when I needed them.

Thank you to everyone at the University of Hawaiʻi at Mānoa who helped me complete this research and still enjoy life. Thank you to my office husband, Owen Neill, and wives Malin Klawonn, Maria Janebo, and Sarah Glancy for putting up with my odd working hours and constant snacking with tea/hot cocoa making. Thank you to my roommates at University Manor, for cooking and laughing with me: Etsuko, Katie Small, and Takara Tada. Thank you to my Wilhelmina rise roommate, Katie Robinson, for understanding my crazy work schedule and putting up with the bus for a year. Thank you to Leona Anthony, Alison Houghton, and Susan Van Gorder for making the administrative part of life proceed flawlessly. Thank you to the professors who provided valuable discussions, insights, and support to all aspects of my dissertation topic: Janet Becker, Fred Dunnebeir, Chip Fletcher, Neil Frazer, Mike Garcia, Julia Hammer, Eric Hellebrand, Garette Ito, Steve Martel, John Sinton, Jeff Taylor, and Cecily Wolfe. Thank you to my two lab assistants, Lauren Swavely and Kristine Kosinski, who performed above and beyond what I'd asked of them. Thank you to the early graduate students and friends for their humor, advise, and support: Wendy Stovall, Kurtis and Erin Nishimura, Loÿc Vanderkluysen, Alain Volentik, Nicole Lautze, Tom Fedenczuk, Eva Marie-Nosal, Matthew Barbee, Tom Shea, Deb Eason, Shelley Isgett, Lydia Hallis, Julia Eychenne, Kae Tsunematsu, and Lisa Munger. I'd like to thank the current grad student cohort for getting me out of the office and always having a fun time: Jonathan Sleeper, Sam Howell, Jessica Zaiss-Bowman, Sarah Maher, Jessica Barnes, Brian Boston, Regan Austin, Lydia Baker, Chris Goodwin, Christine Waters, Alice Coleman, Mary Tardona, Emily First, Kendra Lynn, Jonathan Tree, Sarah Crites, David Trang, Patrick Gasda, Christine Jilly, Matt Markley, Erin Fitch, and Jessica Orfe. I'd like to thank Penny Larin for being awesome.

Finally, a special thank you to the people in my life outside of academia who provided balance, exercise, peace and tranquility. Thank you, Janice Kim, for being the best landlord on the planet, and thank you to both her and Chuck Ferrera for being fantastic friends, supporting my ice cream addiction, guiding my cooking/baking skills, editing a preliminary draft of my work, and for being interested in my research. Thank you to Marcus for listening, offering opinions, and encouraging me. Thank you, Coach Geoff and the Saint Louis track team ,for 6 wonderful seasons, including the 2009 state track meet championship. Thank you to everyone at volcanic rock gym for welcoming me into the climbing community. Thank you, Casey, for a fun, peaceful, and relaxing end to my dissertation.

Abstract

Hawaiian fountains, typically occurring on basaltic volcanoes, are sustained, weakly-explosive jets of gas and juvenile ejecta. A broad range of Hawaiian fountaining styles occurred during twelve episodes of the Mauna Ulu eruption on Kīlauea between May and December 1969. The western episode 1 fissure system is currently well exposed, providing an exclusive opportunity to study processes of low-intensity fissure fountains. Episode 1 fountains occurred along a 5 km long fissure system that exploited the eastern-most kilometer of the Koʻai fault system. A low, near-continuous, spatter rampart is present on the northern upwind and upslope side of the fissure. Most pyroclastic products, however, fell downwind to the south and little was preserved because of two processes: 1) incorporation of proximal spatter in rheomorphic lava flows 10–20 meters from the vents, and 2) downslope transport of cooler spatter falling on top of these flows >20 meters from vent. There is a clear 'lava-shed' delineation between lava that drained back into the fissure and lava that continued flowing into the flowfield. Vents range in surface geometry from linear–circular, with superimposed irregularity and sinuosity, and range from straight-sided–flaring cross-sectional geometries. Irregularity results from joints in the pre-existing wall rock. Sinuosity results from the local stress field. Geometry of non-flared vents could indicate the true geometry of the dike. Flared vents likely formed through mechanical erosion and thermo-mechanical abrasion. Vent positions along the fissure likely resulted from flow focusing. Uniquely, these vents drained and remain unobstructed (some >100 m depth), despite subsequent nearby eruptive activity. Three vents were imaged ≤16 m in depth at <4 cm resolution with tripod-mounted LiDAR. Textural analyses of pyroclasts from eruptive episodes 2–12 show three distinct degassing and outgassing paths: 1) rapid degassing and quenching with minimal outgassing, 2) prolonged degassing and outgassing, and 3) rapid degassing and quenching on pyroclasts' rims with prolonged internal bubble coalesce. Contrasting patterns of shallow degassing and outgassing were the dominant control driving Hawaiian fountain behavior and variability, and are probably the dominant control for many other Hawaiian-style eruptions.

Table of Contents

List of Tables

List of Figures

List of Abbreviations

Above sea level	asl
American Geophysical Union	AGU
And others	et al.
And so forth	etc.
Approximately	ca.
Aspect ratio	AR
Carbon dioxide	CO_2
Dense rock equivalent	DRE
Digital elevation model	DEM
Dots per inch	dpi
East Rift Zone	ERZ
East-northeast	ENE
Eastern fountaining zone	EZ
Episode	Ep
Episodes	Eps
Equivalent diameter	Eq D
Figure	Fig.
Flaring ratio	FR
For example	e.g.
Global positioning system	GPS
Hawaiian Standard Time	HST
Hawaiian Volcano Observatory	HVO
In other words/that is	i.e.
Inter-episode	iEp
Interferometric synthetic aperture radar	InSAR
Jeffery B. Judd	JBJ
Late-stage eruptive activity	L
Light detection and ranging	LiDAR
Million years	Ma
North	N
Peak of eruptive activity	P
Scanning electron microscope	SEM
South	S
Southwest	SW
Southwest Rift Zone	SWRZ
Three-dimensional	3D
Two-dimensional	2D
United States Geological Survey	USGS
University of Hawai‘i	UH
Vesicle number density	VND
Vesicle size distribution	VSD
Vesicle volume distribution	VVD
Water	H_2O
Western fountaining zone	WZ

List of Units and Symbols

area	A
approximately	~
bubble size distribution	N_a
Celcius	C
centimeter	cm
compressive stress	σ_c
corrected melt volume	N_v^m
crustal thickness measurements	c
day	d
degrees	°
dip angle	°
Fahrenheit	F
flow directions	°
hour	hr
gram	g
greater than	>
greater than or equal to	≥
kilogram	kg
kilometer	km
kilovolts	kV
lava cooling time	t
length	l
less than	<
less than or equal to	≤
magnification	x
meter	m
micrometer	μm
millimeter	mm
minute	min
nano ampere	nA
outer rampart slope angle	°
pi	π
plunge angle	°
percent	%
regularity	Ω
regression coefficient	R^2
second	s
semi-major axis	λ_1
semi-minor axis	λ_2
strike	°
vent slope angle	θ
temperature	T
tensile stress	σ_t
volume of gas	V_g
volume of melt	V_m
volume size distribution	N_v
years	yr

Chapter 1

Introduction

1.1 Dissertation Overview

This dissertation examines the variability of Hawaiian-style basaltic fountaining behavior, with an emphasis on fountains from a fissure source. The 1969 episodes of the 1969–1974 Mauna Ulu eruption of Kīlauea are used as a case study because they provide unique exposures of the vent and shallow conduit. The twelve fountaining episodes span the full spectrum of fountain intensity seen historically at Kīlauea volcano. This chapter provides the context of this research path and how it fits in and augments the body of scientific literature. Chapters 2 and 3 focus specifically on fountains from a fissure source, documenting subaerial products and the geometry of the vents and the shallow conduit respectively. Chapter 4 expands in scope to look at vesicularity across various fountain intensities and styles. The final chapter (chapter 5) unites the interpretations in chapters 2 through 4 and looks ahead at the broader impacts of this research for future studies.

1.2 Volcanological Setting

1.2.1 Hawaiian Islands

The Hawaiian-Emperor seamount chain is a semi-linear string of volcanic seamounts, atolls, and islands, 80 of which have been identified and named.

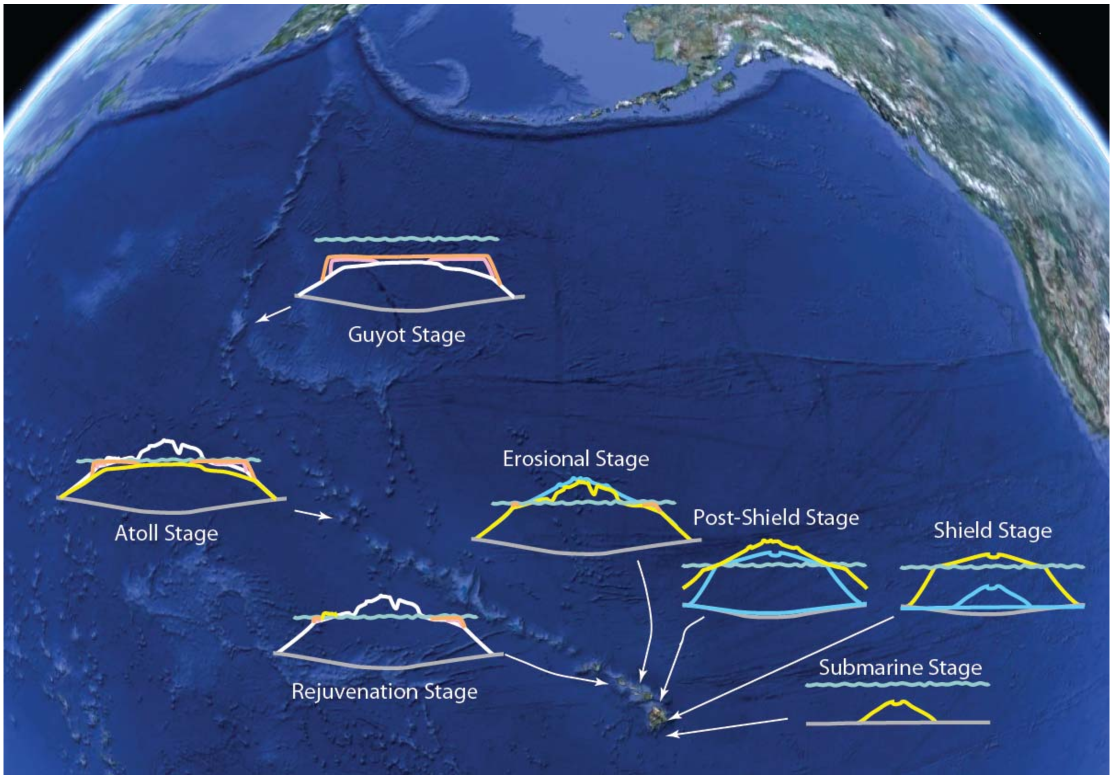

Figure 1.1 Google Earth image of the Hawaiian-Emperor seamount chain. The life cycle stages of oceanic volcanoes forming islands are depicted with cross-sectional line drawings and arrows that point to islands with volcanoes in each respective stage.

The chain stretches 5,800 kilometers (km) across the Pacific Ocean from 19 degrees (˚) north (N), where volcanic activity is ongoing today, to 54˚ N at the North Pacific Aleutian Submarine Trench (figure (Fig.) 1.1), where the oldest date measured on the extinct volcanoes is 81 million years (Ma) old. With the plate tectonic revolution in the early1960s, the island chain became regarded as a classical hotspot track along the Pacific basin, tracing out the movements of the Pacific plate as it passed over a stationary mantle plume (Wilson, 1963; Decker, 1987; Sharp and Clague, 2006). Recent paleomagnetic data (Tarduno and others (et. al.), 2009) has shifted this paradigm with evidence that the mantle plume is not fixed in location, but has moved southward over the last 80 Ma, so that the hotspot track is the sum of both plate and plume movements. The mantle plume itself was recently imaged with seismic tomography (Wolfe et al., 2011) as a narrowing, downward sloping, and inclined low velocity zone reaching to 1500 km depth.

The volcanic islands that make up the Hawaiian-Emperor seamount chain pass through an island "life cycle" (Fig. 1.1), initially proposed by Stearns (1946) and modified by Macdonald et al. (1983) and Moore and Clague (1992). The life cycle includes growth (alkali submarine shield building, tholeiitic subaerial shield-building, alkalic cap/post-shield building), erosion and fringing reef growth, rejuvenation volcanism (alkalic and explosive), erosion and barrier reef growth with slow sinking until an atoll is formed, and finally complete re-submergence as a seamount and accompanied by the death of the reef. In all eruptive phases during the life cycle, magma rises buoyantly from the mantle plume, through the lithosphere, and into shallow storage in the volcano before being erupted (Tilling and Dvorak, 1993). The alkalic and tholeiitic melts are considered to represent low and high degrees of melting, respectively, as the volcano approaches, passes over, and moves off the hotspot. Whereas the islands in the Hawaiian-Emperor seamount chain helped create the concept of a volcanic island life cycle, very few of the volcanoes have passed through every stage.

1.2.2 Kīlauea volcano

Eight volcanic islands make up the state of Hawai‘i (Fig. 1.2), and the southernmost, largest, and youngest of them is the island of Hawai‘i, or “the Big Island” (Macdonald et al., 1983), which is thought to be directly above the hot spot (Frey and Rhodes, 1983). Five subaerial and two submarine shield volcanoes make up the Big Island, and they are, from oldest to youngest, Māhukona, Kohala, Mauna Kea, Hualālai, Mauna Loa, Kīlauea, and Lō‘ihi (Moore and Clague, 1992). Kīlauea is the youngest subaerial volcano in the island of Hawai‘i and is host to the eruption studied in this dissertation. Ninety percent of the entire surface of the volcano has been resurfaced in the last 1,100 years (yr) (Holcomb, 1987), with alternating centuries-long effusive and explosive periods (Fiske et al., 2009; Swanson et al., 2012). These phases included the ‘Ailā‘au and Observatory shield-building eruptions, caldera collapse, and explosive phreatomagmatic explosions that sometimes reached into the jet stream; these eruptions dwarfed the current 30 yr long Pu‘u ‘Ō‘ō activity and the 1924 explosive summit eruption.

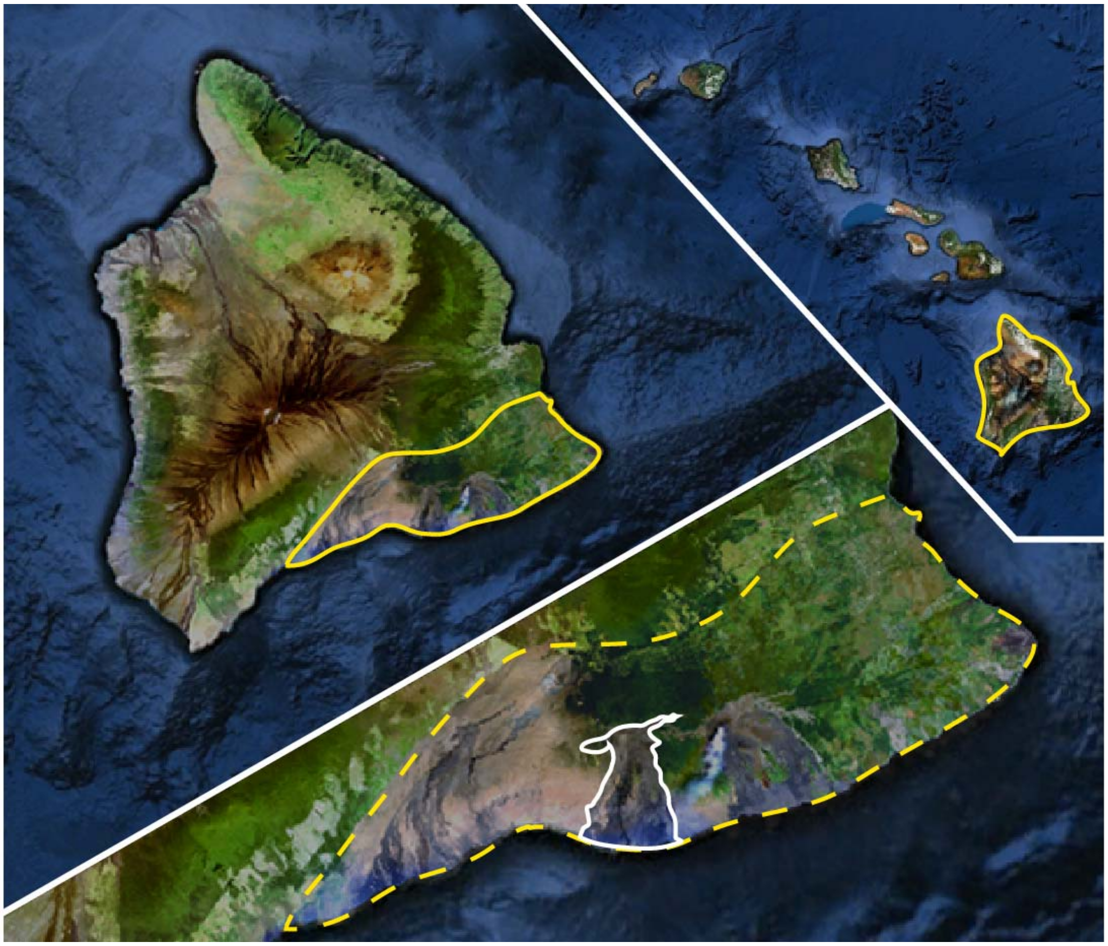

Figure 1.2 Top right Google Earth images of the Hawaiian Islands. From North to south: Niʻihau, Kauaʻi, Oʻahu, Molokaʻi, Maui, Kahoʻolawe, and Hawaiʻi (or "Big Island", outlined in yellow). **Upper left** The island of Hawaiʻi. The five subaerial volcanoes on the island are, from oldest to youngest, Kohala, Mauna Kea, Hualālai, Mauna Loa, and Kīlauea (outlined in yellow). **Lower right** The full extent of the Mauna Ulu lava flows is indicated by a white outline, and is near the geographic center of Kīlauea volcano.

Melting originates in the plume around 80 km depth and rises towards Mauna Loa and Kīlauea. The pathway utilized by the magma was first defined using earthquake foci by Tilling and Dvorak (1993). Magma supply to the volcanoes is variable over timescales of years to decades and has been calculated for Kīlauea during specific periods. Swanson (1972) calculated a supply rate of 0.11 km^3 yr^{-1} for three eruptions in 1952, 1968–69, and 1969–1971, and during this period there was minimal edifice deformation during the eruptions. This is an elevated supply rate from the preceding 18 yr repose period as well as with respect to the period from 1975 to 1982, between two major flank eruptions, during which it was 0.08 km^3 yr^{-1} (Johnson, 1995). Magmatic supply again increased to 0.12 km^3 yr^{-1} when Puʻu ʻŌʻō began erupting in 1983 (Heliker et al., 2003) and recent work by Poland et al. (2012), shows that this rate almost doubled during the years 2003–2007, but has since returned to about 0.12 km^3 yr^1.

Within the volcanic edifice, the shallow magma storage beneath the summit is located under the south end of the caldera, with multiple inflation sources under both the south rim and the middle of the caldera floor at depths of a few hundred meters to 3 km (Fiske and Kinoshita, 1969). It is still currently undecided whether the shallow summit storage region is a spherical or simply shaped reservoir (Yang et al., 1992) with a more viscous crystallizing layer on the walls (Pietruszka and Garcia, 1999) or a complex amalgamation of interconnected dikes and sills (Fiske and Kinoshita, 1969). Whether the mantle melting region exploits a single conduit to supply the volcano or a deeper extension of this dike and sill plexus proposed by Eaton and Murata (1960) and Fiske and Kinoshita (1969) is unknown as the techniques available do not resolve to a fine enough scale.

The structure of Kīlauea is better documented than that of other volcanoes because of its uniquely persistent activity in historical times. Ongoing eruption since January 1983 has provided ample and continuous opportunity for observing, quantifying, and interpreting the volcanic system. The volcano is buttressed against the eastern flank of Mauna Loa, and at its summit is a 4 x 3.2 km wide caldera with rim heights up to 120 meters (m) tall (Macdonald et al., 1983). The current summit eruption is located on the southeast side of Halema‘uma‘u pit crater, near the southwestern edge of the caldera. Two rift zones extend outwards from the caldera: the southwest rift zone (SWRZ), which bends slightly southward with distance from the caldera, and the east rift zone (ERZ), which starts near Kīlauea Iki crater and extends southeastward until Pauahi pit crater, where it bends to trend east-northeast to the coast and into the submarine environment (Fig. 1.3). The subsurface structure of the highly active ERZ has a dike-like geometry, extending subaerially for 55 km (with melt storage at 3–4 km depth, Johnson, 1995), and is 2–4 km wide on the surface of Kīlauea.

Kīlauea’s most recent eruptions have been only weakly explosive (in other words (i.e.), Hawaiian-style fountaining events) and/or effusive, beginning in 1952 and occurring on a near-annual basis through the 1960s, with eruptions in the following locals (starting dates given in parentheses):

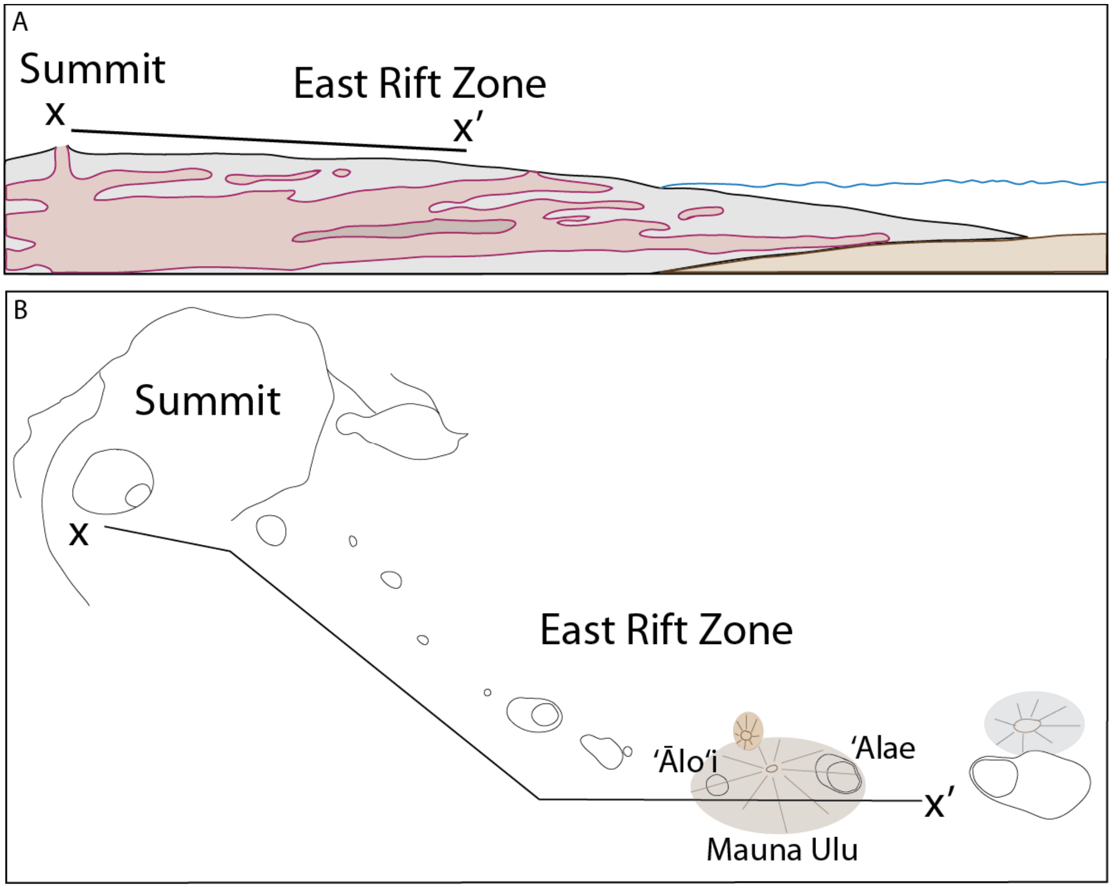

Figure 1.3 **A** Modified from Holcomb (1987). A schematic cross-section of Kīlauea’s rift zone going down rift. It has been suggested that the rift zone has at least two (possibly more) storage levels. **B** Map view sketch of Kīlauea’s summit and upper east rift zone. Note the Mauna Ulu footprint covers ‘Ālo‘i and ‘Alae craters, indicating they are now filled in with lava.

Halemauʻmaʻu: 1952 (Jun 27), 1961 (Feb 24, Mar 3, Jul 10), 1967 (Nov 5), 1975 (Nov 29), 2008 (Mar 15–still ongoing),

Summit caldera: 1954 (May 31), 1959 (Nov 14), 1971 (Aug 14, Sept 24), 1974 (July 19, Sep 19), 1975 (Nov 29), and 1982 (Apr 30, Sept 25),

SWRZ: 1971 (Sept 24), and 1974 (Dec 31), and

ERZ: 1955 (Feb 24), 1960 (Jan 13), 1961 (Sep 22), 1962 (Dec 7), 1963 (Aug 21, Oct 5), 1965 (Mar 5, Dec 24), 1968 (Aug 22, Oct 8), 1969 (Feb 22, May 24–Fig. 1.3), 1972 (Feb 3), 1973 (May 5, Nov 10), 1974 (July 19), 1977 (Sept 13), 1979 (Nov 16), and 1983 (Jan 3–still ongoing).

Of these fountaining eruptions, most are characterized by single episodes of low to moderate (<150 m in height) fountain activity from fissure sources and moderate (<400 m in height) fountain activity from circular sources. However, several episodes from the multi-episodic eruptions of Puʻu ʻŌʻō (1983–present), Mauna Ulu (1969–1974), and Kīlauea Iki (1959) included high fountaining episodes of 450–580 m fountain height.

1.3 Eruption dynamics and variability in fountains

1.3.1 Hawaiian fountaining

Basaltic eruptions of effusive and weakly explosive character occur at such volcanoes as Kīlauea, Etna, Nyiragongo, Izu-Oshima, and Eyjafjallajökull. Kīlauea is the archetypical location for sustained weakly explosive basaltic eruption behavior, and thus this style of activity was named after its location as "Hawaiian fountaining" or "Hawaiian-style eruptions" (Walker, 1973). Hawaiian fountains are uprushing two-phase jets of gas and incandescent pyroclasts (Wolff and Sumner, 2000). Historical Hawaiian style fountains worldwide vary in height by three orders of magnitude (<1600 m), but heights at Kīlauea have reached up to 580 m.

It is generally agreed that Hawaiian-style volcanism involves sustained release of exsolved, buoyant gas bubbles that drive the eruption. The mechanism (Fig. 1.4) of ascent and eruption, however, can be (and is) viewed in two ways: 1) small gas bubbles form in the conduit and, being coupled to the melt, fragment the ascending magma at shallow depths (Wilson, 1980; Parfitt, 2004), or 2) a magmatic foam collapses at the top of a magma storage region and produces an annular flow of gas and melt (Vergniolle and Jaupart, 1986; Vergniolle and Mangan, 2000). The difference in models is essentially that the Wilson and Parfitt model assumes a relatively closed and coupled magma-gas system, especially at shallow depths, whereas the Vergniolle and Jaupart model assumes a relatively open and decoupled magma-gas system. We use the Wilson and Parfitt model, discussed further in chapter 4, because pyroclastic textures do not indicate a foam collapse event.

Studies of the dynamics of fissure eruptions are rare. Deposits tend to be intensely welded and key observations are hard to make during the eruption because of the associated hazards and high heat flux. There are computational

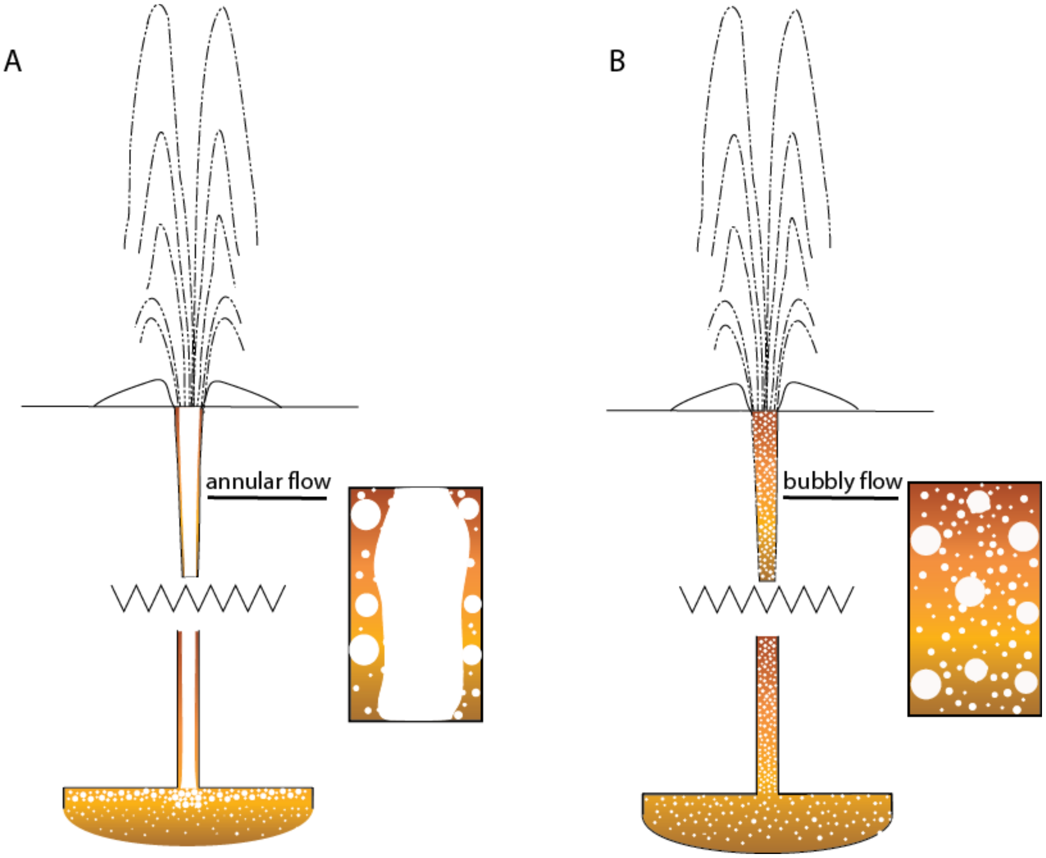

Figure 1.4 Schematic diagrams depicting the differences between Hawaiian fountain eruption models. **A** The Vergnoille and Jaupart model invokes foam formation in the magma chamber than, upon collapse, creates larger slugs of gas which travel up the conduit to produce Hawaiian style fountaining. This is a relatively open system with the gas phase mostly decoupled from the melt phase. **B** The Wilson and Parfitt model utilizes bubble nucleation and buoyant rise of the bubbles when coupled with the magma to drive fountain dynamics during an eruption. This is a relatively closed system approach to treating fountain behavior.

issues because, by definition, fissures are two-dimensional (2D) in x-y space (on the ground surface they have a finite length and width that are not equal).

1.3.2 Vesiculation in basaltic systems

The location and duration of bubble nucleation is a critical process in driving the intensity and style of the activity (e.g., Toramaru, 1995; Gerlach and Graeber, 1985). Once formed, diffusive and decompressive growth of the gas bubbles takes place and, in an open system, the largest bubbles buoyantly rise through the magma (Fig. 1.5). Growing evidence suggests that variability in eruptive behavior (fountain height, discharge rate, steadiness, and so forth (etc.)) cannot be correlated strictly to eruption rate, but is also related to the fluid dynamics of ascending vesiculating magma (Wilson, 1980; Wilson and Head, 1981; Lejeune, 1995; Wallace, 2005; Gonnerman and Manga, 2007, Edmonds and Gerlach, 2007). Gas coupling in the system, especially the manner and depth of its segregation into a gas phase, are thought to be particularly important. Pre-eruptive gas content, shallow conduit dimensions, and magma rheology also combine to define complex feedbacks that affect eruption mechanisms, style, and intensity. Aside from the pioneering work at Pu‘u ‘Ō‘ō (Mangan and Cashman, 1996) and recent studies of the 1959 Kīlauea Iki eruption by Stovall et al. (2011, 2012), vesicularity studies of Hawaiian pyroclasts are limited.

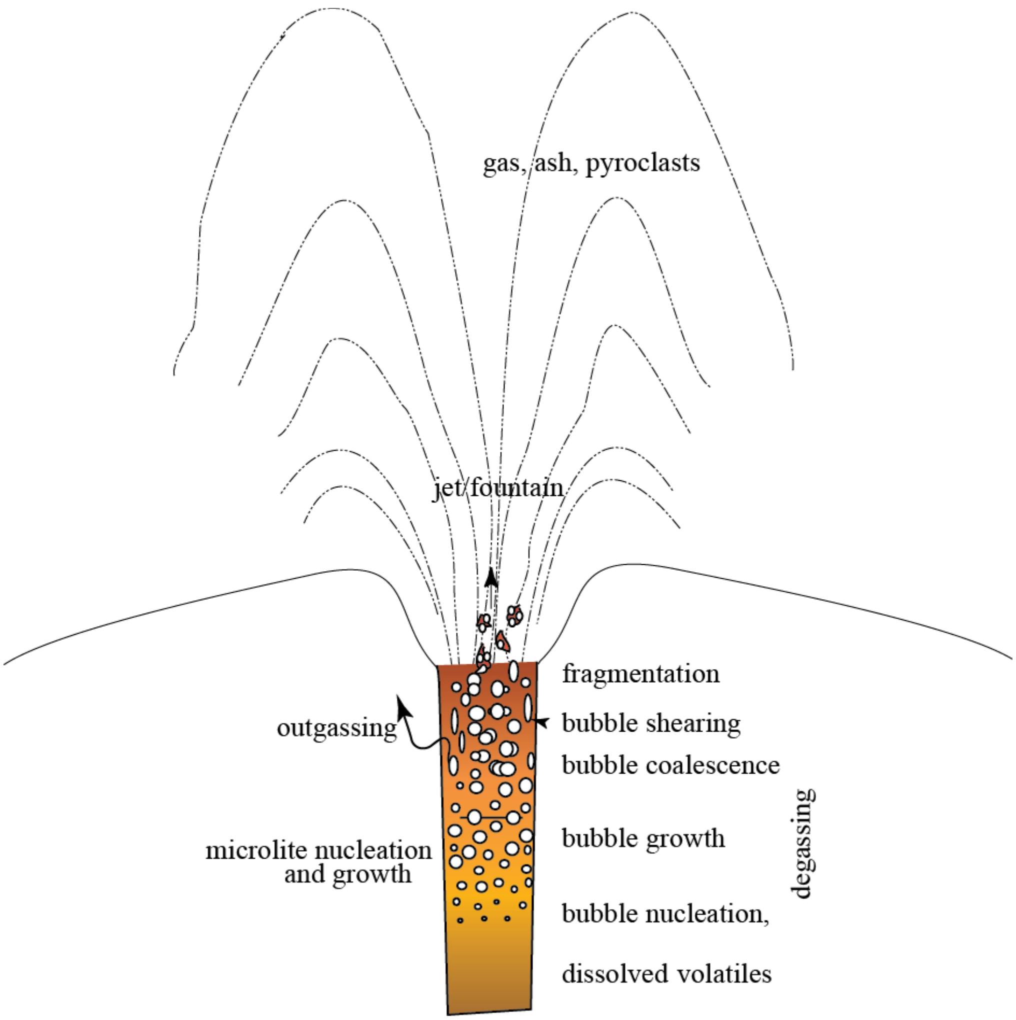

Figure 1.5 Schematic diagram of basaltic degassing processes (not to scale). At a depth of critical super saturation, dissolved volatiles will nucleate bubbles either homogeneously or heterogeneously. The bubbles, being buoyant, rise towards the free surface. As pressure decreases during ascent, and as more dissolved volatiles diffuse into gas phase, the bubbles grow in size. Microlites (microscopic crystals) may also begin to nucleate as volatiles leave the melt to preferentially be in the gas phase. Bubbles may become large enough to feel their neighbors, and coalescence can occur. At fast magma ascent rates, bubbles may also become sheared, especially at the conduit margins, before fragmentation takes place. After fragmentation, gas, ash, and pyroclasts exit the vent in a jet or fountain. The processes of bubble nucleation to coalescence are called degassing. If gas can escape the system through the conduit walls, it is called outgassing.

1.4 Mauna Ulu 1969–1974 eruption

The Feb 22, 1969 eruption of the ERZ was a precursory fissure eruption to the Mauna Ulu eruption, and occurred in the same area as the 5 yr long eruption. This activity has also been grouped retrospectively in name with the Mauna Ulu eruption, but is still recognized as separate from the 5 yr of Mauna Ulu activity. The Mauna Ulu eruption is the second longest and second most voluminous historical eruption on Kīlauea, superseded only by the current Puʻu ʻŌʻō eruption.

1.4.1 Chronology

The Mauna Ulu eruption of Kīlauea was initiated by a 36 hour (hr) long episode of fissure fountains on May 24–25, 1969 (Swanson et al., 1979; Tilling et al., 1987). Eyewitness accounts (Swanson et al., 1979) indicate that the Mauna Ulu fissure system was preceded by a propagating earthquake swarm that was felt in the nearby town of Volcano. The fissure system opened at 04:45 am Hawaiʻi Standard Time (HST) and rapidly lengthened to 2.5 km in 15 minutes (min) (by 05:00), stretching from 200 m north of ʻAlae Crater across ʻĀloʻi Crater to the old Chain of Craters Road. The fissure system crossed the former ʻĀinahou Road (current Chain of Craters Road) at 08:30. Initially, the whole fissure system hosted low fountains ≤ 50 m high, but then it evolved into two fountaining zones: one between ʻAlae and ʻĀloʻi craters (the eastern fountaining zone (EZ)), and the other between the Chain of Craters Road and ʻĀinahou Road (the western fountaining zone (WZ)), separated by an inactive region 1 km long, through ʻĀloʻi Crater. Twenty-five meters of lava that had ponded in ʻĀloʻi during the February 22, 1969 eruption had completely drained into the new fissure by mid-morning. Both fountaining zones fed lava flows that moved down a gentle southward slope, as described in Swanson et al. (1979). Most later eruptive activity was located between the two pit craters; the WZ never erupted again and, fortunately for our work, was not buried by later activity.

Fountains from the 11 following episodes in 1969 (Fig. 1.6) ranged from low, 50 m high fountains in episode (Ep) 1 to a 540 m high fountain in Ep 9, the second highest ever recorded at Kīlauea. These fountains issued from two vents 75 m apart through September and, thereafter from a single vent until the end of December; Ep 1 was the only fissure activity during the Mauna Ulu 1969 eruption, building a series of discontinuous low spatter ramparts. By the end of 1969, a 50 m high tephra cone had been constructed around the two vents, with medial and distal deposits stretching to the south-southwest, in the direction of the trade winds. Three well-documented effusive stages ensued from January 1970 to October 1971 (Swanson et al., 1979). Activity included spattering, gas pistoning, broken dome fountains, and channelized and tube-fed lava flows, as well as the eventual filling of both ‘Alae and ‘Ālo‘i pit craters. The tephra cone evolved into a lava shield, growing to a total height of 100 m by the end of activity in October 1971. Lava reoccupied the Mauna Ulu vents in February 1972, and activity continued in the same fashion as stages 2–4 from 1970–1971, overflowing the shield and raising the summit to its final height of 120 m above the pre-eruptive surface.

1.4.2 Literature references

The Mauna Ulu eruption provided an early chance for scientists to study Hawaiian volcanic processes both on the surface and in the subsurface. Some

Figure 1.6 Episode number and height of fountain shown in each photograph; photograph from episodes 3 and 7 show vent area after fountaining ceased. All photos are from the Hawaiian Volcano Observatory.

of the key observations to come from the Mauna Ulu eruption include lava flow dynamics (Swanson, 1974, Peterson and Tilling, 1980, Peterson et al., 1994), gas pistoning behavior (Swanson et al., 1979, Tilling, 1987), the nature of steady-state magma transfer down the rift zone (Tilling, 1987), and the ability to measure magma supply rate (Swanson, 1972; Dzurisin, et al., 1984).

Lava flows, seen commonly in the geologic record of Kīlauea, could be observed in detail during their formation, which allowed for a better understanding of flow dynamics, relationships to eruptive behaviors, and interpretation of older lava flows. Shelley pāhoehoe, rarely preserved due to its brittle nature, was documented forming as gassy lava toes, and the origin of dense, degassed flows (fountain-derived) and dense, tumuli-rich pāhoehoe flows (lava tube-derived) were also described (Swanson, 1972). This allowed for the interpretation that Kīlauea's vast pre-historical pāhoehoe flow fields were also tube-fed, even though their emplacement was unobserved and undocumented (Holcomb, 1987). Moore et al. (1973) documented tube-fed flows that entered the ocean, noting that lava advances by different mechanisms when flowing under water. One method of advance was as cylindrical lobes, and the other was by cracking that allowed lava to grow more rapidly as rounded "pillows."

Duffield (1972) described the formation and motion of lava crusts across the top of lava ponds in the Mauna Ulu vents, making an analogy to small-scale plate tectonics (then a recent paradigm shift in geology). Flow lines along the lava plates indicated direction of movement, which occurred perpendicular to "rifts" during slight uplifts and drops of the lava column from which the plates spread apart. Another behavior of the magma column that was observed for the first time was the behavior termed gas pistoning. This is a process by which magma rises slowly over tens of minutes in the vent and then rapidly outgases within tens of seconds, dropping down to the pre-rise level. This outgassing occurs when the magma column is at its peak height but can also be triggered artificially by disturbing the free surface at critical times (Swanson et al., 1979).

After the Pu‘u ‘Ō‘ō eruption began in 1983, and with its three-decade run of activity, Mauna Ulu became a largely forgotten eruption, and little has been published subsequently on the Mauna Ulu eruption, especially regarding the May 24–25, 1969 opening fissure.

1.5 Dissertation structure

Chapter 2 details the chronology of Mauna Ulu’s Ep 1 fissure fountaining and the interplay between lava flows and growth of spatter ramparts. Data sets are presented on pre-eruptive forest density, post-eruptive tree mold locations, pre-existing topography, pre-existing ground slope, the current topography, lava flow directions, lava bench heights, spatter rampart geometries, and spatter textures. These data sets are combined to construct a model of how a fissure system behaves from inception to cessation of fountain activity. Relative timing of events is deduced, because absolute timing can seldom be pinpointed, and is used to interpret how drainage of erupted lava back into the fissure affected the remaining fountains, as well as the final flow surface. This chapter was published in *Bulletin of Volcanology* in 2012 (Volume 74, issue 7, pages 1729–

1743, doi: 10.1007/s00445-012-621-1). The final publication is available at www.springerlink.com.

Chapter 3 builds on chapter 2, looking again at Ep 1 of the Mauna Ulu eruption, but from a perspective of the magmatic conduit and vent system. Vent dimensions are mapped with centimeter precision along the full 900 m of exposure. Features of the vents, such as roughness, irregularities, sinuosity, and en echelon stepping are documented and discussed, as well as the vent parameters of aspect ratio and flaring ratio. This work will be submitted to *Bulletin of Volcanology* in April 2013.

Chapter 4 broadens in scope and in timescale to address conduit and eruption dynamics for four of the twelve fountaining episodes (Eps) (1, 5, 9, and 12), between May and December 1969, from a vesicularity and microtextural perspective. Episodes 1 and 9 represent extreme low and high Hawaiian fountain activity respectively, whereas Eps 5 and 12 represent intermediate activity from paired and single sources, respectively. The United States Geological Survey (USGS) samples taken before and after the peak of Ep 5 permit us to examine the change in vesicle textures through time for a single episode. This work is published in the *Journal of Volcanologic and Geothermal Research* (vol 255, pages 79–89, doi: 10.1016/j.jvolgeores.2013.01.016). The final publication is available at www.elsevier.com.

Chapter 2

Hawaiian fissure fountains 1: decoding deposits—
episode 1 of the 1969–1974 Mauna Ulu eruption

2.1 Introduction

Hawaiian fountains are the low intensity end-member in the spectrum of sustained explosive volcanic eruptions. They produce basaltic lava flows and construct cones or linear steep-sided accumulations (ramparts) of typically agglutinated spatter and/or scoria. Cones form during eruptions with a dominant single-source, circular vent, whereas ramparts form along sublinear fissure segments within fissure systems that are hundreds of meters to several kilometers in length. The asymmetry of spatter cones is common and well documented, driven either by downwind advection of the spatter (e.g., Puʻu ʻŌʻō in 1983–1986; Heliker et al., 2003) and/or by pre-existing topography (e.g., Kīlauea Iki 1959; Richter et al., 1970). Spatter rampart geometries are far less well described, but include both single ramparts and pairs of ramparts, symmetrically distributed along a fissure. Individual fountaining episodes at Kīlauea volcano have a range of durations from 2 hr (Richter et al., 1970) to 16 days (d) (Heliker et al., 2003) and eruption rates from 400 kilograms per second (kg/s) (Macdonald et al., 1983, 0.15 m^3/s) to 1.7×10^6 kg/s (Richter et al., 1970, 641 m^3/s). The range of maximum-recorded fountain heights at Kīlauea is 8 m (Heliker et al., 2003) to 579 m (Richter et al., 1970). Hawaiian fountains subdivide into moderate to high fountains (>100 m) with high mass discharge rates associated with single, circular sources, and low fountains (<100 m), often linked to linear sources and low mass eruption rates per unit length of fissure (unpublished data, Houghton).

Previous workers (for example (e.g.), Wilson ,1980; Wilson and Head, 1981; Vergniolle and Jaupart, 1990; Parfitt and Wilson, 1995; Parfitt et al., 1995; Vergniolle and Mangan, 2000; Slezin, 2003; Parfitt, 2004) have modeled point-source fountains and estimated magma ascent rates of 0.2–14.6 m/s (Wilson and Head, 1981). However, Hawaiian fountains are commonly fissure-fed for part or all of an eruption, as seen at Pu‘u ‘Ō‘ō in 1983 (Wolfe et al., 1988); Izu-Oshima in 1986 (Sumner, 1998; Aramaki et al., 1988); Etna in 1991, 1999, 2001, and 2008 (Stevens et al., 1997; La Delfa et al., 2001; Behncke and Neri, 2003; Bonaccorso et al., 2011); and Eyjafjallajökull in 2010 (Moune et al., 2012). Aside from work done in the early 1980s (Wilson, 1980; Wilson and Head, 1981), models to date do not consider eruptions from a fissure or variability in fountain height and mass discharge rate along such a source. This study provides new information on the diversity of processes in Hawaiian fissure fountains by considering a well-exposed deposit from the 1969–1974 Mauna Ulu episode 1 (Fig. 2.1), which present an opportunity to quantify the geometries of spatter ramparts and infer their interactions with coeval lava flows. Chapter 3 will address the vents and subsurface fissure system from this episode. Our aim is that data in this and the companion paper can be used to expand future computational models of Hawaiian fountains to include fissure sources with variability of the eruptive system at several levels. Episode 1 provides an opportunity to study

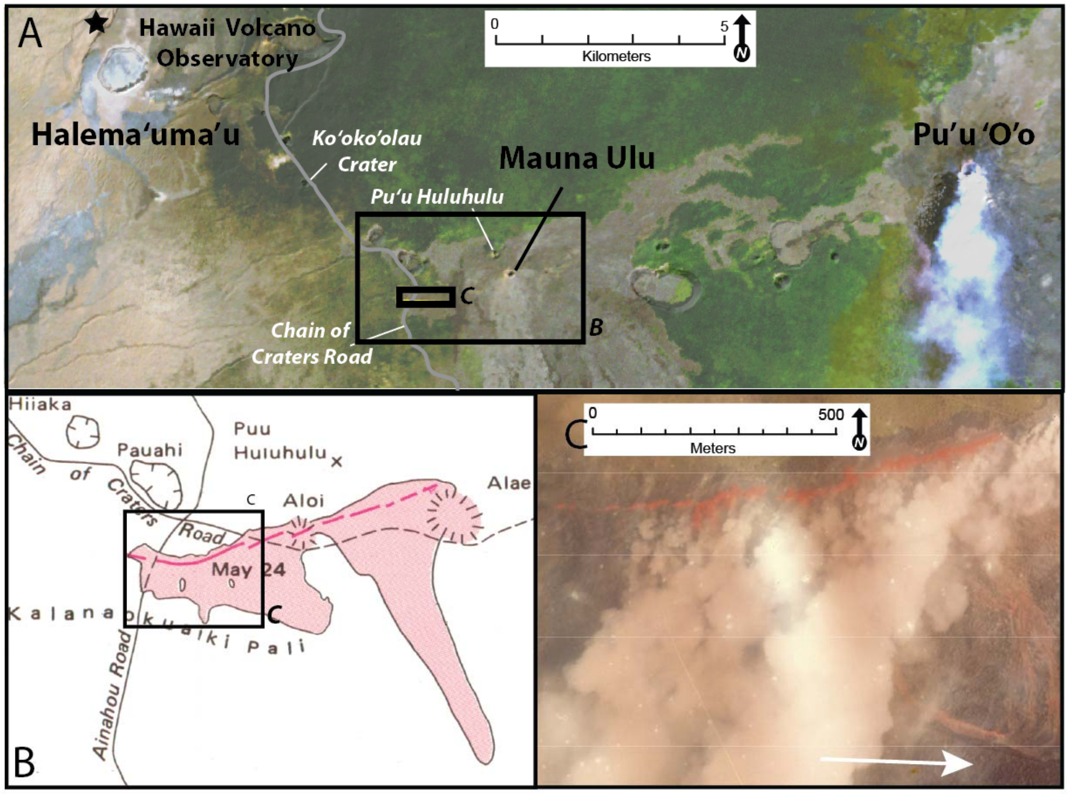

Figure 2.1 **A** Satellite image of Kīlauea, Hawaiʻi. Major locations (Halemaʻumaʻu, Mauna Ulu, Puʻu ʻŌʻō) are labeled. The present day Chain of Craters Road is labeled, and denoted with grey line, and locations of high points mentioned in text (Koʻokoʻolau Crater and Puʻu Huluhulu) are labeled. Thin black box labeled "B" designates area covered in Fig. 2.1b. Thick black box labeled "C" west of the Mauna Ulu shield denotes the field area. **B** Modified map from Swanson et al. (1979). Red line is the episode 1 fissure and pink shaded area is the extent of the eastern and western lava flow fields. This map indicates the old Chain of Craters road and ʻĀinahou Road. Box labeled "C" is extent of area covered by photograph in Fig. 2.1c. **C** Previously unpublished aerial photograph from Sandia Labs at 09:40 HST on May 24, 1969. Photograph taken 1 hr after fissure reached full length. Note that the flow field is fully developed (at lower right, white arrow).

and quantify a low-intensity fissure eruption, with preservation of both the fissure and proximal eruption products. Rampart height, fountain spacing, and the distribution of lava flows versus agglutinated spatter around the fissure allow us to interpret how deposits vary with discharge rate and local environment.

The 5 yr long Mauna Ulu eruption of Kīlauea (Fig. 2.1a) was initiated by an episode of fissure fountains on May 24, 1969 (Swanson et al., 1979; Tilling et al., 1987). Nine hundred meters of the originally 4.5 km long fissure system remains accessible, unaffected by contemporaneous and subsequent Mauna Ulu lava flows. Eyewitness accounts (Swanson et al., 1979) indicate that the Mauna Ulu fissure system (Fig. 2.1b, red line), preceded by a propagating earthquake swarm, opened at 04:45 HST east of the old Chain of Craters Road. (I will refer to the Mauna Ulu fissure system in this chapter simply as “the fissure” even though it is not a single continuous feature). Rapidly opening, the fissure bi-directionally extended 2.5 km in 15 min (by 05:00), from 200 m north of ‘Alae Crater in the east to the old Chain of Craters Road in the west, intersecting ‘Ālo‘i Crater (Fig. 2.1b). The fissure crossed the former ‘Āinahou Road (current Chain of Craters Road) at 08:30. Initially, the whole fissure length hosted low fountains up to (≤) 50 m high, but rapidly evolved into two fountaining zones: the EZ between ‘Alae and ‘Ālo‘i craters, and the WZ, our field area, (Fig. 2.1c) between Chain of Craters Road and ‘Āinahou Road, separated by an inactive region 1 km long, through ‘Ālo‘i Crater. The low fountains showed small, but largely undocumented, temporal and spatial variations in height.

Both fountaining zones fed lava flows that moved down a gentle southward slope, described in Swanson et al. (1979). During the 17.25 hr of activity at the WZ, flows were impounded 1.2 km down slope by Kulanaokuaiki Pali, a north-facing fault scarp. Swanson et al. (1979) calculated that a total magma volume of 4×10^6 m^3 was erupted on May 24– 25; no separate estimate was made for the EZ or WZ.

The eruption's ensuing 11 high-fountaining episodes and 3 effusive stages through 1974 are well-documented (Swanson et al., 1979; Tilling et al., 1987), but little more is published about episode 1 (Peterson, 1969; Swanson et al., 1971). This paper reconstructs the WZ events of May 24 from a physical volcanological perspective to (a) determine the intensity and variability in fountain behavior and coeval lava flows within a short-lived fissure system; (b) document the interaction between fountaining, lava flows, and drain-back of dynamically ponded lava; and (c) determine how the forest, ground slope, and flow dynamics affected rampart growth and preservation.

2.2 Field area and methods

2.2.1 Field area

Discontinuous spatter ramparts from the WZ (Fig. 2.2a) strike 080° in a 900 m long, 30 m wide region across the northern part of the field area. Lava flows from the fissure extend horizontally 50 m upslope to the north and 200 m downslope to the south where a 1–2.5 m wide and 400 m long non-eruptive crack (labeled as "April 1970" in plate 1; Swanson et al., 1979), then another kilometer southward to Kulanaokuaiki Pali. Data were collected within a

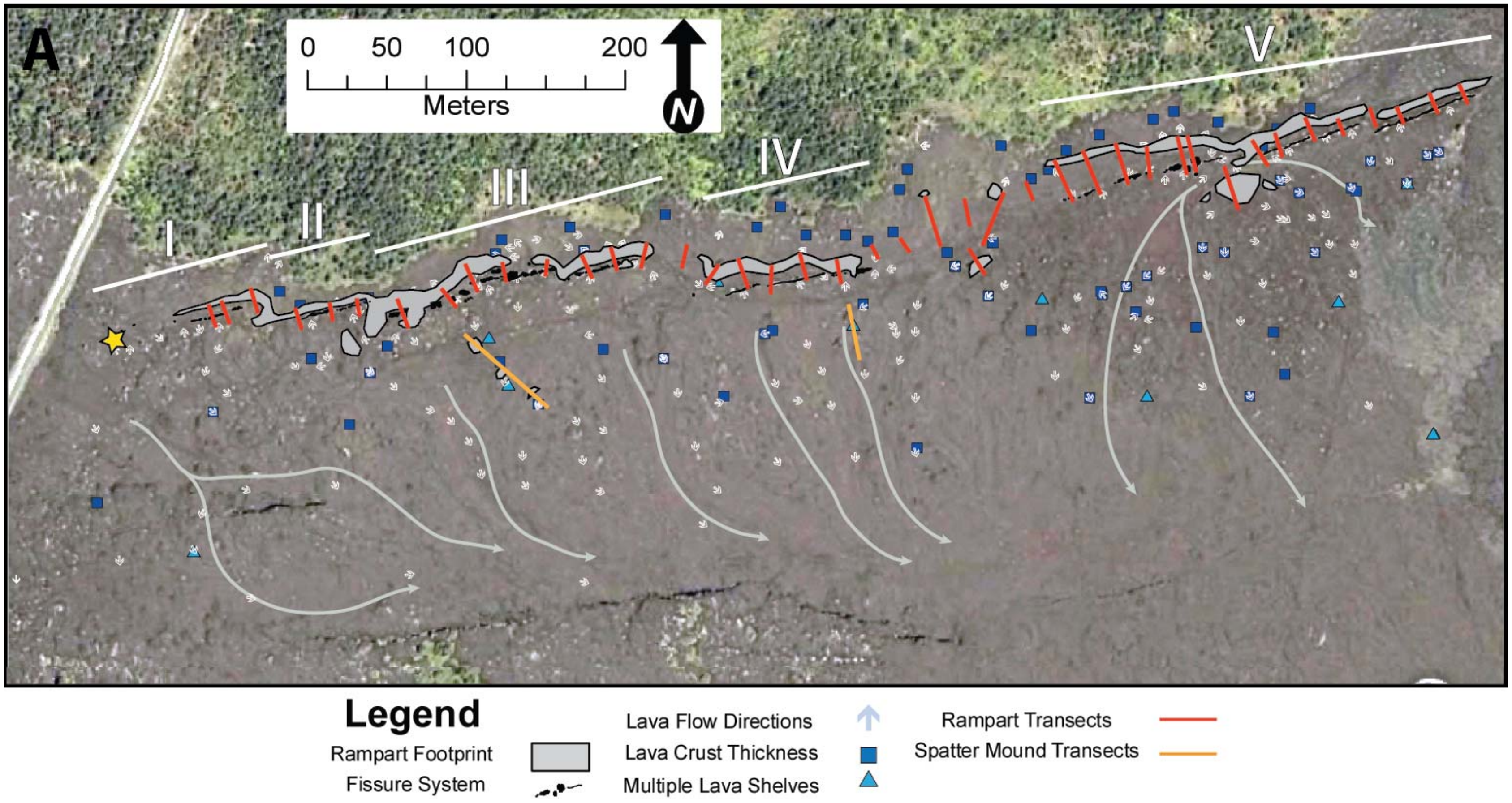

Figure 2.2 Location maps of data sets. Green: forest; gray: lava flow field; the road cutting the upper left corner: ʻĀinahou Road; dark linear feature in lava: an open, low relief, north-facing fault scarp. Rampart trace is light grey and the fissure is black. *Yellow star is vent 1 (the reference point of origin).* **A** Red lines across the ramparts are locations of 42 transects: 1- 40 (west to east) are on the northern side, transect 41 is on the western southern rampart (between IV and V), and transect 42 is on the eastern southern spatter rampart (middle of V). Dark blue squares are crustal thickness measurements, cyan triangles indicate multiple lava shelves, small white arrows are flow direction measurements, (pointing in the direction of flow), and long grey arrows indicate lava drainage pathways.

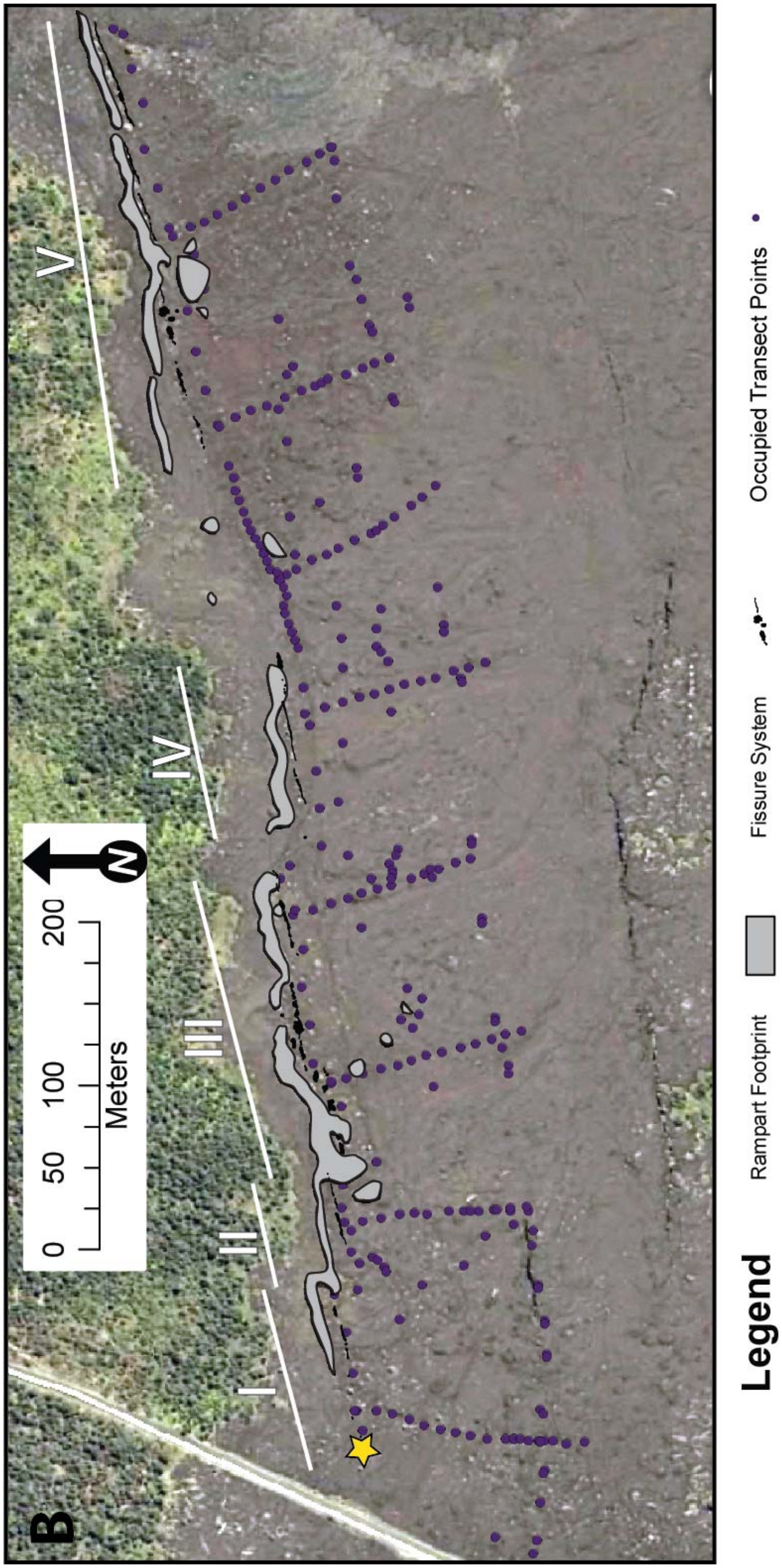

Figure 2.2 continued B Positions occupied for kinematic GPS transects.

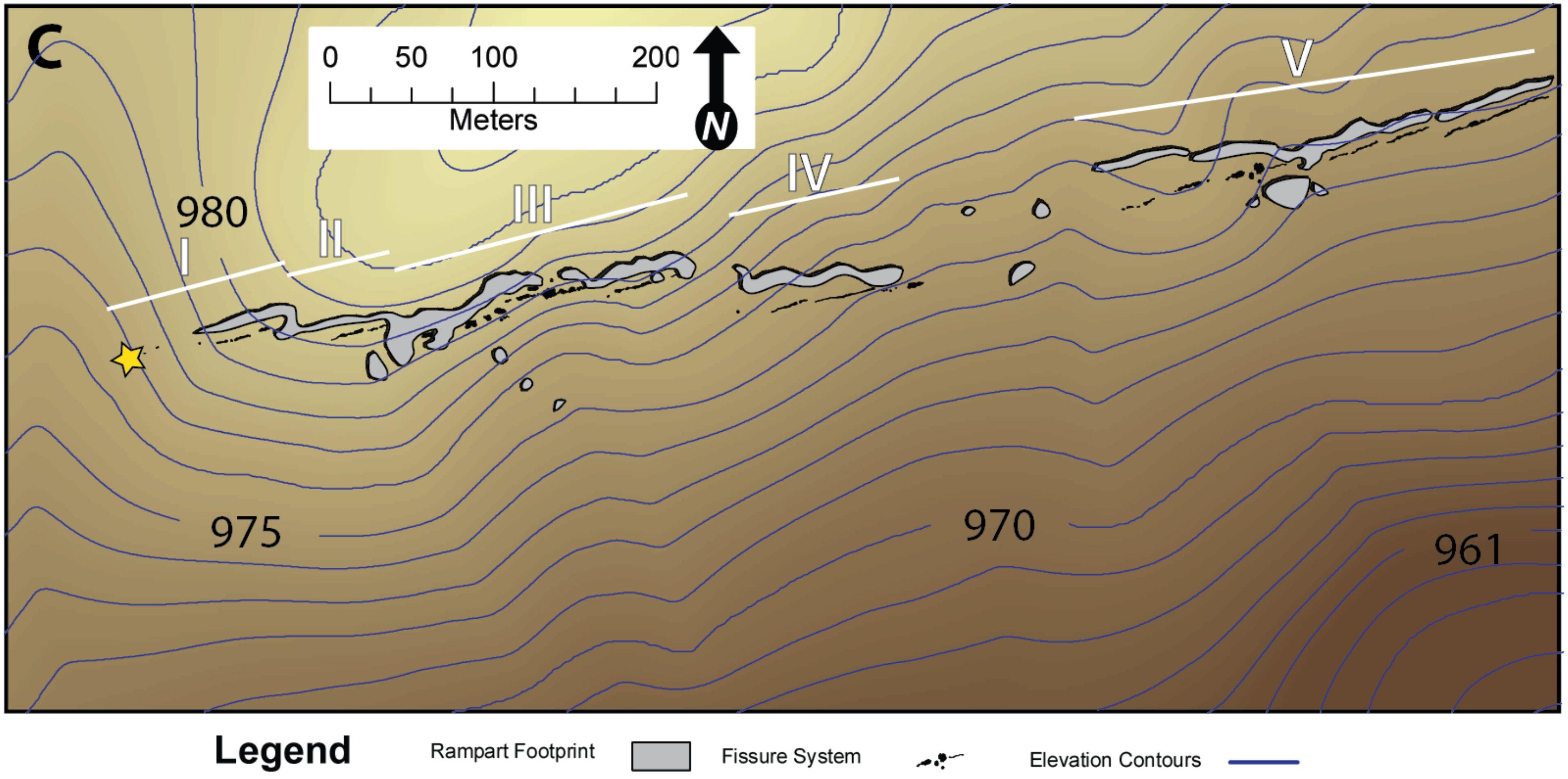

Figure 2.2 continued C Digitally re-created pre-eruption surface topography with the rampart footprint superimposed.

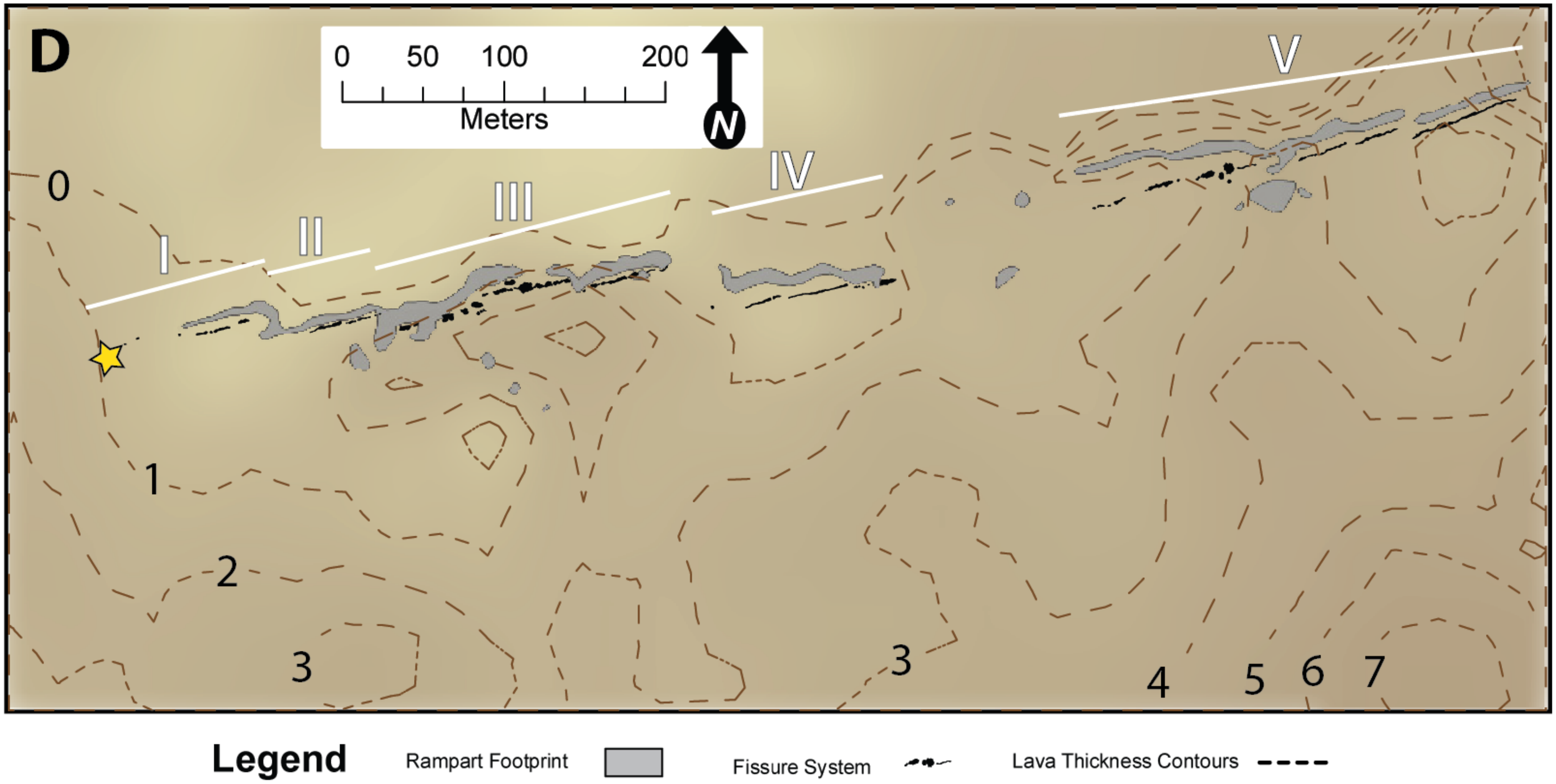

Figure 2.2 continued D Contours of present-day lava thickness remaining on surface (i.e. lava erupted from WZ, not including drainback) up to 120 m south of the fissure.

Table 2.1 Table showing the length, orientation, and distance from the reference point (yellow star, Fig. 2.2a) of each fissure segment in the field area and the gaps between them. The number of vents along each fissure segment is also listed, but will be discussed in chapter 3.

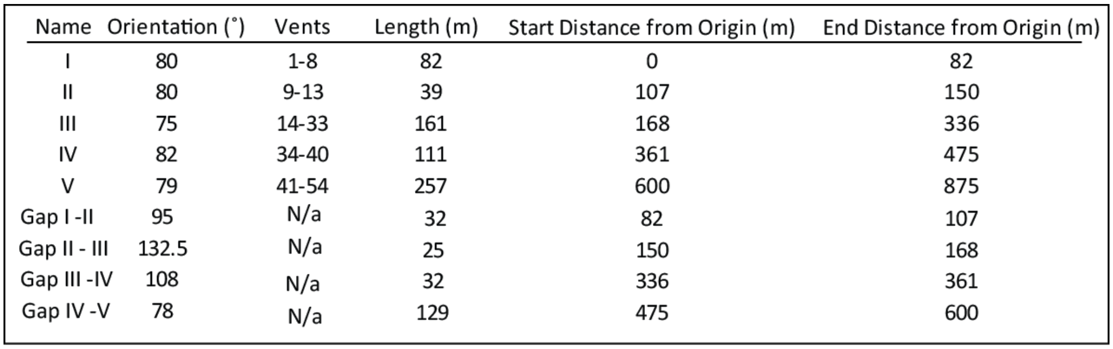

Name	Orientation (˚)	Vents	Length (m)	Start Distance from Origin (m)	End Distance from Origin (m)
I	80	1-8	82	0	82
II	80	9-13	39	107	150
III	75	14-33	161	168	336
IV	82	34-40	111	361	475
V	79	41-54	257	600	875
Gap I -II	95	N/a	32	82	107
Gap II - III	132.5	N/a	25	150	168
Gap III -IV	108	N/a	32	336	361
Gap IV -V	78	N/a	129	475	600

250 × 900 m area bounded by the outer edge of the lava flows in the north and the non-eruptive crack in the south. A reference point of origin for the fissure was taken as the westernmost exposed vent and is the location from which distances in the dissertation are measured (Fig. 2.2a, yellow star). Based on rampart continuity and en echelon offsets between groups of vents, I divided the fissure into five segments (Fig. 2.2a, Table 2.1), labeled as I–V from west to east.

A 1965 contour map of the pre-eruptive Mauna Ulu region was digitized, and five small lava flows erupted in the area of interest between 1965 and May 1969 were added to produce a 0.5 m resolution pre-eruptive topography of the Mauna Ulu area (Fig. 2.2b). This pre-eruptive topography was then subtracted from the current digital elevation model to obtain the thickness of lava preserved in the WZ (Fig. 2.2c). Syn-eruptive topography (maximum lava height) and post-eruptive (current ground surface) topography were derived from a series of kinematic global positioning system (GPS) transects (0.1 m resolution) both parallel and orthogonal to the fissure (Fig. 2.2d).

2.2.2 Characterizing rampart geometry and tephra dispersal

Rampart transects at 40 northern and two southern locations were made with a tape and compass. Each transect orientation was perpendicular to the steep inner rampart wall, and length measurements and slope angles were measured with the aid of a straight-line guide. A cross-sectional rampart area was calculated by drawing the profile for the transect and dividing it into a series of polygons based on obvious changes in rampart slope (Fig. 2.3c) that could

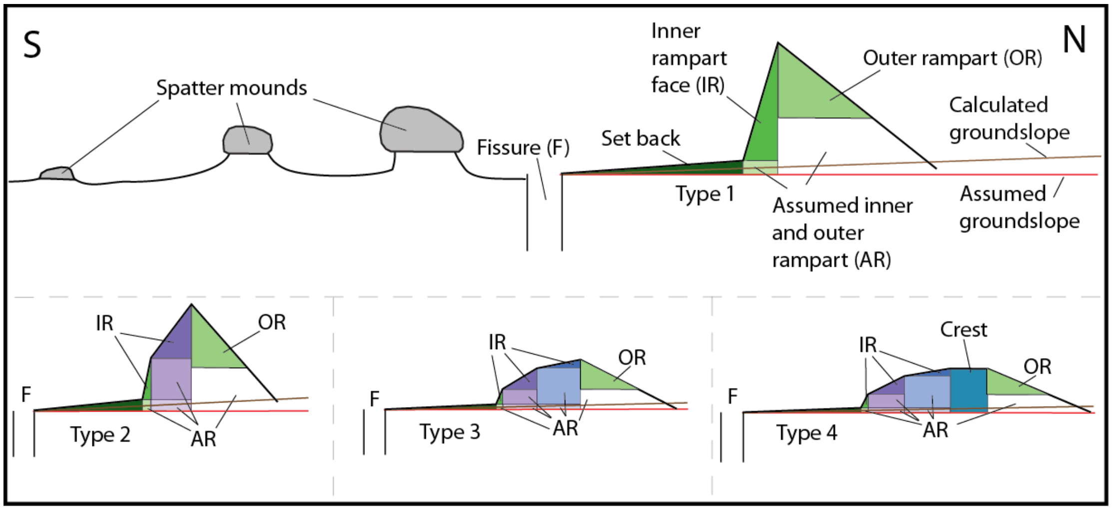

Figure 2.3 Cartoon cross-section of agglutinated spatter deposits. North is to the right of the figure. Cross sections measured the set back distance (fissure to base of the inner rampart) and inner and outer rampart faces (darker triangles). Volume calculations account for presumed spatter (lighter squares) that could not physically be touched, and initially used a flat ground slope (red line), but were corrected (brown line) after Fig. 2b was generated. **Top**: Full representative cross-section. To the south, spatter mounds are present; to the north, a Type 1 rampart (most common) that has 1 inner rampart face. **Bottom**: half cross sections of rampart variations: **left**- Type 2 rampart (two inner rampart faces), **middle**- Type 3 rampart (three inner rampart faces), and **right**- Type 4 rampart (three inner rampart faces and a flat crest).

.

then be converted into 1 m wide unit volumes. Pre-eruption ground slope was measured from the digitized pre-eruptive digital elevation model (DEM), approximated as a single triangle at the base of the rampart cross sections, and subtracted from the volume calculated for each 1 m wide transect. Spatter dispersal was estimated from slope measurements of the outer rampart and quantified through calculations of deposit thinning half-distances (Pyle, 1989). In addition, thinning half-distances were calculated for two transects through aligned spatter mounds south of the fissure where relics of widespread tephra fall were preserved.

2.2.3 Characterizing lava flow directions, volumes, and stagnation times

Lava formed a pāhoehoe flow field in which the following features were analyzed: large-scale drainage pathways, local flow directions, prominent flow features (that is (i.e.), bow waves and wakes), lava crust thickness, heights/locations/thicknesses of lava shelves, maximum lava inundation heights, and localized ground slopes derived from pre- and post-eruptive elevation changes. Lava cooling times (*t*) were calculated from average crustal thickness measurements (*c*) for a range of features (Hon et al., 1994):

$$t = 164.8(c^2)$$

The reconstructed flow thickness data (Fig. 2.2b) were used to calculate the lava volume that remains on the surface, i.e., total erupted lava volume less the amount of lava that drained back into the fissure.

2.3 Eruption observations

Visual documentation of the May 24, 1969 eruptive activity is limited to four aerial photos from Sandia Labratories and 19, previously unpublished, 35-mm slides taken by Hawaiian Volcano Observatory (HVO) staff member Jeffrey B Judd (JBJ). No film footage was taken on that day. Moreover, aside from the mean fountain height estimate, total eruption volume, and eruption rate calculations, no other recorded measurements were found pertaining to May 24 and episode 1. Data presented in this section are derived from a subset of the available photographs, while all published information and unpublished photographs were utilized in the reconstruction of events, which is discussed in the interpretations section. An eruptive fissure panorama could be created from three JBJ photographs, designated in their captions as “PM” (afternoon), taken from an unspecified northern location. Based on the spatial orientation of eruption plumes, and Puʻu Huluhulu’s silhouette, I determined that the panorama was taken from Koʻokoʻolau Crater’s spatter cone and that the eastern fountains are blocked from view. Western fountain heights visible above the forest were determined by a simple geometric ratio of height (*h*) over distance (*D*):

$$\frac{h_{\text{Pu'u Huluhulu}}}{D_{\text{Pu'u Huluhulu}}} = \frac{h_{fountain}}{D_{fountain}}$$

Forest vegetation consisted predominantly of 10 m tall mature Ohiʻa lēhua (Metrosideros polymorpha) trees, which I added to the photographically measured height of each fountain for a more accurate fountain height.

Corrected fountain heights ranged 13–32 m. Our measurements correlate well with Swanson et al. (1979), who stated that the WZ had maximum eruption heights of 50 m. Variations of 10–15 m in fountain height are seen over lateral distances as short as 4–15 m. High, optically dense fountains in the photograph are either single sources or, at most, clusters of three to four vents over a few tens of meters. The visible fountains were triangulated to be from fissure segments III, IV, and V relative to the locations of Puʻu Huluhulu, ʻĀinahou Road, and the location of the photographer.

Weak low fountains or strong continuous spattering are seen above ramparts in the remaining 16 JBJ photographs on May 24. Lack of scale, problems of perspective, and not seeing the base of the fountain preclude measurements of absolute fountain heights from these images. Photos from early afternoon provide a wide view of activity, with one image capturing eight spattering sources varying in fountain height and optical density. Relative height fluctuations were determined by comparing the size of the photo's largest airborne clasts to the equivalent mean maximum clast dimensions measured on the ramparts (37×19×7 cm). Fountains were calculated to vary between 0.2 and 5 m above the rampart crests even though absolute height is uncertain. They are not likely to exceed 8–12 m given the final rampart heights (discussed in next section).

2.4 Rampart geometry and tephra dispersal

2.4.1 Rampart deposits, tephra dispersal, and pyroclast vesicularity

Agglutinated spatter ramparts are nearly continuous on the northern side of the fissure but are present along only two segments on the southern side, along with infrequent small spatter mounds (Fig. 2.2). I have documented four types of rampart profiles (Fig. 2.3). Table 2.2 and Fig. 2.4 summarize the mean and range of parameter values for each type, respectively. Rampart geometry 1 (having one inner rampart face and one outer rampart face, with no flat crest) makes up 86 % of the rampart transect geometries in the field area.

The linear half-distance of pyroclastic fall deposits (distance over which the outer wall of the deposit halves in thickness) scales with mass eruption rate (Pyle, 1989; Wilson and Houghton, 2000). Half-distance values of the northern ramparts are less than 10 m (Fig. 2.5). No distal tephra blanket is present to the north. A single measurement of thinning half distance of the southern proximal ramparts is 11 m. Two transects of southern aligned spatter mounds perpendicular to the fissure yield distal thinning half distances of 21 and 15 m. These data constrain clast dispersal beyond the ramparts, representing what is preserved of a widespread “tephra blanket” segment of the deposit. All the data are compatible with Hawaiian/Strombolian dispersal in the sense of Walker (1973) and Pyle (1989).

Intense welding and rheomorphic flow precluded us from constraining clast geometries along most of the ramparts. One exception is at a site at 155 m, on the west end of segment III, where clasts show no evidence of rheomorphism.

Table 2.2 Rampart types separated into their frequency and mean geometric constraints.

Rampart Geometry	Frequency %	Rampart Transect Mean Volume (m^3)	Rampart Mean Height (m)	Rampart Mean Width (m)	Outer Rampart Wall Mean Length (m)	Outer Rampart Wall Mean Slope (^{o})
Type 1	86	0.37	0.04	15.58	5.81	21
Type 2	7	0.31	0.04	13.36	4.19	35
Type 3	2	0.32	0.05	12.37	4.52	25
Type 4	5	0.59	0.04	23.74	3.57	15

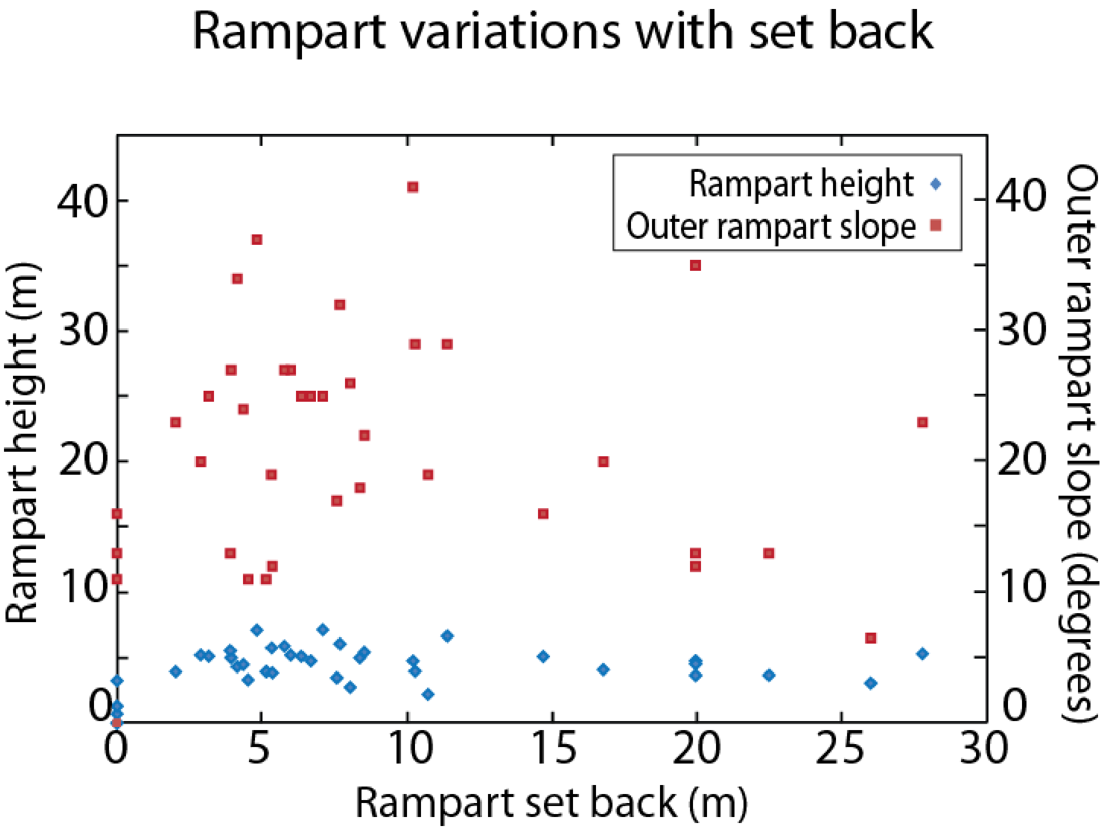

Figure 2.4 Plot showing relationship of rampart height (blue diamonds) and outer slope (red squares) to the set back distance. Data points on the y axis (x = 0) have no vent exposed at the rampart location. Data points on the x axis (y = 0) have no rampart associated with vent exposure.

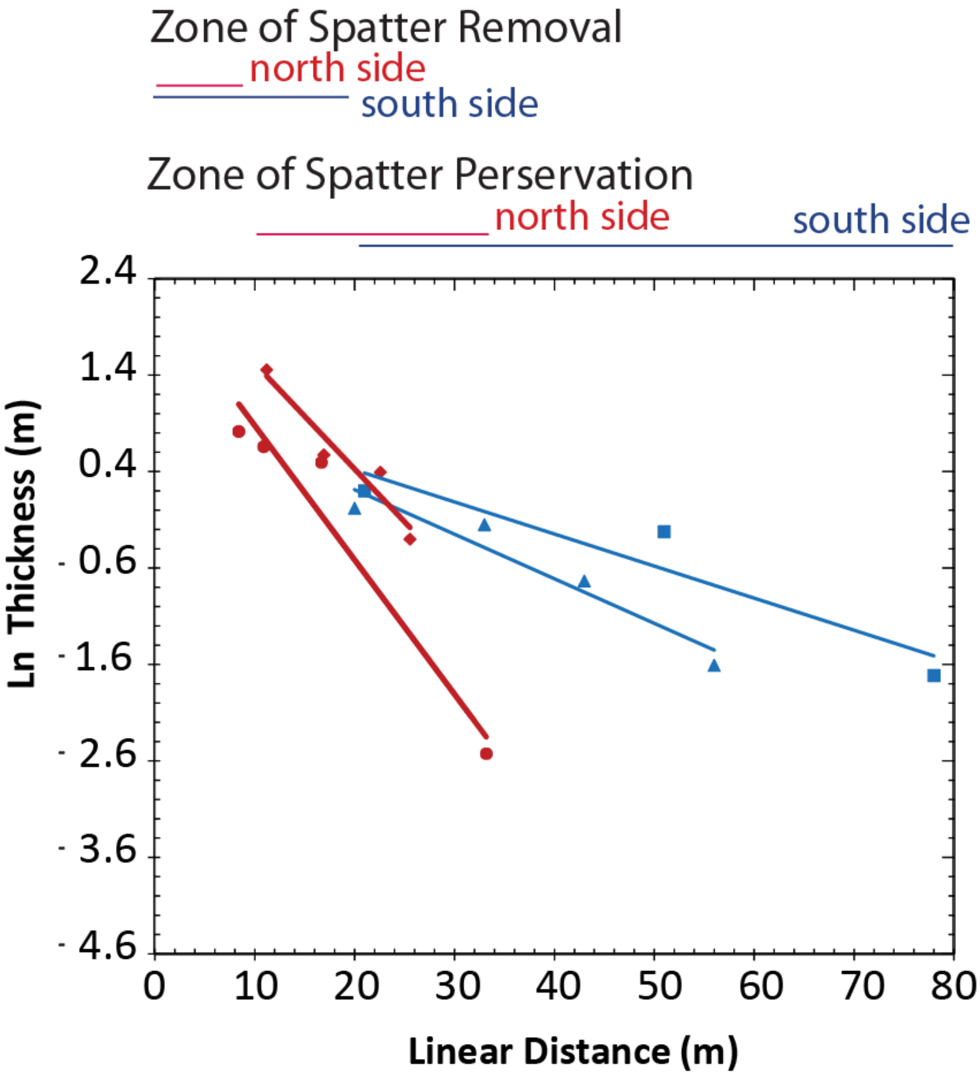

Figure 2.5 Plot of thickness vs. distance perpendicular to the fissure of two full transects. Northern rampart transects (red) show a thinning half-distance of 6 m in the west (shallower line) and 5 m in the east (steeper line), with projected heights of 14 m and 10 m at the vent respectively. Southern spatter transects (blue) show a thinning half distance of 21 m in the west (shallower line) and 15 m in the east (steeper line) with a maximum projected deposit thickness of 3 m at the vent in both cases. Breadths of spatter preservation and removal zones are shown above the plot. The zone of spatter preservation is the range over which spatter was deposited, but was not always preserved. The regression coefficient (R^2) values for all lines range from 0.89–0.95.

Here, maximum pyroclast dimensions were measured in situ, as broadly representative of the rampart grain size (Fig. 2.6a), averaging 15×10×10 cm (range: 2–54 cm wide and 1–15 cm thick). Along the rest of the fissure, pyroclasts margins are rheomorphic (Fig. 2.6b) and strongly agglutinated within tens of centimeters of the rampart exterior. In extreme cases, e.g., at the 466 m and 650 m locations, pyroclasts are completely welded and indistinguishable throughout the interior portions of the broken ramparts. Agglutinated spatter on the rampart exterior contains very sparse but larger vesicles, typically 6×4 cm across. A true diameter of the largest vesicles (>12 cm) could not be obtained because the clasts are broken and incomplete. Vesicle textures of pyroclasts in the interior of broken northern ramparts (distances: 466 m, 650 m, and 707 m) include a mixture of stretched and spherical vesicles. Spherical vesicles are typically 0.30–0.35 cm in diameter (largest vesicle, 2 cm long and 1 cm wide), and sheared vesicles are typically 0.6×0.2 cm (largest 1.4 cm long and 0.6 cm wide, Fig. 2.6c). A separate population of smaller, dense, vesicle-poor, fluidal, and non-welded spatter particles that surrounds many vents is dispersed for only a few meters about the vent.

2.4.2 Northern ramparts

Agglutinated spatter ramparts are present upwind and upslope of the fissure along 80 percent (%) of its length, corresponding to distances of 36–347 m (segments I, II, and III), 368–470 m (segment IV), 554–564 m (between segments IV and V), and 598–887 m (segment V). Parameters that vary along the fissure length include the height, outer rampart slope, rampart setback from

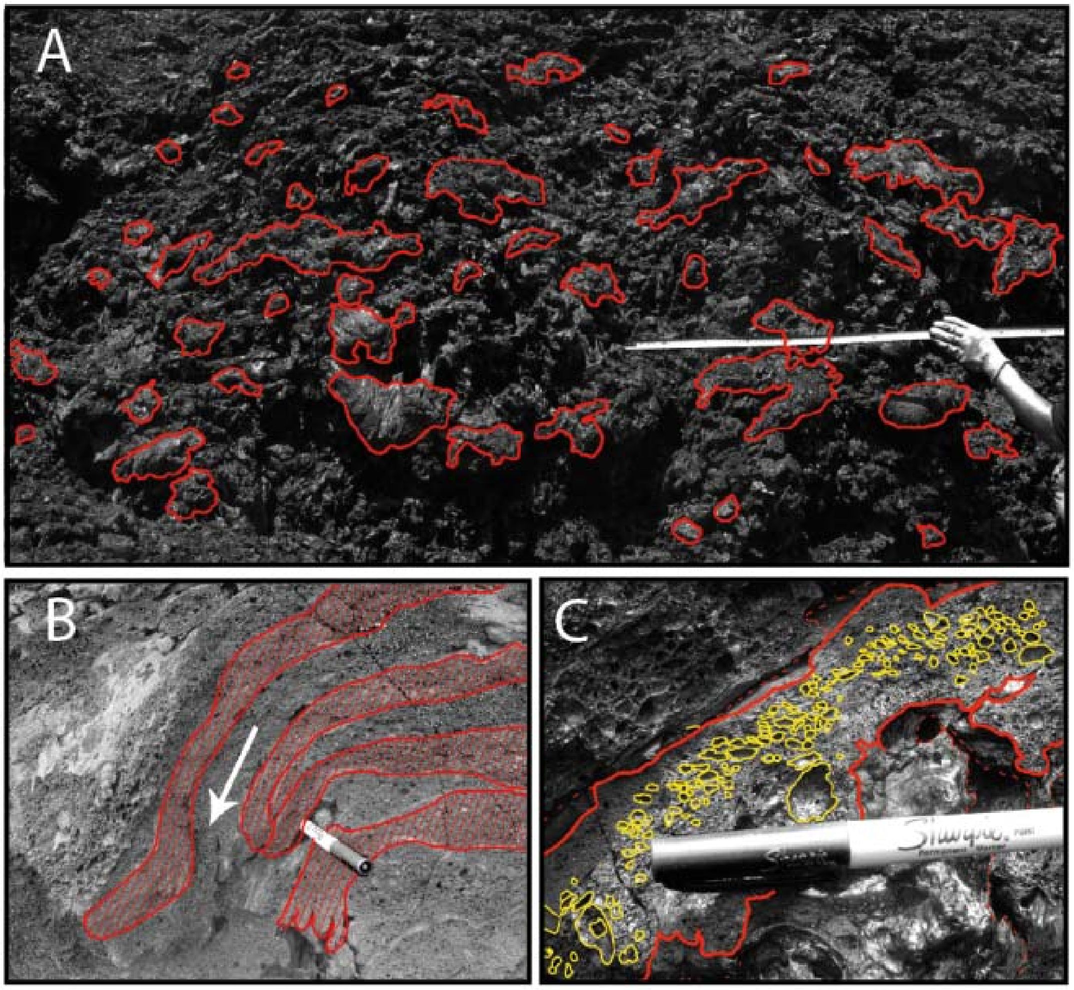

Figure 2.6 A Photograph of weakly agglutinated pyroclasts that retained individual identities with no rheomorphism (at 155 m distance). Some clasts are outlined in red to show complexity of rampart growth. We measured the x and z dimensions (assuming x = y in the depositional plane). The measured z dimension is perpendicular to the depositional surface. **B** Photograph of spatter on inner rampart face at 707 m distance. Clast identities were retained, with 4 hatched in red for emphasis. Rheomorphism was in direction of arrow, down the rampart face towards the vent. **C** Clast (outlined in red) just under surface of inner rampart face at 707 m distance. Vesicles (yellow) are both sheared and non-sheared. Sheared vesicles are elongate both normal to the direction of impact flattening and parallel to flow direction, and are present in the middle of clast above pen. More spherical bubbles are on the left and right sides of clast.

the fissure, and the abundance of tree molds. Rampart height, i.e., maximum deposit thickness, varies along the fissure, ranging from 70 cm to 7.1 m with a mean of 4.4 m. Height variation on the order of 1–2 m occurs over length scales of 2–3 m along the fissure. Outer rampart slope, which reflects the thinning rate, and thus mass discharge rate (Walker, 1973; Pyle, 1989), ranges from 0º to 37º with a mean of 21º. Segment II ramparts (transects four to six) are the only ones close to the fissure (approximately (ca.) 1 m). All other ramparts are between 3 m and 30 m from the fissure. Tree molds are present within a broken rampart at a distance of 560 m, but obvious signs of tree branches or trunks are not present on the remaining ramparts' surfaces (or the outer surface of the broken rampart). Tree molds are also present immediately east and west of the broken rampart between distances of 575 m and 657 m, where northern ramparts are non-existent. In addition, tree molds can be found between distances of 342 and 370 m (segments III and IV), as well as within a 40 m radius of the westernmost vent.

2.4.3 Southern ramparts and spatter mounds

Agglutinated spatter ramparts are found in only two locations on the southern side of the fissure (constituting 5% of exposed fissure length): from distances of 529–548 and 694–721 m. These two rampart segments are each perched at dividing points between major lava pathways (see section 2.5). There are numerous isolated small spatter mounds associated with tree molds on the south side of the fissure to distances of 100 m, i.e., well beyond locations at which the ramparts should have formed.

2.5 Lava flows

The first lava flows from the WZ fissure engulfed 5 km^2 of land immediately surrounding and downslope of the fissure (Swanson et al. 1971). Whereas a velocity was not estimated for the flow front, the lava field had clearly reached Kulanaokuaiki Pali, 1 km south of the fissure, in the aerial photographs (Fig. 2.1c) at 09:40. I assume that fountains fed lava flows continuously between their onset and 09:40 HST, thus allowing a rough calculation of minimum flow front velocities: 0.15 km/h at the old Chain of Craters Road and 0.4 km/h at the old ʻĀinahou Ranch Road. During episode 1, EZ and WZ produced a combined 4.5×10^6 m^3 of erupted lava at an average rate of 40 m^3/s (Swanson et al. 1979).

2.5.1 Paleoenvironment: pre-eruption forest and tree molds

A dense forest originally stood where the lava fields are now located (Swanson et al. 1979), and many, but not all, of these trees became lava tree molds. I have digitized the pre-eruptive ground slope (Fig. 2.7a) and 5,003 pre-eruption trees from aerial photographs, 557 of which have been mapped as tree molds using satellite imagery and a handheld GPS (Fig. 2.7b). It is clear from pre-eruptive aerial photographs that, although tree density did vary slightly, there was no clear "path of least resistance" through which the lava flowed. Figure 2.7b shows over 400 mapped tree molds on the south side of the fissure, which typically have a vertical lava veneer 0.1–0.25 m thick and a total mold diameter of 0.5–0.75 m. The widest tree mold (at 803 m distance and 20 m

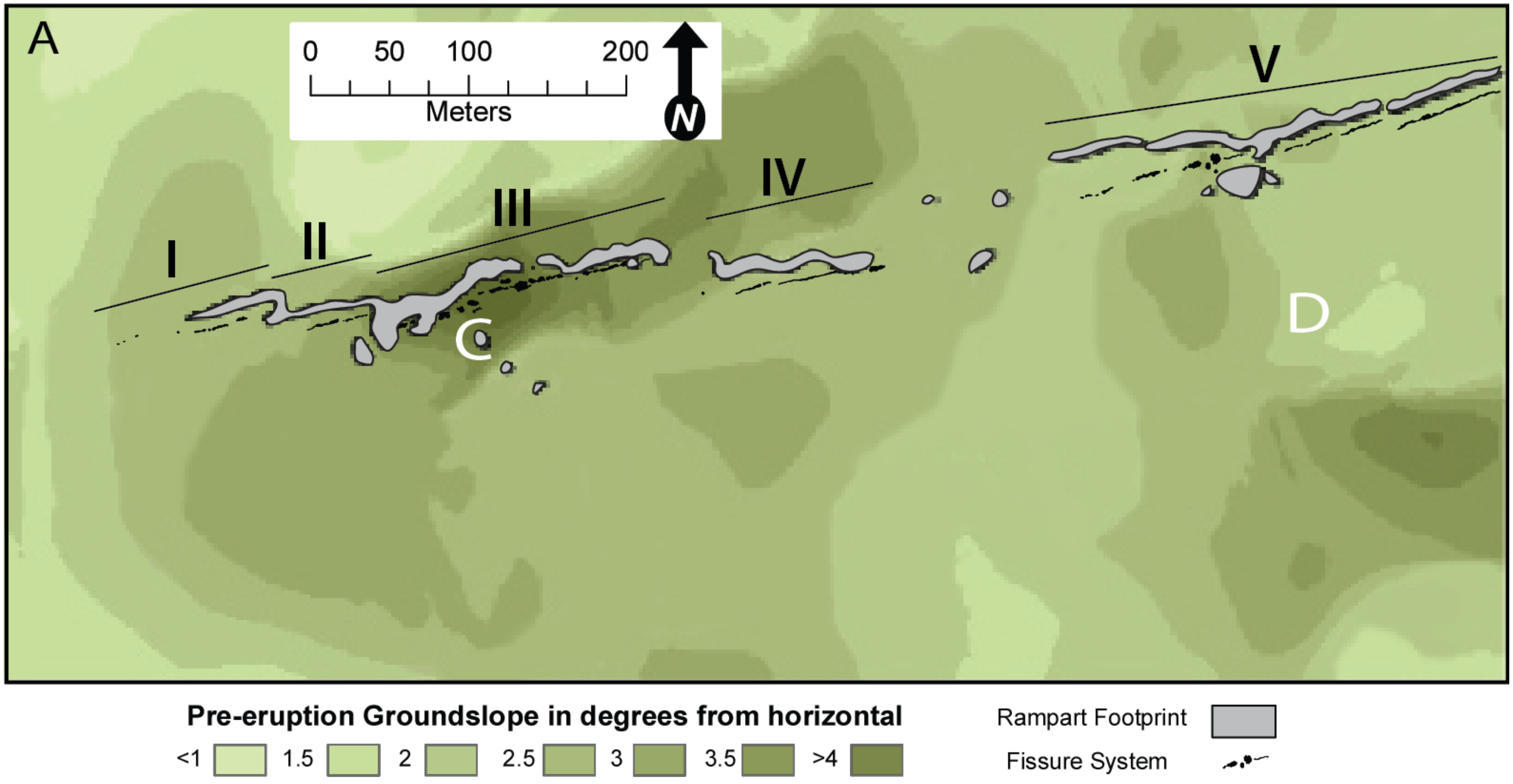

Figure 2.7 A Interpolated ground slope from topography in Fig. 2.2b with ramparts and vents superimposed. Darker shades of green indicate steeper slopes, in gradations of one-half degree. C and D indicate locations of Figs. 2.7c and 2.7d.

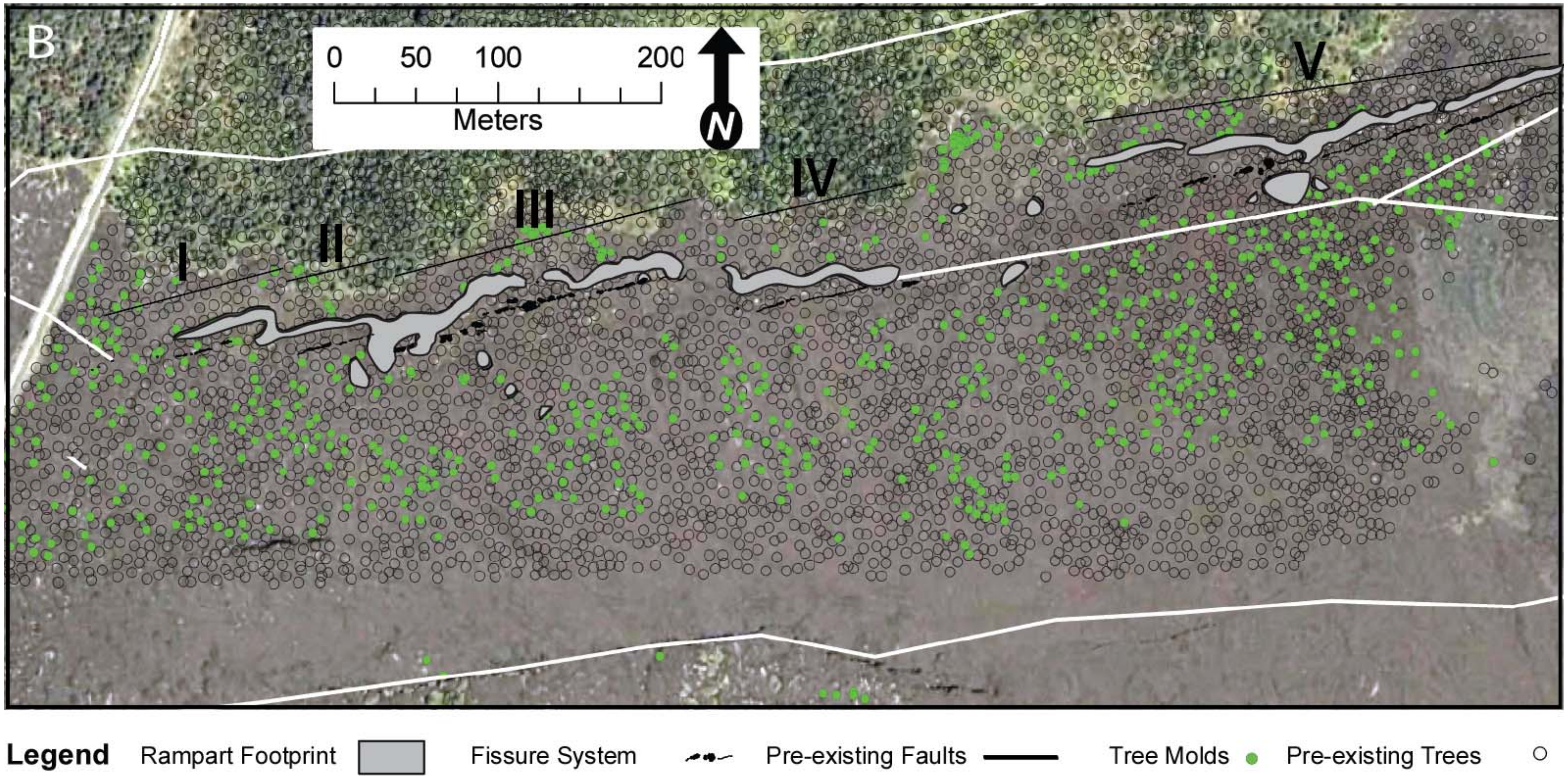

Figure 2.7 continued B Map of forest density and tree molds. Circles outlined in black are trees on pre-eruption aerial photos, green circles are tree molds mapped via field GPS and present-day satellite imagery. White lines are pre-existing faults, mapped from 1965 aerial images.

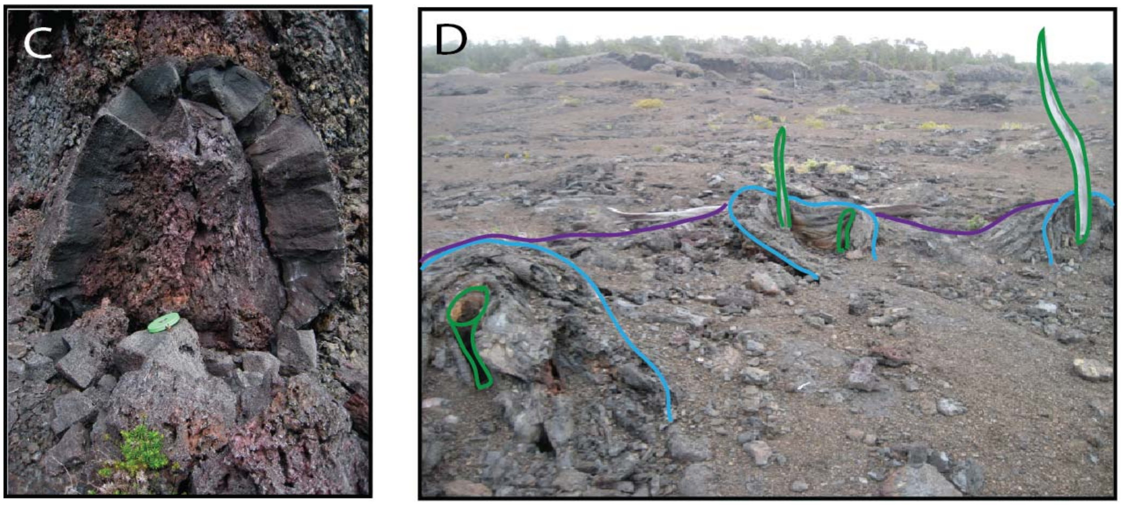

Figure 2.7 continued C The tallest tree mold (1.5 m) in the area (segment III) is unique in being initially constructed of spatter, then covered in lava veneer. **D** Image showing the growth of individual tree molds (blue) into a composite tree mold (purple), creating lava pathways by diverting lava around the trees (green). The three trees span a lateral distance of 10 m.

south of the vent) is 2 m across at the base, but is unbroken, so the lava veneer thickness and internal diameter are unknown. Tree molds located directly adjacent to vents are short and rounded, less than 0.5 m in both height and diameter. The tallest tree mold (Fig. 2.7c) at 155 m distance is 1.5 m high, with a 1 m wide base. The mold itself consists of spatter around a single tree encased in 13 cm of lava (the thickest observed in the field area). In several places, small trees that were closely spaced initially formed individual tree molds, but as the lava continued flowing, they merged into a composite mold and forced later lava to flow around the composite structure (Fig. 2.7d). Large composite tree molds have prominent elevated "bow waves" and elongated wakes. Molds of several tree branches are contained within one broken rampart, but it is unknown whether the remaining ramparts also contain molds of tree branches. Spatter-topped tree molds occur within 100 m south of the fissure. On these tree molds, and other topographic high points, there are often several levels of lava crusts projecting outward as shelves. Three (plus or minus (±) 1) lava shelves are common on tree molds and paleo-highs near the fissure system, and pairs of shelves are present on tree molds and drainage pathway margins farther from the fissure system. Depth to the pre-eruptive ground surface was measured down the middle hole to the ground surface in 10 of the southern tree molds yielding a mean maximum inundation height (top of tree mold to pre-eruptive ground surface) of 1.8 m. Tree molds closest to the fissure have shallower depths (approximately (~) 1 m) than those farther downslope (greater than (>) 2m).

2.5.2 Flow directions and pathways

Most lava drained south from the fissure, following the regional slope. There are six preserved topographic lows (Fig. 2.8a) south of the fissure, corresponding to major lava pathways within the flow field, each oriented north to south (Fig. 2.2). Close to the fissure, pathways have lateral, margin-parallel, ropy folds where thin, newly formed crust was stranded on the flow margins. Southern lava pathways bend eastward 120 m downslope of the fissure. Flow lineations (south and east) in pathways are consistent across the flow surface; a total of 181 flow direction indicators were recorded (Fig. 2.2, Table 2.3).Within southern lava pathways, flow indicators point consistently southward, but between the pathways, flow directions are highly variable. Immediately adjacent to, and on both sides of, the fissure, lava flow directions are inward toward the vents, where drain-back textures are present.

In three locations on the north side of the fissure, volumetrically minor but dynamically important lava flows are present where ramparts are absent: the middle of segment III, between segments III and IV, and between segments IV and V.

2.5.3 Observations of lava crusts

Lava crusts grow while in contact with underlying moving lava (Stovall et al., 2008). Crust thicknesses, whether as the main pathway surfaces or elevated lava shelves, allow us to determine cooling times following Hon et al. (1994;

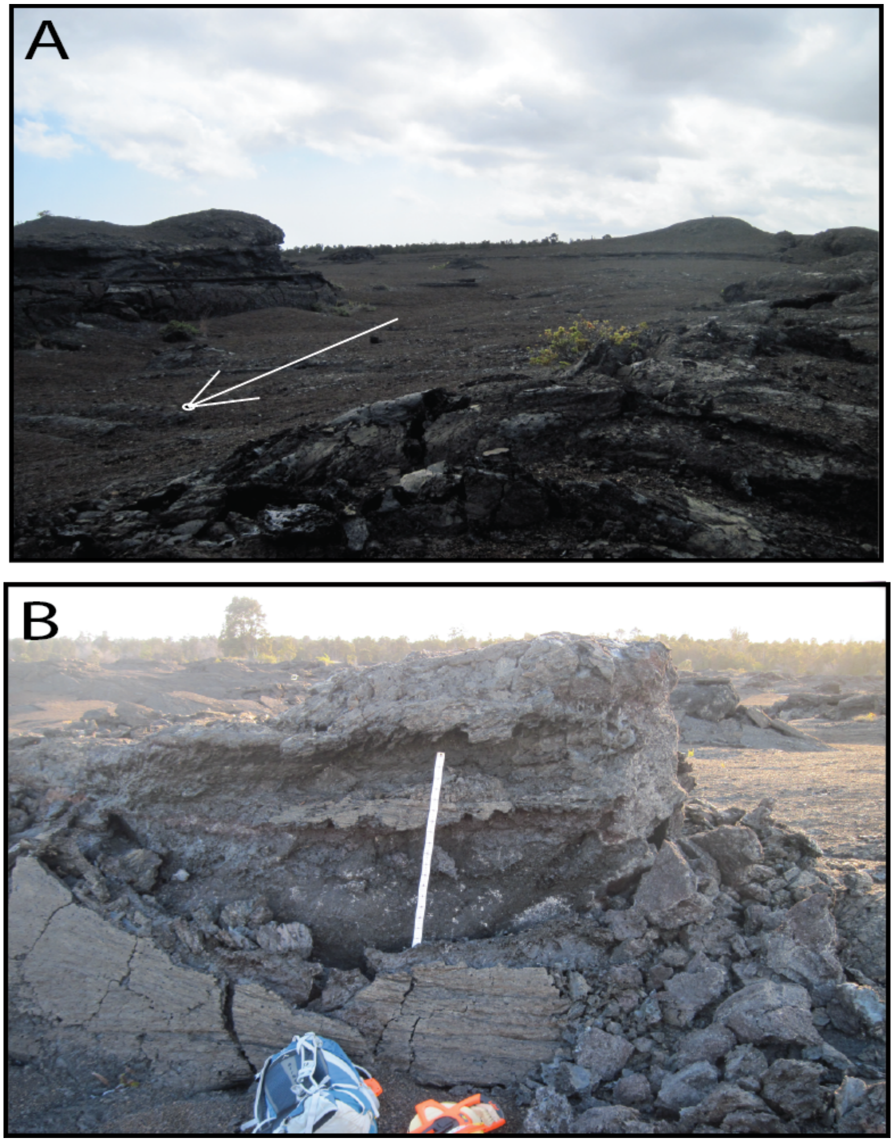

Figure 2.8 A Looking northwest, upslope of one of the major drainage pathways. White arrow indicates direction of flow (south), and is placed in center of pathway. **B** Lava shelves with a meter stick for scale, crossing the lower shelf. Flow lineations occur on the upturned crust between the meter stick and the backpack.

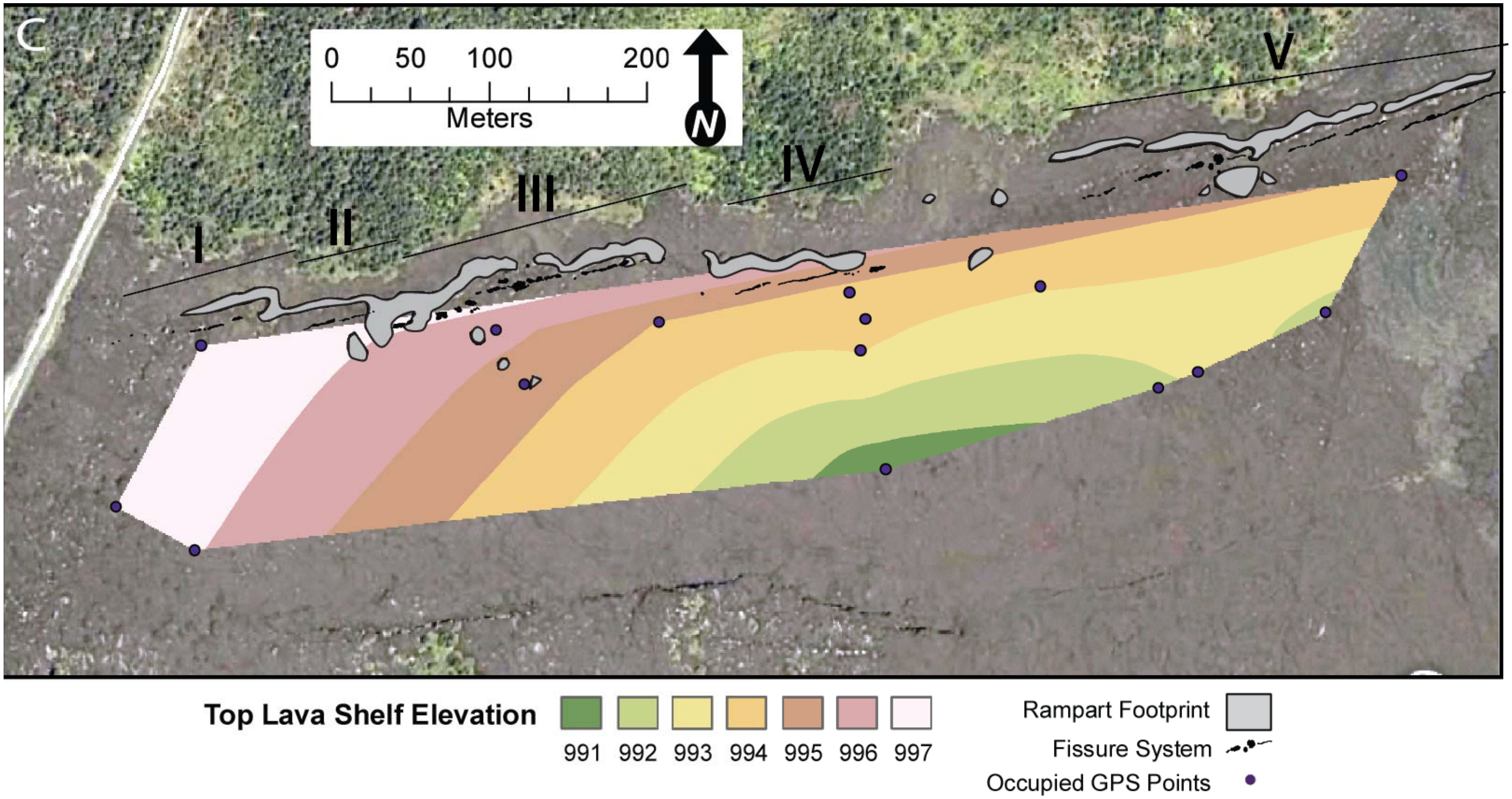

Figure 2.8 continued C Satellite image of field area where forest and lava flow field are same coloration as Fig. 2.2a. Map contouring the elevation of the highest lava shelves, measured at the kinematic GPS locations shown. Elevation decreases to the southeast in 1 m intervals.

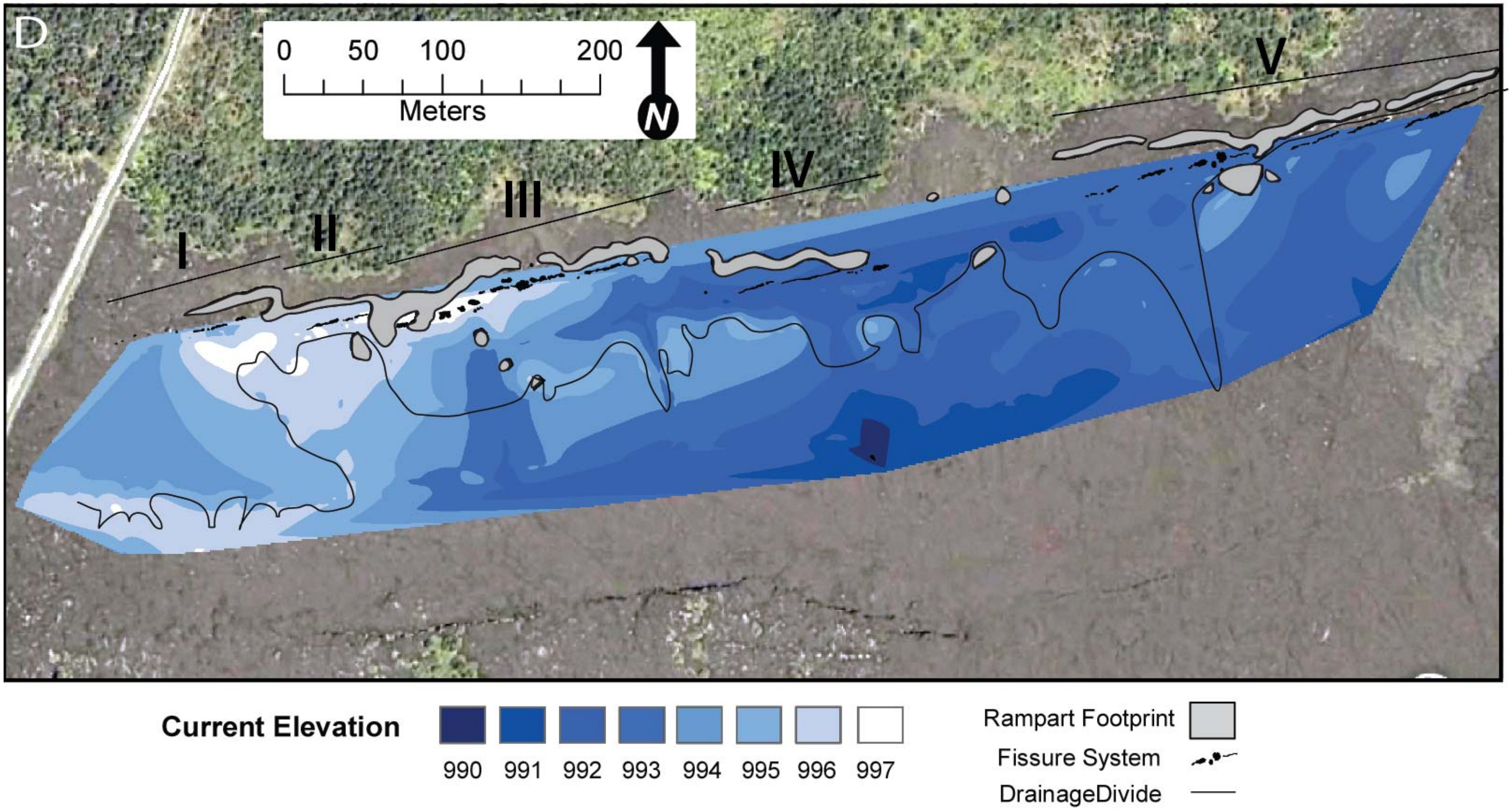

Figure 2.8 continued D Kinematic GPS-derived ground topography from transects shown in Fig. 2.2b. Black irregular line is a “lava drainage divide” showing where present elevations indicate lava drained back into the fissure after fountain activity stopped (north) or continued into the flow field (south). The lowest elevation along the fissure is between segments IV – V.

Table 2.3 Mean values of lava data, including flow directions, crustal thicknesses, calculated crustal growth/lava stagnation times, and shelf heights above the ground surface (where present).

Mean Flow Direction N of Ramparts $(^{o})$	Mean Flow Direction S of Ramparts $(^{o})$	Lava Crust Mean Thickness (cm)	Mean Lava Stagnation Time (hr)	1st Lava Shelf Mean Height (where present) (m)	2nd Lava Shelf Mean Height (where present) (m)	3rd Lava Shelf Mean Height (where present) (m)
352	164	10	1.9	1.70	1.19	.72

Table 2.3), which help define the durations of different stages in the evolution of the flow field.

Crustal thicknesses on the short flows north of the fissure average 10 (±4) cm, equivalent to 90 min of crustal growth. Areas between the major southern pathways' show a wider range of crustal thickness up to 24 cm, equivalent to a maximum of 9.5 hr. Drainage pathways crusts average 9 (±2) cm thick, equivalent to only 80 min of crust growth. Thin, inward dipping, near-vent crusts that characterize drainback into the fissure at the end of the eruption are typically 5 (±1) cm thick, equivalent to 30 min of growth. The relative timings of drainback crusts across different vents, however, are ambiguous.

Thicknesses of preserved lava shelves on topographic high points (Fig. 2.8b) record the durations of relatively stable conditions with matching discharge and drainage rates. Figure 2.2 shows the locations of all the shelf thickness measurements. The uppermost shelves preserved near the fissure are up to 2.5 m above the pathway surface, and have 6–9 m thicknesses correlating to 40–120 min of crustal growth. The lower crusts are generally thinner, 4–10 cm, corresponding to 15–100 min of growth. Farther from the fissure, upper crust thickness and cooling times (7–9 cm, 48–80 min) are similar to proximal sites, but heights range up to 1.5 m above the pathway surface. The single lower shelf, ranging 6–11 cm thick, corresponds to 40–120 min of crustal growth. Elevation of the highest lava shelves gradually decreases southeastward across the field area from 996 m above sea level (asl) at segments I and II to 991 m asl south of segment V (Fig. 2.8c). In contrast, the final surface of the lava (current ground surface) shows a complex pattern of late-stage draining. The boundary between the two different flow regions is plotted as a thin, irregular, solid black line on Fig. 2.8d. The kinematic GPS height measurements (Fig. 2.2d) show the elevation of the highest lava shelves (Fig. 2.8c) and ground surface after draining (Fig. 2.8d).

2.6 Interpretation

Episode 1 in the WZ consisted of three phases: (1) a short interval of fissure propagation, waxing fountain discharge, and lava inundation; (2) vigorous sustained fountains reaching maximum heights of 50 m with sustained and stable discharge and dynamic ponding of lava; and (3) waning fountain discharge, discontinuous fountaining activity, and lava drain-back into the fissure. There are no direct records, however, of the durations of these phases within the 17.25 hr WZ eruption timeframe. Next, I discuss indirect ways of constraining these phases, as summarized in Table 2.4.

2.6.1 Eruption dynamics

The opening phase of the WZ eruptive activity was likely characterized by voluminous production of fountain-fed lava flows along the whole fissure due to the fact that the flow field was at full length and width by 09:40. The area between segments IV and V has the lowest pre- and post-eruption elevations, thickest lava crusts, and highest lava shelves (4 m) along the whole fissure, and has neither northern ramparts nor exposed vents. I suspect that these

Table 2.4 Revised and enhanced chronology of May 24, 1969 activity. This table summarizes the physical processes that acted at various times during the 18 hr of activity.

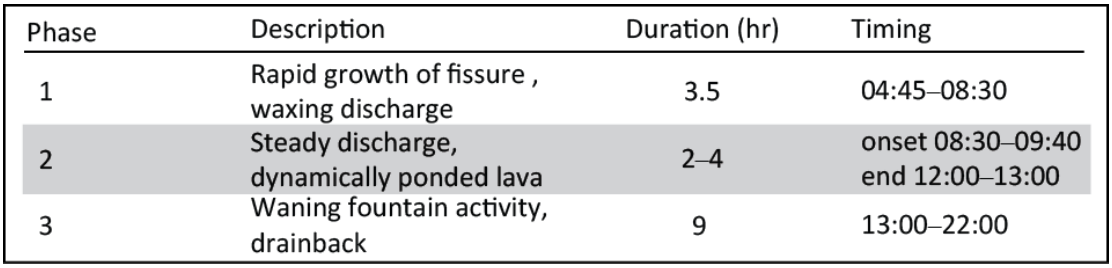

Phase	Description	Duration (hr)	Timing
1	Rapid growth of fissure , waxing discharge	3.5	04:45–08:30
2	Steady discharge, dynamically ponded lava	2–4	onset 08:30–09:40 end 12:00–13:00
3	Waning fountain activity, drainback	9	13:00–22:00

observations can be accounted for by a sustained effusion during phase 1 that flooded this low-lying area, precluding rampart formation during all phases.

Along the entire fissure, tree molds formed as lava inundated the forest, growing thicker as long as the tree mold was submerged in lava. Rampart formation also likely began at this time, with spatter establishing a solid base north of the fissure and to the south on both paleo-topographic highs and around trees close to the fissure.

Our investigation into the lava features along the crack labeled in Swanson et al. (1979, plate 1) as “April 1970” indicates that the crack was open on May 24, 1969, and then reactivated in April 1970. The pre-eruption width of the crack is unknown due to vegetation in the aerial photographs, but flow textures suggest that lava initially flowed into it, but then bridged it and continued flowing down slope in phase 1, eventually ponding against Kulanaokuaiki Pali.

During peak flow (phase 2), all pre-existing paleotopographic highs within 20 m of the fissure were covered by at least 1 m of lava, but on average the lava surface was approximately 2.5 m higher than the present pathway surface. Figure 2.8c indicates that, at this time, the flow of lava was consistently downslope away from the fissure, and most of the flow was directed southeastward following the preexisting ground surface. The lava was thus behaving as a dynamically ponded sheet flow with meter-scale variations in flow depth. Fountain height and intensity varied greatly, not only laterally along the fissure, but also temporally. At this stage, fountains must have erupted through (and entrained portions of) ponded lava in the vents. High pyroclast accumulation rates did not lead to rampart construction, especially in the south, because falling spatter in areas of lava drainage were carried away, except for those pyroclasts that landed on paleo-highs and tree molds. A small volume of lava flowed around the northern ramparts, covering the bases of the outer ramparts. Crustal thicknesses reflect an early emplacement and onset of crust formation in a stable environment, suggesting growth contemporaneous with rampart construction. Lava trapped between the fountains and the inner walls of the northern ramparts undercut the rampart bases. I suspect that this undercutting was thermal instead of mechanical, as the newly formed ramparts were likely a similar temperature to that of the lava ponded against it, thereby decreasing the thermodynamic barrier needed to allow thermal erosion. I postulate that any broken and cracked ramparts may have been destabilized by this undercutting and subsequent removal of the lava support during the last eruptive phase. Tree molds record the maximum inundation height but give no direct growth duration as the cooling relation of Hon et al. (1994) cannot be used for the condition of lava crusts excluded from contact with the atmosphere.

Ultimately, after peak flux, the drainage rate away from the fissure exceeded the declining lava supply from the fountains (phase 3). The panorama photograph from Koʻokoʻolau Crater shows that activity waned inward from both ends of the WZ. The westernmost fissure segment had the simplest and shortest history of inundation and drainage, and does not show a complex pattern of drainage during phase 3. Most lava continued to drain southward, but some began flowing back into those fissure segments that had ceased fountaining. Near-fissure crusts show a lack of flow indicators and reflect relatively passive drainback beneath fixed crusts at this time. Lava reentered the fissure along its entire length after fountain activity stopped. At this time, southward flow focused to the major pathways and surface flow indicators formed. Lava shelves indicate periods of relatively constant lava flux as opposed to periods of actively waxing or waning flow. The presence of multiple lava shelves suggests that the waning discharge rate was incremental with one or more periods of relative stability during the decline. A complex boundary exists between late-stage lava that drained back into the fissure and lava that continued to flow downslope (Fig. 2.8d).

2.6.2 Variability of fountaining along the western fissure

High points on the ramparts are not always coincident with the highest fountains as seen in single photographs. In the extreme case, images from old ʻĀinahou Road looking to the east show high ramparts with no fountains, indicating an early high rate of accumulation and rapid rampart construction over a short period. Fountain intensity and height for those areas shown in the photographs may have been at a maximum early in the eruption, producing other high ramparts. Alternatively, the high fountains may correlate with the rampart lows if the accumulation rates were sufficient enough to cause rheomorphism. However, the whole WZ did not erupt with equal intensity during the full 17.25 hr of activity and rampart-derived, time-averaged eruption rates are therefore a minimum estimate of instantaneous eruption rates during fountain activity.

2.6.3 Chronology

Phase 1 (inundation and increasing fountain activity) lasted from 04:45 to 08:30, by which time the whole western fissure was active. Based on the literature and eyewitness reports, I assume that the WZ fountains began sequentially and rapidly, with the easternmost fountains starting up to 3 hr before those in the west. I infer that phase 2 (steady peak flux) was underway by 09:40 because the aerial photograph taken at that time indicates vigorous fountaining of all segments and a well developed flow field. The highest lava shelves created during maximum inundation formed over a period of 40–120 min, a minimum estimate for the duration of phase 2. The duration of phase 3 (waning) can be estimated from the thickest crusts present between lava pathways to be approximately 9 hr. This suggests the waning phase began around 13:00. I conclude that phase 2 had a duration of no longer than 4 h (~9:00 to ~13:00), ending between noon (in the west) and early afternoon (in the east).

In the far west, fountaining either did not take place from the fissure or had such low height, weak intensity, and/or short duration that any spatter deposits were subsequently buried by lava flows emanating from segments I and II. Segments I and II ceased fountaining next (certainly by early afternoon, before ground photographs were taken). Lava from segments III, IV, and V did not reach segments I or II. The gap between segments IV and V was likely to have been a major draining path for lava within the drainage divide, and fountains there probably died early (between late morning and mid afternoon), although this section has the most ambiguous timing estimates along the whole

WZ. Fountain cessation in the gap may have been induced by drowning (Wilson 1980), because this area was (and still is) the lowest topographic point along the fissure and would have contained the greatest depth of ponded lava in and above the vents. Given that fountains along segment V were weak or absent in the mid to late afternoon, I conclude that activity ceased here earlier than at segments III and IV. Drainage into segments III, IV, and V is unlikely to have started before late afternoon or early evening (i.e., until after the ground photos were taken). I conclude that the gap between segments IV and V continued draining lava away from the fissure after all fountains had ceased because flow indicators point west toward segment IV where obvious drain-back textures cover the surface lava. Absolute elevation of this gap is lower than that of the vents in segment IV and the ground slope dips toward the gap between these two segments. Lava drainage in each fissure segment presumably ended in the order of segments I and II, followed by segment V, then segments III and IV, and finally ending in the gap between fissure segments IV and V.

An important conclusion drawn from the observations is that transitions between phases were not isochronous along the fissure. Lava almost certainly drained into some portions of the fissure (segments I and II) while fountains still erupted from other portions of the fissure (segments III, IV, V). At the cessation of all fountaining activity, lava re-entered the fissure along its entire length.

2.7 Discussion: asymmetry and absence of fissure eruption ramparts

The May 24, 1969 spatter deposits reveal an interesting paradox. Spatter is preserved only locally south of the fissure, but our estimates, based on the sparse preserved deposits, suggest that twice as much material fell in this downwind region than in the northern upwind region, which is characterized by a high, near-continuous rampart. If this is so, what was the fate of the “missing” spatter falling to the south? I propose that two mechanisms removed spatter clasts downslope from the fissure. Proximally, pyroclasts falling within 20 m of the fissure to the south formed spatter-fed flows and within 10 m to the north became impounded lava; in both cases, any sense of pyroclastic “identity” was lost. Farther downslope (>20 m) on the southern side, spatter fell as discrete clasts but was rafted away on moving flows. The local southern preservation of pyroclasts on tree molds and paleo-highs is proof that distal material fell cooler in this region and could be locally preserved as it did not rheomorph or get transported downslope. A total absence of spatter on the lava flow today clearly indicates that flows continued moving after the cessation of fountaining. Upslope, to the north of the fissure (>10 m), a volumetrically minor amount of spatter-fed lava was both impounded by the fountains and occasionally flowed around the ramparts (which were able to form and grow because the lava could not readily flow to the south).

Figure 2.9 shows schematic snapshots through the eruption and the physical processes that I believe led to the near absence of ramparts on the south side of the fissure. Phase 1 low fountains (Swanson et al., 1979) fed early lava that drained downslope, southward, carrying away most of the early spatter as it was deposited (Fig. 2.9a–b). Some spatter congealed on branches of trees, and lava engulfed tree bases, with heat from the newly formed lava crust igniting some trees. Increasing mass eruption rate during phase 1 caused dynamic ponding of the lava flow, burying the remaining trees more deeply, allowing stable crusts to form and attach to the tree molds. Spatter fell continuously beyond 20 m from the fissure but was transported downslope on the flowing lava, except where it landed on the stable crusts anchored to tree molds or other topographical high points (Fig. 2.9c). With waning discharge rate, the level of the lava flow dropped (Fig. 2.9d), exposing the spatter-covered mounds at heights of 1–2 m above the present ground surface (Fig. 2.9e).

The asymmetry of other rampart deposits is covered only fleetingly in the literature. For Kīlauea fissure eruptions, typically the cumulative vent length (e.g., fissure length) is stated along with a phrase to the effect “a rampart was constructed.” There is generally no discussion of whether the rampart(s) is/are a paired unit or a single asymmetrical feature as seen at Mauna Ulu. However, asymmetrical ramparts on Kīlauea are not confined to the 1969 eruption (e.g., October 1963, Moore and Koyanagi, 1969; December 1965, Fiske and Koyanagi 1968), but other fissures have not produced asymmetrical deposits to the same extreme that is observed at Mauna Ulu. In addition, accounts of fissure eruptions in Japan, Italy, and Iceland also simply acknowledge that ramparts formed, but give no dimensions or detailed analysis. In this paper, I have presented new data sets to better quantify, understand, and model the dynamics and products of low Hawaiian fissure fountains.

Figure 2.9 Cartoon series showing progression and formation of asymmetrical spatter ramparts (looking west). For simplicity, details of subsurface structures (i.e., tree roots, previous lava flows, etc.) are not shown. In panels a-d, pyroclasts are color coded (hot = orange, moderate = red, cool = grey) and arrows in the lava show flow direction. For all panels, black lines around tree trunks are tree mold crusts both within the spatter rampart to the north (right) and in the lava flow field to the south (left and center). **A** Fissure initiation in phase 1. **B** Lava rapidly engulfs the forest as magma flux and fountain height increases during phase 1. Tree mold and rampart formation begins, trees near fissure start to burn, and lava flows transport spatter downslope.

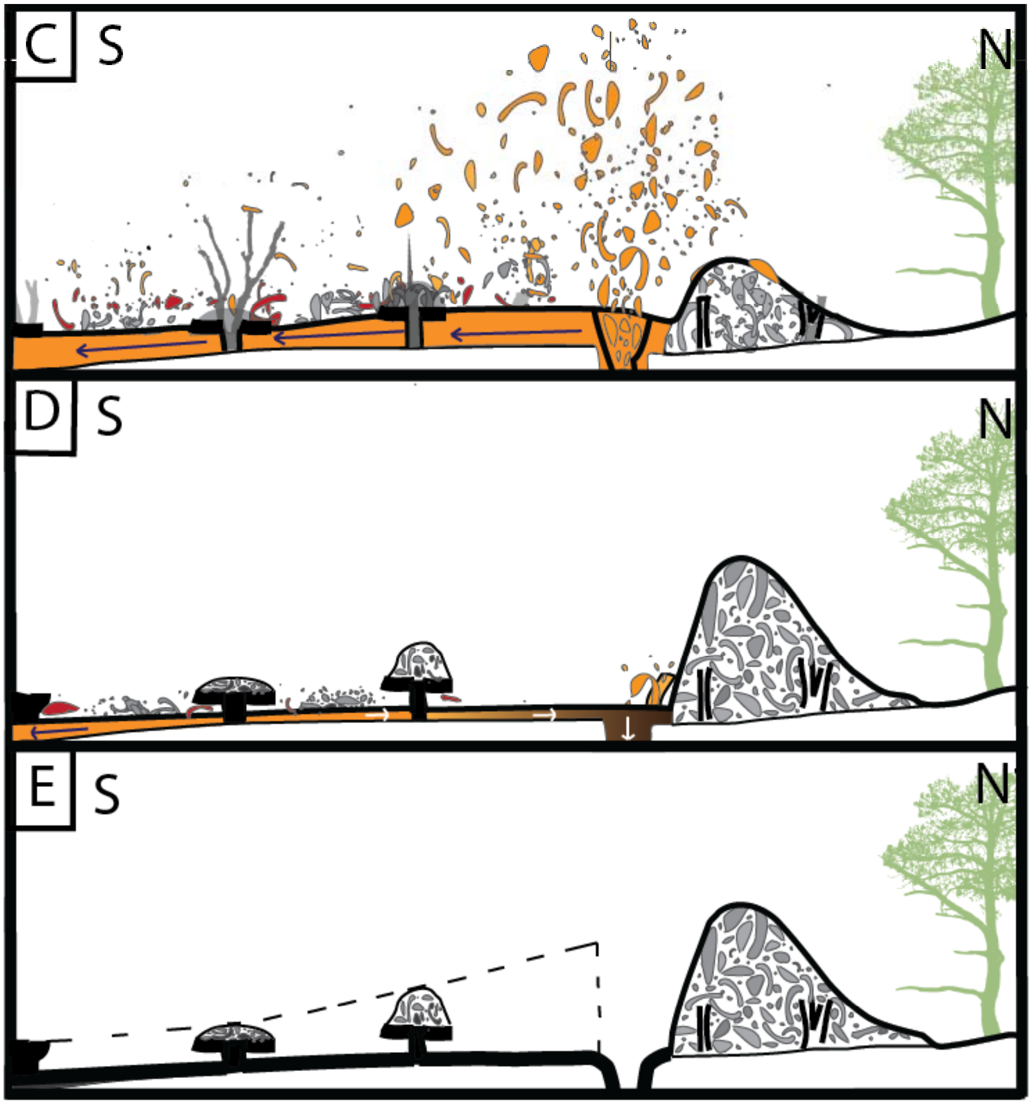

Figure 2.9 continued C During phase 2, peak flux creates dynamically ponded lava flows. Ramparts and tree molds continue to grow, trees continue to be incinerated, and lava drainage pathways stabilize. A lava bench (thick black line) forms around the top of tree molds and on pathway margins (not depicted). Spatter is rafted downslope, unless it lands on a tree mold, where it accumulates (shaded grey). **D** Incremental fountain decline in phase 3 allows the lava flow level to drop in a stepwise fashion, creating secondary/tertiary shelves (not depicted). Any remaining spatter on the lava is transported downslope. North of the lava divide, lava drains back into the fissure after fountain cessation (white arrows). **E** Dashed line indicates where a southern rampart would have been located if fully constructed. Present topography on the surface of the lava flow is shown by the heavy black line.

2.8 Conclusions

The fissure eruption of May 24, 1969 illuminates a misconception that explosive eruptions always produce thicker deposits downwind from vent. Preserved deposit thicknesses during low fountaining eruptions reflect many influences, including ground slope, the presence or absence of coeval lava flows, accumulation versus deposition rates, local topographic relief, and the wind field. On Kīlauea, symmetrical (paired) ramparts are not always formed during fissure eruptions. For fountaining eruptions of fluid magmas, like basalt, a dynamic balance always exists between processes promoting rampart/cone growth and processes favoring removal of tephra via coeval lava flows. The fissure cutting the ground surface in such a way that down slope was all on the south side of the fissure also aided in the preservation of spatter ramparts and the formation of the flow field. The ramparts of May 24, 1969 show that this eruption balanced at the cusp between explosive (pyroclastic) and effusive activity.

Chapter 3

Hawaiian fissure fountains 2: Vents and shallow conduit geometry, episode 1 of the 1969–1974 Mauna Ulu eruption.

3.1 Introduction

Basaltic fissure eruptions, the most common type of terrestrial eruptions (Sigurdsson, 2000), are poorly constrained due to limitations on our observations of the natural systems (vent and conduit geometry, temporal and spatial variations in mass flux, etc.). The typically agglutinated nature of subaerial pyroclastic deposits and the common burial of vents make quantification and constraint of Hawaiian eruption dynamics a challenging task. Kīlauea's fissure eruption episode on May 24, 1969, which initiated the 5 yr long Mauna Ulu eruption, provides an excellent opportunity to study fissure system geometries and derive input geometry parameters for models of basaltic fountain dynamics. The westernmost 900 m of the original fissure system remains accessible today, to depths that are in places greater than 100 m, because lava drained back into the system, leaving an open cavity that allows quantification of the geometry of much of the vent and shallow conduit system. Here I quantify and interpret the fissure and vent geometry.

3.2 Background

Relevant background information from structural geology, fluid dynamics, and the theory on how fissures are modified by syn-eruptive processes will be useful in discussing the implications of the detailed fissure geometry measurements presented here.

3.2.1 Structure of joints, faults, and fissures

Fractures can develop along cooling joints, through shearing (Pollard and Aydin, 1988) or mode 1 opening (Holland et al., 2006) of these internal rock weaknesses. These fractures can also slip (either dip-slip, mode II, or strike-slip, mode III) in order to accommodate ground shifting/settling or dike injection/propagation. Jagged, sub-vertical scarps along the fracture faces are relicts of initial cooling joints and or bedding planes. As fractures propagate and expand, they react to the local and regional stress fields, altering their propagation direction and opening behavior. A single fracture will splay into en echelon segments if the principal stresses rotate around the propagation axis (Sommer, 1969) with the number of segments proportional to the stress rotation angle (Pollard et al., 1982). Fractures dilate in the direction of least compressive stress (i.e. greatest tensile stress, $\sigma_{t,}$) and propagate in the direction of greatest compressive stress (σ_c). Therefore, when the principal stresses rotate as they approach the ground surface from depth, the crack will realign to the new stress field to conserve energy needed for continued propagation (Pollard et al., 1982). Individual lengths of en echelon cracks are always smaller than the parent crack length (Pollard et al., 1982). Should en echelon segments grow long enough to both react to and join each other, they connect in a manner where the tip of one en echelon segment will bend towards its neighbor, joining it as close to 90º as possible (Pollard et al., 1982).

Jointing of basaltic lava is driven by thermal stress build up within a cooling lava flow (Ryan and Sammis, 1978) or inflation pressure during lava flow formation. Cooling joint crack advance is determined by the cooling rate of the flow (Ryan and Sammis, 1978). Cracks are typically mode I (dilational opening), but can also be a combination of mode I and mode III (out-of-plane shear), or rarely mode I and mode II (in-plane shear). A crack tip propagates through the cooling lava crust into the hot viscous layer immediately beneath it, halting crack growth and creating a textural change in crack appearance from smooth to rough (Ryan and Sammis, 1978). DeGraff and Aydin (1987) showed that joint growth into the lava resulted from new cracks nucleating on the edge of old cracks and confirmed that crack propagation ceased at the brittle-to-ductile transition in the lava crust. Cooling joints can create polygonal shapes that, when extended in the vertical direction, create columns with edge widths (or face widths) averaging 26 cm wide, but ranging from millimeters to tens of meters (Ryan and Sammis, 1978; DeGraff and Aydin, 1987; Dance et al., 2001). Polygonal fracture patterns are common (DeGraff and Aydin, 1987; Aydin and DeGraff, 1988; Dance et al., 2001; Goehring et al., 2006, Goehring and Morris, 2008) and evolve with depth (or length) from tetragonal to hexagonal polygons (Aydin and DeGraff, 1988) where face width is a proxy for polygonal diameter (Ryan and Sammis, 1978).

Magmatic dikes, when propagating to the surface, move upwards by either intruding a self-created and self-propagating crack, or by utilizing pre-existing fractures and joints (when oriented in a direction preferential to propagation) (Delaney et al., 1986; Valentine and Krogh, 2006). Asymmetry of overall dike shape has been attributed to gradients in the regional stress field and/or the dike’s internal magma pressure (Pollard and Muller, 1976). Fracture length, in addition to the stress and fluid pressure gradients, also controls the magnitude of asymmetry. A cross sectional dike shape akin to an inverted teardrop is obtained when the dike driving pressure is constant while the regional pressure is gradational along the dike length (Pollard, 1987). Dikes will segment into systematic en echelon steps when either the principal stress field orientation rotates or if the dike propagates at an angle to the principal stresses (Pollard, 1987). Whereas Pollard et al. (1982) showed that overlapping en echelon steps can create pinching and swelling of the segment tips in an elastic model, recent work by Daniels et al. (2012) demonstrate that dikes tend to be thicker at the ends and thinner in the middle, indicating dike shapes are not consistent with a purely elastic model of the host rock. No correlation was found between a dike’s thickness and its asymmetry in the Daniels et al. (2012) study, and asymmetry is attributed, in order of importance, to en echelon overlapping, host-rock inelasticity, and host-rock property variations. Dike thickness variations can be an effect of host rock inelasticity, but Daniels et al. (2012) also suggest that some of the shape variation can be due to thermal chilling of the dike tips. This chilling along the crack tips acts to prevent the dike from closing fully as the eruption wanes and overpressures drop. The solidified dike tips keep the dike center partially open as overpressure drops, prolonging the duration over which an eruption may continue (Daniels et al., 2012).

An en echelon arrangement of fissure segments is a common geometry for basaltic volcanic systems. Examples include other Kīlauea eruptions (Macdonald and Eaton, 1957; Fiske and Koyanagi, 1968; Moore and Koyanagi, 1969; Richter et al., 1970; Lockwood et al., 1999), as well as eruptions in Iceland (Gudmundsson, 2003; Grant and Kattenhorn, 2004; Jenness and Clifton, 2009), Reunion (Cayol and Cornet, 1997), the Canary Islands (Day et al., 1999), Ethiopia (Ebinger and Casey, 2001; Wolfenden et al., 2004) and the East Pacific Rise (Fornari et al., 2004). Very recent eruptions at Kīlauea have been studied using GPS, Interferometric Synthetic Aperture Radar (InSAR), and tilt data to interpret en echelon geometries. The consistency of strikes and prevalence of en echelon segments at Kīlauea suggest that the overall stress field (near Mauna Ulu) is an interaction of the curved ERZ and the Koʻae fault zone to produce a combination of mode I (tensile) opening and mode III shear cracking (Montgomery-Brown et al., 2010).

3.2.2 Fluid dynamics of fissure eruptions

Theoretical work in the early 1980s (Wilson, 1980; Wilson and Head, 1981) provided a solid first-order foundation for understanding the dynamics of Hawaiian style eruptions. Their calculations cover expected fountain behavior given various factors, including gravity, atmospheric density, magma water content, vent geometry, ascent velocity, fountain spread angle, and fountain height suppression when erupted through ponded lava. A notable improvement from previous models of fissures is the incorporation of a magma/gas mixture, and the pressure of the gas used in driving the explosive eruption (Wilson, 1980).

Minimum vent widths of 0.2–0.6 m were calculated for basaltic fissures erupting 30–500 kg/s per meter of fissure from conduit lengths of 0.5–20 km (Wilson and Head, 1981). Fountain height correlates negatively with magma viscosity and correlates positively with ejecta velocity, mass eruption rate, and magma gas content, where released water (H_2O) content of 0.4% can produce a 500 m high fountain.

Giberti and Wilson (1990) developed this model further to allow for prescribed vent geometry, analyzing the effects of geometry on dike flow to the surface from 1000 m depth. Where previous models that used a prescribed lithostatic pressure saw the vent shape always flare near the surface from sonic or supersonic motion, Giberti and Wilson (1990) constrained the fissure to be 1) straight walled, 2) convergent towards the surface, or 3) of a variable width (lenticular shape). In all cases, and for steady state eruption dynamics, exit pressures and mass discharge are dependent on magmatic source driving conditions. Exit velocities in their simulations, however, are broadly similar to each other because, after material exits the vent, it quickly expands and decompresses to ambient atmospheric pressure. The resulting flow into the fountain cannot be visually distinguished from the lithostatic case with ground observations. Exit pressures are predicted to be greater than atmospheric at the surface but quickly decay to atmospheric pressure, such that the choice of fissure geometry (and therefore lithostatic versus non-lithostatic pressure condition in the ascending magma-gas mixture) is not likely to produce significant differences in fountain structure. They conclude that fissure widths less than 1 m wide are most likely to have non-lithostatic pressure gradients.

Mitchell (2005) further investigated shallow conduit shape and how it changes through time during an eruption. In two scenarios, surface choked conditions (i.e. exit velocity less than or equal to (≤) Mach 1) and balanced lithostatic pressure conditions, vent widening through time allowed the choking point of the flow to descend lower into the conduit. For basaltic fissures, Mitchell (2005) found that wall stresses generally are not large enough to disrupt the conduit walls, even at the surface where they are greatest. He infers that original dike shape is likely preserved in the early part of the eruption, or for eruptions of short duration. Eruptions of longer durations can evolve towards complex vent shapes.

Flow focusing (i.e., vent localization) along a fissure could be fluid dynamically induced in thermo-viscous flow by fingering instabilities (Wylie et al., 1999). “Thermo-viscous” is used by Wylie et al. (1999) to mean a small temperature decrease that induces a large viscosity increase, which causes magma to move sluggishly or to stagnate. Fingering instabilities occur at low discharge rates and vary in timing (taking up to days to form) for eruptions of different compositions, based on the magma’s diffusional response time (Wylie et al., 1999). Focused flow (resulting in a single vent from many original vents) occurs at the lowest discharge rates, but does not necessarily imply that the source driving pressure is significantly reduced, meaning that eruptive activity along a fissure will localize to a main vent even if the magma pressure supplying the eruption is weak, but steady. Wylie et al. (1999) note the importance of including the temperature-dependence of magma viscosity. Stagnation of flow at the dike margins in response to cooling-induced viscosity increases provides a powerful mechanism for flow localization, via fingering instabilities, away from cooler zones. Viscosity-induced flow stagnation was found to be more significant than solidification for flow localization.

3.2.3 Syn-eruptive fissure transformations

During eruptions, the vents can become enlarged or constricted due to melting, flow cooling and viscosity increase, erosion, or collapse. These processes are a mixture of pure thermal, pure mechanical, and combined thermo-mechanical processes, which are briefly introduced here.

3.2.3.1 Thermal

Delaney and Pollard (1982) note that dike thickness does not affect the amount or rate of heat transferred to the wall rock during the eruption, and that thermal properties affect geometry through their influence on internal magma pressure distribution. They conclude that fissure eruptions will cool and solidify, within a day, when flow is laminar through a narrow dike. For Hawaiian eruptions to last longer than a day, localization to a wider central vent(s) is necessary. Bruce and Huppert (1989) investigated the melting of dike walls and freezing of magma onto the dike walls as a mechanism for flow focusing with a simplified thermodynamic model of basaltic fissures. Their model assumes the country rock is elastic, flow in the dike is laminar, that the country rock and dike magma (both basalt) have identical thermal properties, and that the wall rock is 50 degrees Celsius (˚C) cooler than the dike, but they do not account for the latent heat of fusion against the dike margin or thermal advection. They calculate the threshold temperature for which dike walls will eventually melt or solidify during an eruption. Assuming a country rock temperature (T) of T=100 ˚C far from the dike, it would take less than 1 d to solidify dikes having widths ≤30 cm, but it would take >18 days to solidify dike widths of 1.5 m. Furthermore, only fissures greater than or equal to (≥) 1.7 m in width would be able to melt their sidewalls and widen fissures during a prolonged eruption. Remelting of the initial quenched margin of the dike was termed “thermal turnaround” and must take place before the fissure wall rock can be thermally eroded (Bruce and Huppert, 1989).

Another study (Petcovic and Dufek, 2005) investigated the effect of employing a wall rock of lower solidus temperature than the intruding dike. For a simulation in which a 10 m wide basalt dike at its liquidus temperature of 1145 ˚C (solidus 1020 ˚

C) conductively heated tonalite wall rock initially at 50 ˚C, it took 30 d to initiate melting of the wall rock (solidus ~725 ˚C). The motion of the magma in the dike, however, was not explicitly treated. The dike temperature was held at 1145 ˚C throughout, and cooling of the magma in contact with the wall rock was not modeled. These simplifications mean that the time to initiation of melting was likely underestimated.

For the same compositions and geometry, simulations including advection of the magma, together with cooling-induced viscosity variations, showed that it takes much longer to initiate melting (320 d) when realistic temperature, viscosity, and velocity gradients are used. The cooling of the dike margins insulates the tonalite wall rock from the high internal temperatures of the dike (Petcovic and Dufek, 2005). A similar phenomenon was documented by Williams et al. (2004), where the chilled margin of a basalt lava tube insulated the host rock from erosion.

3.2.3.2 Mechanical

Delaney and Pollard (1981) documented field evidence of localization of dike flow in a "bud," or a wider area of the dike, produced by brecciation and removal of wall rock by plucking and transportation. This leads to large increases in flow rate and pressure applied to the conduit walls, creating a positive feedback where brecciation can continue to expand the conduit. Wylie et al. (1999) agree that vent localization could be induced mechanically, through brecciation and removal of wall rock by fluid pressure and fluid sheer stress. Removal of brecciated wall rock effectively widens the conduit, reducing flow resistance, and preferentially allows material entering the base of the fissure to laterally focus and exploit these pathways, leading to further mechanical erosion along those flow paths (Wylie et al., 1999).

Mitchell (2005) found that conduit sheer stresses in his model of basaltic fissures were not sufficiently high enough to promote fracturing and removal of large pieces of wall rock, and proposed that the most feasible mechanism for widening a basaltic fissure is likely through steady and continuous mechanical abrasion, rather than fracture-induced wall failure and removal.

3.2.3.3 Thermo-mechanical

In a study on the erosional capacity of surface lava flows, Fagents and Greeley (2001) note that to capture eruption dynamics accurately, the mathematics needs to combine rheological and thermal aspects of the system in the same equations, and not be addressed individually. In their computational fluid dynamic analysis, they inferred that melting of dense basalt (by molten basalt) near a vent would take only hours, whereas hundreds of meters to kilometers from source, melting could take up to two weeks to initiate. Fagents and Greeley (2001) emphasized that substrate heating penetration distance is controlled by the properties of the substrate itself. A low solidus temperature of the substrate relative to the lava can lead to enhanced erosion (Greeley and Hyde, 1972; Greeley et al., 1998), which could include any or all of the following: 1) mechanical removal or plucking of blocks (Peterson and Swanson, 1974), 2) gouging or scouring of the interface (Kauahikaua et al., 1998) between the dike and wall rock, 3) vigorous flow (Williams et al., 2004), or 4) actual thermal melting (Kauahikaua et al., 1998; Fagents and Greeley, 2001) after several days to weeks.

3.3 Field area and methods

3.3.1 The May 24–25, 1969 eruption (Mauna Ulu Ep 1)

An 18 hr long episode of fissure fountains on May 24, 1969 (Swanson et al., 1979) initiated the 5 yr long Mauna Ulu eruption of Kīlauea (Fig. 3.1, Tilling et al., 1987). The eruption took place on the upper ERZ of Kīlauea, where it crosses the periphery of the east-northeast (ENE) trending fractures of the Koʻae fault system. Five eruptions had occurred in the Mauna Ulu area between January1952 and May 1969. The 1969 fissure system crosses eruptive fissures from December 1965 and lies less than 100 m south of the December 1962 eruption location (Swanson et al., 1979). Activity on May 24–25, 1969 was the only episode in 1969 (of 12 total fountaining episodes) that was associated with a fissure source, and the western 880 m of the original fissure system produced the first historical eruption from the Koʻae fault system (Swanson et al., 1979).

The eruption began at 04:45 HST, preceded by a propagating earthquake swarm that woke local residents (Swanson et al., 1979). The fissure system opened rapidly, extending to 200 m north of ʻAlae pit crater in the east and cutting Chain of Craters Road 2.5 km to the west in 15 min (by 05:00 HST). The fissure system crossed ʻĀloʻi pit crater, which had been partially filled with 25 m of lava from the February 22, 1969 eruption. A significant amount of the February 22,1969 lava drained into the Mauna Ulu fissure system. By 08:30 HST, the fissure system reached its full extent, crossing ʻĀinahou Road (1 km west of Chain of Craters Road). During fissure opening, the whole length erupted low fountains ≤ 50 m in height, and the fissure evolved into two fountaining zones by 09:40 HST (Chapter 2): an EZ between ʻĀloʻi and ʻAlae craters, and a WZ (our field area) between ʻĀinahou and Chain of Craters Roads. The ~50 m high fountains showed small variations in height temporally and spatially in the few photographs available from May 24, 1969. The fissure was flooded to heights of 2–3 m above the current ground surface at peak discharge

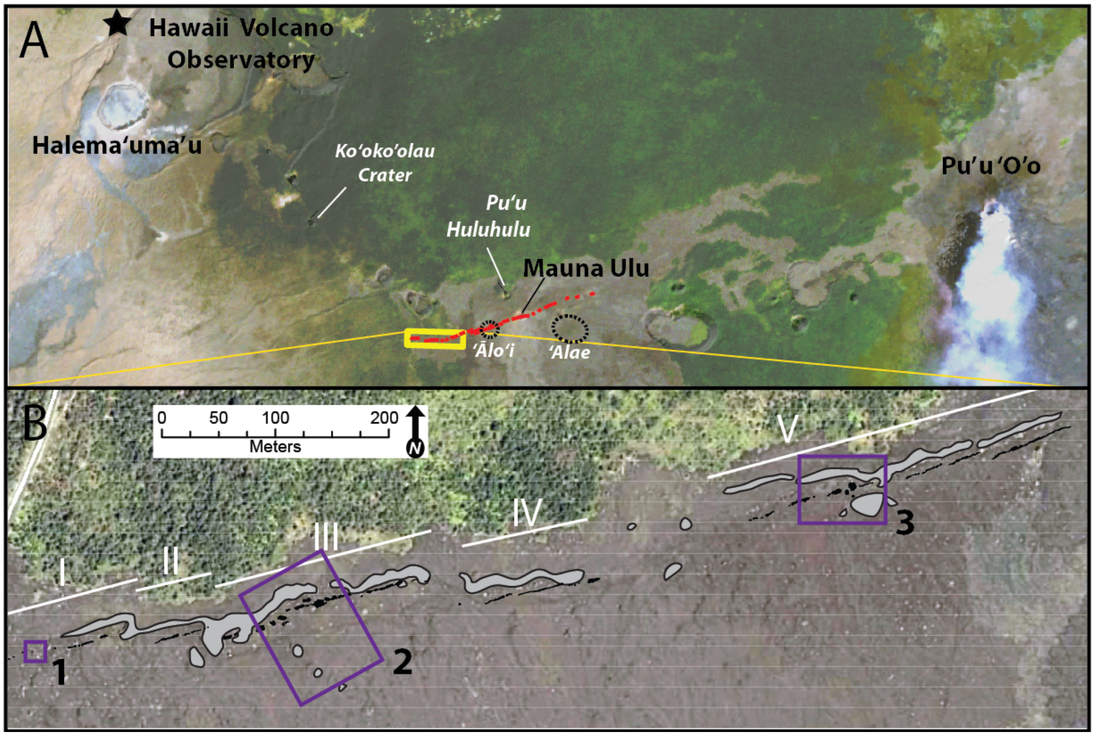

Figure 3.1 A Location map of Kīlauea and east rift zone. The original length of the May 24, 1969 Mauna Ulu fissure system is indicated in red, along with the outlines of ʻĀloʻi and ʻAlae pit craters that were buried during the eruption. **B** Present-day exposure of the fissure system, indicated by yellow box in a, is ~900 m long. The fissure system has five en echelon segments, labeled I – V. Spatter rampart trace is shown in dark gray, vents in light gray. Note that the vents at this scale are drawn in cartoon fashion to show relative locations and fissure (rectangles) versus circular (circles) geometries. The purple boxes designate where Fig. 3.5 (LiDAR 1), Fig. 3.6 (LiDAR 2), and Fig. 3.7 (LiDAR 3) are located from west to east, respectively.

(Chapter 2). Swanson et al. (1979) calculated that a total magma volume of 4×10^6 m^3 was erupted on May 24–25; no separate estimates were made for the EZ or WZ. Both fountaining zones produced lava flows that were impounded 1.2 km down-slope by a north-facing fault scarp in the Koʻae fault system (Swanson et al., 1979).

3.3.2 Measurements of vent/fissure geometry

The field study area measures 900 m long by 60 m wide on an 80º orientation and encompasses the fissure (Chapter 2), between the old Chain of Craters Road (now Mauna Ulu pullout) and the old ʻĀinahou Ranch Road (now the modern Chain of Craters Road). This area is the westernmost kilometer of an originally 4.5 km long system (Fig. 3.1a, red line), and is the western of the two loci of eruptive activity for the 1969 vents (the second was where the Mauna Ulu shield is now located) (Swanson et. al., 1979).

Vent dimensions (length and width) along the exposed fissure system were determined by using differential GPS and tape measurements. The fissure system consists of 5 segments, labeled I–V (Fig. 3.1b), and each segment contains several vents. Vents were numbered, starting with vent 1 in the west, and moving eastwards consecutively to vent 54. Lava is preserved west of vent 1, on the western side of the new Chain of Craters Road, but no source vents or ramparts are observed, therefore vent 1 serves as the point of origin from which distances are reported in the dissertation.

Vent geometry is defined as a combination of width, length, and depth (Figs. 3.2a, 3.2b): an aspect ratio in x-y space (map view) and a flaring ratio in y-z space (cross section), with x and y measured parallel and perpendicular, respectively, to the strike of the fissure and z denoting the depth coordinate. Aspect ratios (AR) were calculated by measuring the long and short axes of vents and dividing the short axis by the long axis. Flaring ratios (FR) were calculated by measuring the vent width at the inflection point between sloping (vent) walls and sub-vertical (conduit) walls and dividing by the vent width at the ground surface. The mean width of each linear vent was calculated from multiple measurements (Fig. 3.2c). AR and FR both have values ≤1. Vent orientation was also measured where the long axis was significantly greater than the short axis, as shown in Figure 3.2d.

Depth along the entire exposed fissure system was measured using a plumb bob. Depths may only be minima if the plumb bob landed on a ledge, overhang, or false roof, none of which can be distinguished from the “bottom” of the fissure system cavity when standing on the ground surface.

3.3.3 Light detection and ranging measurements

Three locations (Fig. 3.1b), encompassing a range of vent shapes, were chosen to image with a tripod-mounted light detection and ranging (LiDAR) device (as described in Morris et al., 2008) in order to quantify the subterranean geometry and identify any distinct geometric change between the vent and the shallow conduit. In all 22 LiDAR scans, image resolution was set to 4 cm at a distance of 30 m to image the ramparts, and 1 cm at 10 m to image the vents and conduits. The first LiDAR area used one scan to image a small ellipsoidal vent. The second LiDAR area combined nine scans to image the widest linear

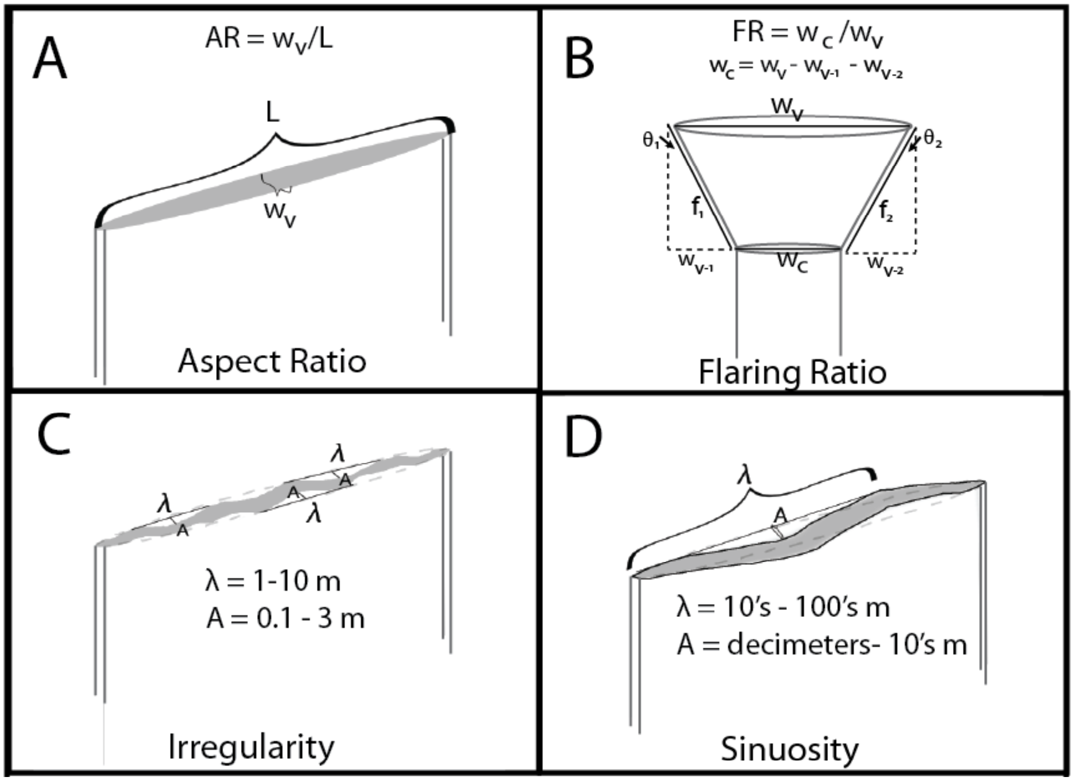

Figure 3.2 Measurements and parameters discussed throughout the paper. **A** Aspect ratio (vent width divided by vent length) is the surface area geometry of the vent. **B** Flaring ratio (calculated conduit width divided by measured vent width). Both measurements are taken in the same vertical plane. Conduit width is calculated by using trigonometry. Measuring the length the flared walls and the angle of the flare allows the calculation of the horizontal width that the flared wall moved inward, and subtracting that value from the vent width (from both sides of the fissure) yields the conduit width. **C** **I**rregularities in vent width, which we have defined as fluctuations in vent width *without a change in vent strike*. This can visually appear to be small-scale sinuosity (Fig. 3.2d), but measurement of the waveforms from trough to trough, as depicted on the diagram, will show that the waveforms are all oriented along the same strike. The range of wavelengths is from 1 to 10 m, and corresponding amplitudes of 0.1 to 3 m. **D** Sinuosity in vent geometry, which we have defined as a change in vent strike *without a change in vent width.* The line of strike is indicated by a dashed gray line. The wavelengths of sinuosity are several tens to hundreds of meters with corresponding amplitudes of 0.1 to 10 m, respectively.

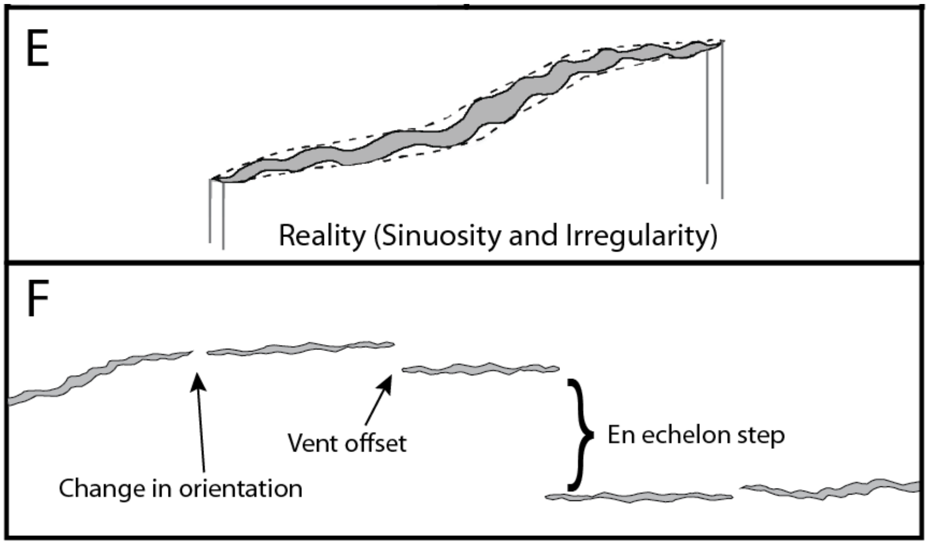

Figure 3.2 continued **E** Complexity of a vent observed in the field. Irregularities are the most common perturbation of geometry from an ideal circle, ellipse, or linear fissure, but they are superimposed on sinuosity when sinuosity is present. Sinuosity is typically difficult to discern because the wavelengths are large and the amplitudes are small, making the waveform subtle. **F** Complexity of sequential vent geometries observed in the field. Vents can be in line with each other (lower right) or offset from each other within each segment (upper left).

vent in the field area (allowing for the deepest view into the fissure), together with the associated northern ramparts, and three isolated southern areas of spatter. The third LiDAR area combined 12 scans to image a flared circular vent overlying a fissure conduit, together with the associated northern and southern ramparts, and some mounds of tree molds north of the rampart.

3.4 Results

3.4.1 Pre- and post-eruption topography

Digitized ground elevation derived from a 1965 topographic map, with the addition of lava flows from eruptions between 1965 and 1969, and fault scarps from 1965 aerial photographs (Chapter 2) provide a baseline map to identify the topographic features with which the fissure system interacted as it broke the surface. The pre-eruptive ground surface, sloping gently to the southeast, has shallow, seemingly inconsequential ‘valleys’ and ‘ridges’ oriented downslope of the fissure (which helped to funnel lava downslope during eruption; Chapter 2) and a local topographic high, elevated 3 m above the fissure, directly north of segment III. The elevation of the fissure is approximately constant, with no more than 6 m of vertical relief along its length; the lowest point along the fissure is between segments IV and V, while the high point is at segment II.

The fissure is aligned with Koʻae faults that also trend at 80º, and Swanson et al. (1979) noted that the westernmost vents (i.e., those west of our vent 1) were located along a north-facing Koʻae fault scarp. The WZ fissure spans and connects two visible fault scarps seen on the 1965 aerial photographs. It is not clear from the aerial photographs whether there was a fault trace connecting the two scarps prior to the eruption.

Lava flow thickness at vent is 0.5–3 m, found by subtracting the digitized pre-eruption topographic map from the current digital elevation model (Chapter 2). The vertical transition from flared vents to steep-walled conduit occasionally coincides with the base of the 1969 lava, but there are several instances (i.e., LiDAR area 3–see section 3.3.2) where this is not true, and vent flare extends well below the estimated thickness of 1969 lava. In these vents, a surface veneer of juvenile lava that has spalled off the vent wall to reveal prehistoric lavas is evidence that flare cuts into wall rock.

3.4.2 Fissure system orientation, dimension, and segmentation

The Mauna Ulu fissure strikes 80º along the ERZ at 1000 m elevation above sea level. The fissure system is exposed for 470 m over a linear span of 880 m and was divided into five segments. Eyewitness observations and photographs indicate that linear vents contained multiple fountains during Ep 1.

The five segments are defined as alignments of closely spaced vents separated by four vent-free regions, at 82 m, 150 m, 336 m, and 475 m, respectively, from vent 1. Segments define an en echelon pattern; three vent-free regions are marked by meter-scale right-stepping en echelon features, and one by a meter-scale left-stepping feature, whose orientations are summarized in Table 3.1. Segment architecture is complex; segments differ in the type, number, and relative positioning of vents.

Segment I (Fig. 3.3) (vents 1–8) contains two lateral vent displacements. Vents include three circular geometries and five fissure geometries. Segment II (vents 9–14) also has two minor shifts in fissure alignment. Vents 9–14 all display linear geometries. Segment III (vents 15–33) six fissure alignment displacements. Segment III consists of two circular vents, 14 linear vents, and three flared circular vents. A cluster of six of these vents (vents 18–23, Fig. 3.3) form two closely spaced and parallel alignments and consists of one circular vent, two flared circular vents, and three linear vents. Segment IV (vents 34–40) has four vent displacements. Vents 34–40 contain one circular vent and six linear geometries. Segment V (vents 41–54) has four separate alignments of linear vents and one cluster containing five closely spaced vents that do not lie along a single trend. Vents 41–54 comprise a series of nine linear geometries and five flared-circular geometries that make up the vent cluster. In summary, individual fissure segments contain between 6 and 19 vents; all have some linear vents, but some also contain circular vents, flared linear vents, and or flared circular vents. In two instances, vents are clustered in groups instead of being aligned along the fissure strike.

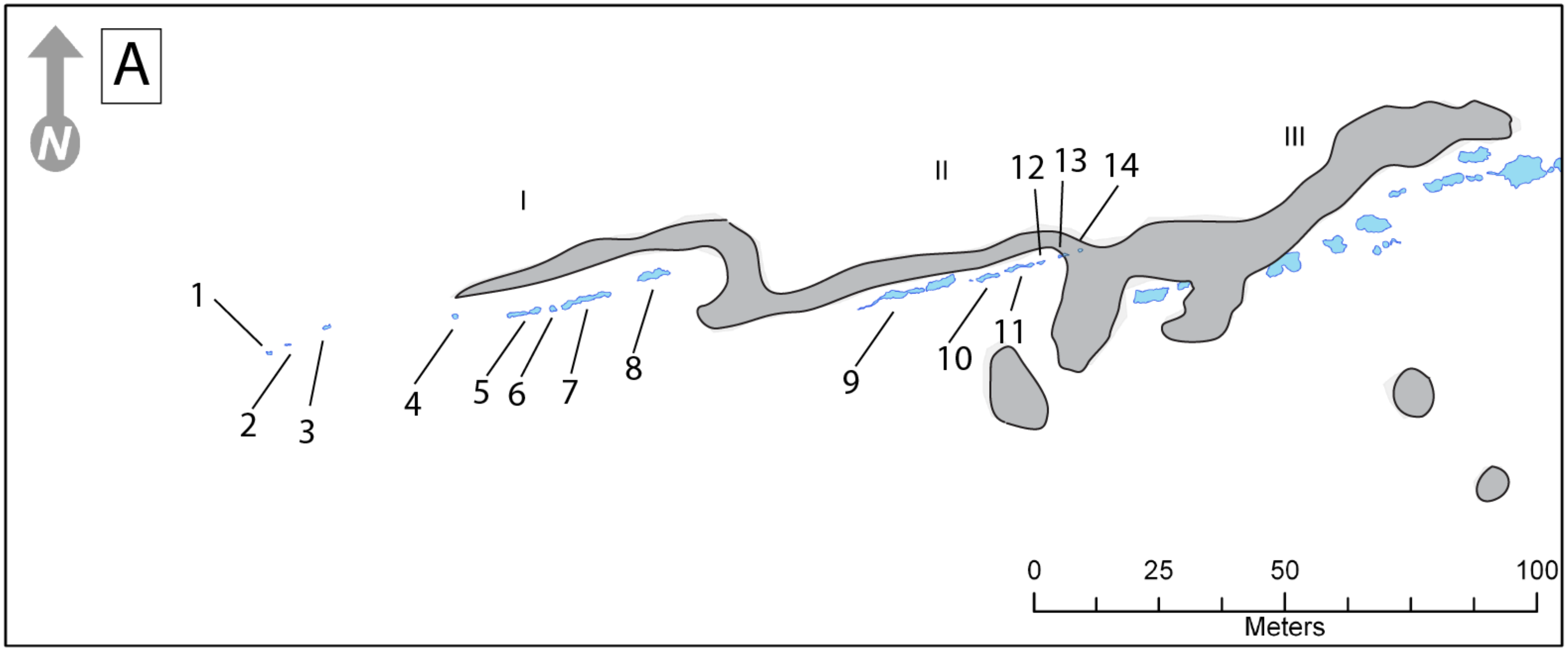

Figure 3.3 Kinematic GPS trace of 54 vents, showing their position, geometry, and size. The rampart footprint is in light gray for spatial correlation with Figure 1a. **A** Vents 1–14 on fissure segments I and II.

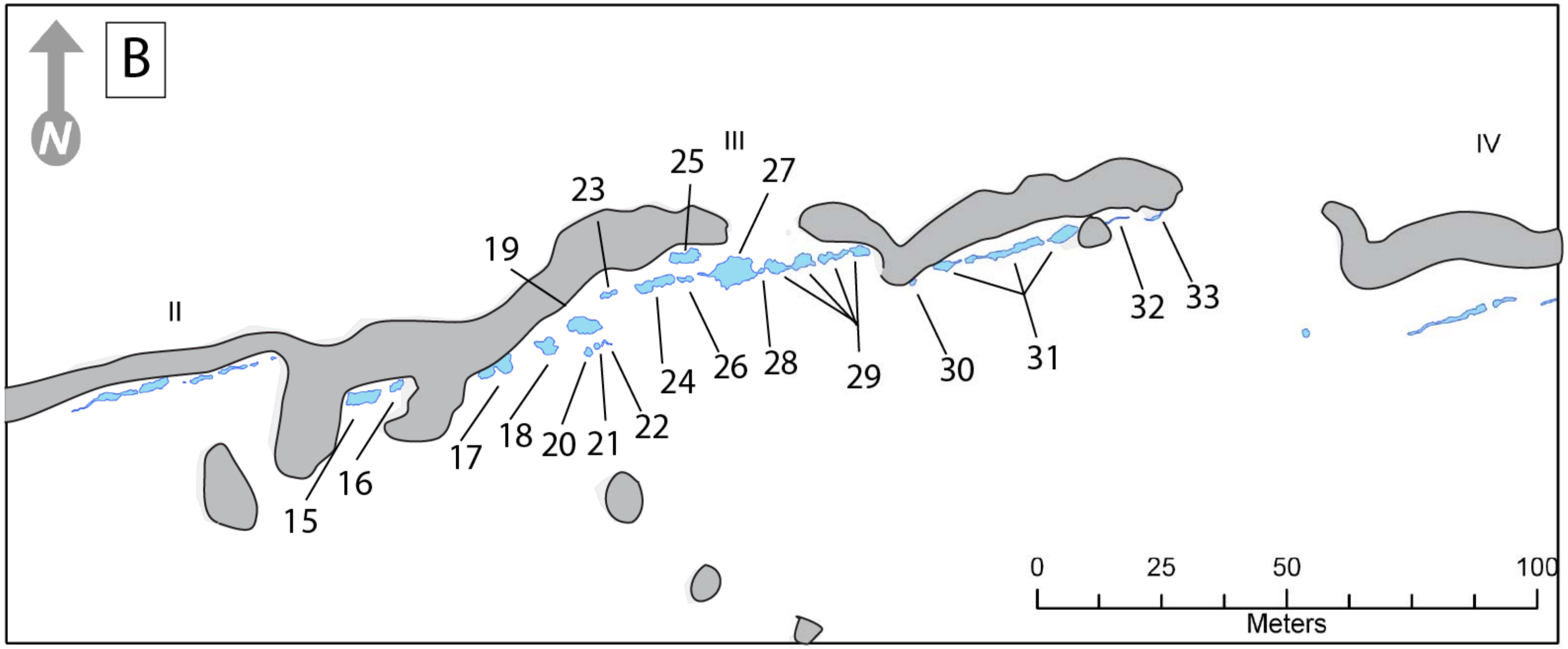

Figure 3.3 continued B Vents 15–33 on fissure segment III.

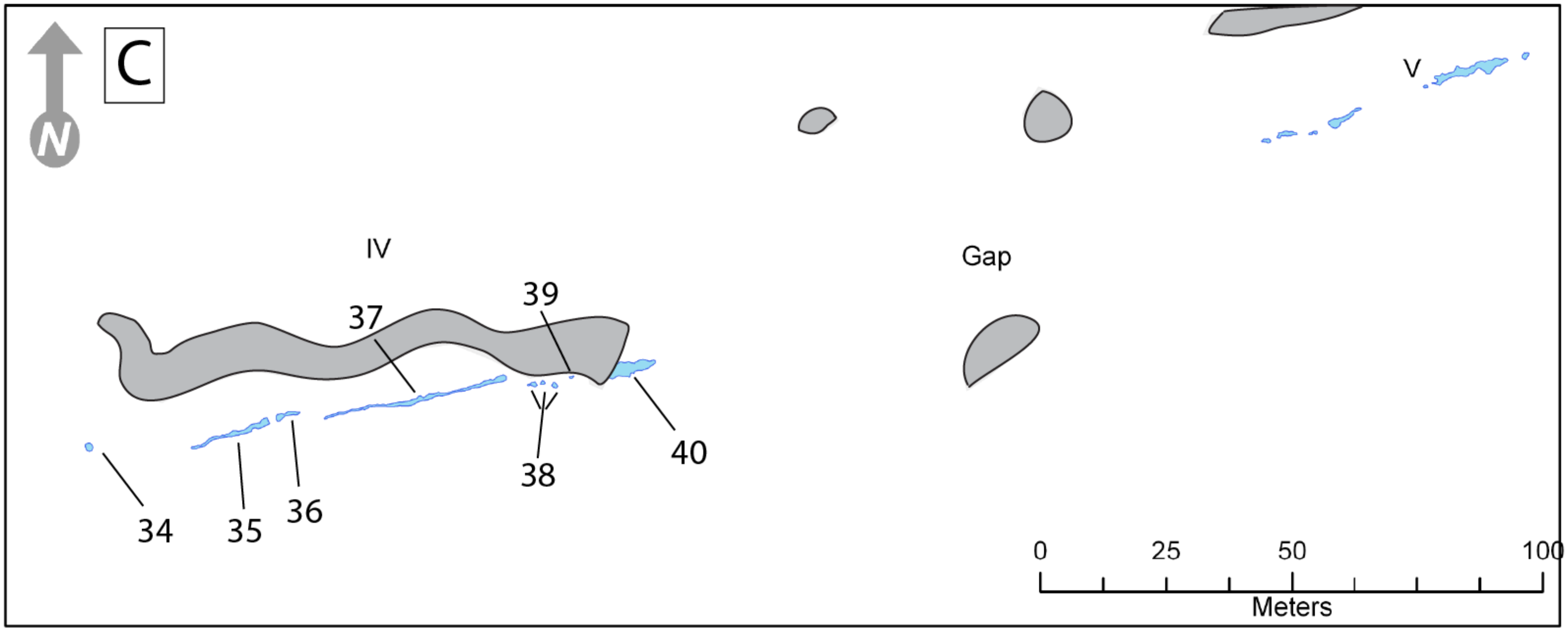

Figure 3.3 continued C Vents 34–40 on fissure segment IV and rampart/vent gap.

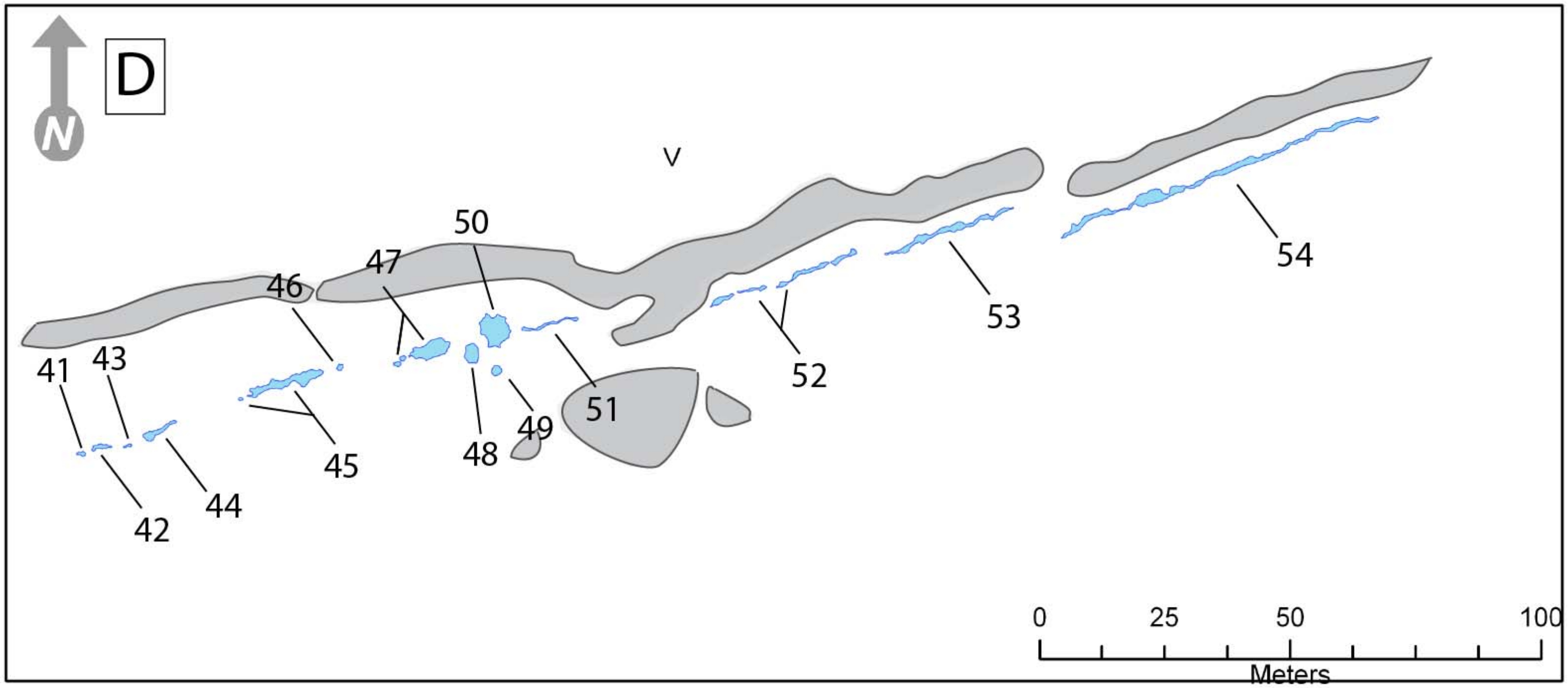

Figure **3.3 continued D** Vents 41–54 on fissure segment V.

On the May 24, 1969 aerial photographs from 9:40 am HST, four gas and ash plumes emanate from linear vents immediately east of the old Chain of Craters Road. There is fresh lava in the photograph, but there is no incandescent material to indicate ongoing fountaining of these four vents at the time of the photograph. These en echelon linear vents, if preserved today, would constitute an additional Segment VI, but are buried by the 1971 pāhoehoe and 1974 ʻaʻā lava flows. Only the crest of one spatter rampart remains visible.

3.4.3 Vent geometries: sinuosity, irregularity, and roughness

None of the vents are well approximated by simple geometric shapes (i.e., a rectangle [linear vent] or ellipse [circular vent]). All vents show centimeter-scale relief along the vent walls, which I refer to as roughness. Linear (elongate) vents also display meter-scale irregularity and decameter-scale sinuosity. Vent irregularity (Fig. 3.2c) takes the form of pinching and swelling of the fissure, causes a deviation in vent width along the fissure length from an idealized geometry (Fig. 3.2b). Irregularity was characterized by measuring variations in vent width. I define vent sinuosity (Fig. 3.2d) as a longer wavelength deviation of vent geometry from a straight line, unrelated to variation in vent width, giving a curved or wavy appearance. Sinuosity was characterized by measuring trough-to-trough wavelength orientations and amplitudes in the geographic information systems program ArcGIS.

Sinuosity occurs over wavelengths of tens to rarely hundreds of meters. The longer of these waveforms can extend over numerous vents (e.g., vents within fissure segments III and IV). Shorter waveforms are confined to a single linear vent, specifically vents 29, 35, 37, 52, 53 and 54. Only four multi-vent waveforms can be identified and are found within segments III and IV. Wavelengths for these four waveforms are 78 m, 168 m, 206 m, and 454 m. Trough-to-peak amplitudes of these four waveforms are 11 m, 12 m, 21 m, and 39 m respectively. The six vents displaying internal sinuosity are the six longest linear vents in the field area and are apparently long enough to incorporate the nature of the waveform, whereas other vents are too short. Measurements from vents 29, 35, 37, 52, 53, and 54 show a typical wavelength of 11m (± 6 m) and amplitude of 63 cm (± 27 cm). This sinuosity and any associated irregularity also extend vertically over the entire depth range that is visible within the fissure.

Irregularity of the fissure (Fig. 3.2c) occurs on meter scales, and is different on the north and south walls of the fissure. The north wall irregularities can be characterized by a spacing of 3 m (±1.2 m) and an amplitude of 80 cm (± 60 cm), oriented along an average strike of 77º. Irregularities on the south wall of the fissure are more variable, with an average spacing of 4 (± 2) m and an amplitude of 70 cm (± 40 cm), oriented along an average strike of 72º. Fissure walls only touch each other when two large irregularities are aligned in a narrow fissure. Amplitude of the irregularities affects vent width more significantly than vent orientation. Although the irregularities on each side of the fissure have different spacings and rarely match on a one-to-one correlation, they are spaced within the stated standard deviations of each other. Irregularity is visually seen to continue with depth into the fissure and, while not measured for safety reasons, appears similar to the irregularity measured at the vent surface.

Drain-back of lava into the vents produced a smaller scale undulation on the fissure walls, over the entire length of the fissure. There are two mean spacings measured at this scale: 1) trough-to-trough spacing of 65 (± 10) cm with an amplitude of 30 (± 5) cm, and 2) 1.5 m (± 25 cm) trough-to-trough spacing with 65 (± 10) cm amplitude. As with irregularity and intra-vent sinuosity, the drain-back texture continues with depth into the fissure, but in contrast, it does not always extend to the lowest depths visible (Chapter 2).

3.4.4 Vent shapes: distribution, dimensions, end-member types

There are two typical plan-form geometries, circular vents and linear vents, both of which may have either a flared or a non-flared vertical profile. Figure 3.4 plots the aspect ratio versus flaring ratio, where the left side of the graph corresponds to linear sources and the right side of the graph corresponds to circular sources; the top of the graph corresponds to non-flared vents and the bottom of the graph corresponds to flared vents. The aspect ratio division between circular and linear sources taken to be AR = 0.5, where the vent length is twice the vent width. Smaller aspect ratios correspond with more elongate surface geometries. The division between flared and non-flared sources is taken to be FR = 0.7, where the vent width is ≥50% wider than the conduit width, because it will be larger than the scale of irregularities, and therefore the documented flaring is genuine as opposed to an artifact of the irregularities. All vents show some degree of flaring and flaring ratios vary continuously, with the exception of nearly circular vents. Linear vents predominate and circular vents, where present, are typically found at the ends of a segment. Flared circular vents are the least common form. Non-flared circular vent/shallow conduit geometries are conceptually analogous to a vertical pipe. Linear vents are equally common in flared and non-flared forms. Non-flared linear vent/conduit geometries are conceptually similar to a knife blade or polyhedron, where the longest axis extends into the ground, and the median and short axes dimensions visible at the ground surface yield an aspect ratio less than (<) 0.5.

Several trends are apparent on the plot of vent geometry (Fig. 3.4). On the far right side of the plot, six vertically aligned data points at AR = 0.93 show an increasing vent flare of nearly circular point sources. Vents 04, 20, 21, 34, 48, and 49 plot in this category and are typically 1.3 m (± 0.2 m) long by 1 m (± 0.3 m) wide, with the largest vent measuring 1.5 m x 1.4 m. I identify these data points as indicating a field of circular vents in Fig. 3.4, distinct from all other vents in the field area. A similar trend, albeit slightly less well correlated, is shown in the increase in flaring among linear vents on the left side of the plot, indicated by the vertical alignment of data points between AR = 0.00 and 0.12. Twenty vents plot in this category and are typically 18 (± 15) m long by 0.8 (± 0.4) m wide, with the most extreme case being vent 54 lying outside the standard deviation at 67.5 m long and 1 m mean width. I identify these 20 data points as indicating in

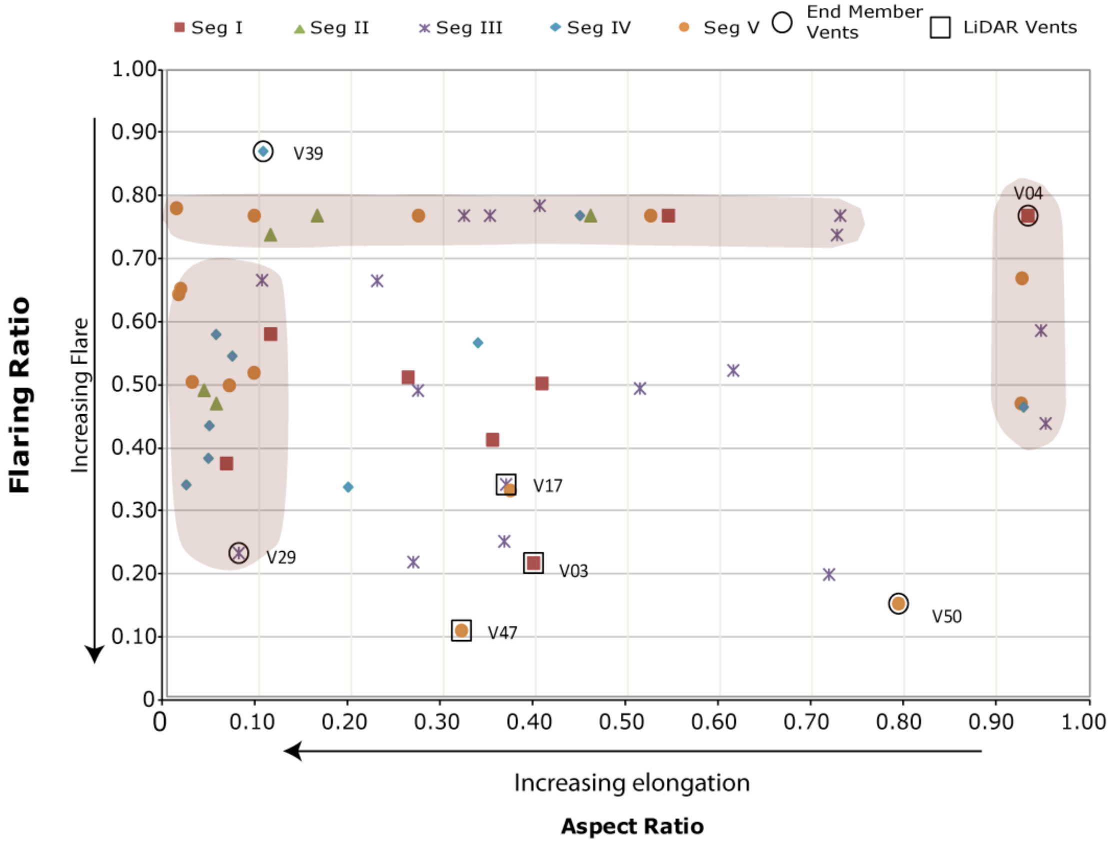

Figure 3.4 Plot of aspect ratio (vent width divided by vent length) versus flaring ratio (calculated conduit width divided by measured vent width). Symbols represent fissure segments: segment I = red squares, segment II = green triangles, segment III = purple asterisks, segment IV = blue diamonds, and segment V = orange circles. End member type vents discussed. Vent 4 represents the most circular vent in the field area with the least flaring (for circular vents). Vent 39 represents the most linear fissure vent with the least amount of flaring (compared with other linear vents). Vent 29 is the linear fissure vent with the most flaring. Vent 50 is the most circular of highly flared vents. Vent 47 (Fig. 3.7) is the vent with the most flaring in the entire field area. Vent 17 (Fig. 3.6) has the clearest and widest view with depth of any vent in the field area, especially those of fissure geometry.

Fig. 3.4 a field of flared-linear vents distinct from other vents in the field area.

Along an FR value of approximately 0.77, 15 vents define a continuous progression from non-flared circular source to non-flared linear source. This non-flaring field plots distinctly from other vents in the field area on Fig. 3.4. The remaining 17 vents plot in a wide field between AR = 0.2–0.8 and FR = 0.1–0.67. These vents are visibly more complex than other vents in the field area. In some cases, such as vent 47 (LiDAR area 3) and vent 50, there is a combination of characteristics, where a dramatically flared circular vent is superimposed upon an unflared fissure conduit. Segments III and V, the two longest segments, have vents that plot in every field of Figure 3.4. Segment I contains three of the four vent types, missing only flared circular vents. Of the two shortest segments, segment II resides almost exclusively in the non-flared linear vent field while segment IV, with the exception of one vent, straddles the flared and non-flared linear vent fields. It is important to note that along linear vents, photographic evidence (Swanson et al., 1979; Chapter 2) indicates that multiple fountain sources were associated with different individual vents.

3.4.5 Vent geometries

Trigonometry was used to calculate the flaring ratio (Fig. 3.2f). The two inclined edges were measured for inclination and length to the change in wall angle of the vent/upper conduit system and then the horizontal extent corresponding to that length was calculated using:

$$w_C = w_V - (f_N \cos\theta) - (f_S \cos\theta)$$

where w_c is the conduit width, w_v is the flared vent width, f_N is the length of northern vent wall, θ_N is the angle of the northern vent wall, f_S is the length of northern flared vent wall, and θ_s is the angle of the southern vent wall. Each of the horizontal extents due to flaring was subtracted from the flared surface vent width to calculate the conduit width. Transition points could not be documented everywhere due to the unsafe nature of several vents and the lack of an obvious transition point in other vents. However, most of the measured flaring ratios had a slope inflection point less than 2 m down the inclined plane and could be measured with a simple board-and-Brunton apparatus. Although the flaring ratio and aspect ratio allow quantification of a vent in two planes, care must be taken when calculating the flaring ratio, especially when the part of the system that is flared lies within the 1969 lava where slumping of the hot vent walls may have altered the flaring angle. Despite this caveat, our vent geometry plot (Fig. 3.4) shows the expected trends of non-flaring to flaring circular and linear sources, as well as a transition from non-flared circular source to non-flared linear source. The vents that plot in the middle uncorrelated region are those that show a combination of features, such as the flared circular vents 47 and 50 over the fissure conduit.

3.4.6 Shallow conduit geometries and vent depths

LiDAR data at 1 cm resolution were collected for three representative vents, documenting the finer detail of the vent and shallow subsurface geometry. Tripod-mounted scans centered at 34 m (vent 3), 243 m (vent 17), and 689 m (vent 47) document the shallow conduit and conduit-to-vent transition for a circular source, linear source, and flared circular source geometry respectively. Within the LiDAR data, cross-sections were positioned to cut the fissure in two manners: 1) parallel to the ground surface at one meter depth intervals and 2) perpendicular to the strike of the vent to show the true width. Where depth and cross-sectional contours intersect the data point cloud, a width measurement was calculated, creating a 1m x 1 m grid of measurements within the shallow conduit.

Our LiDAR area 1 data (vent 03, Table 3.1, Fig. 3.5) extended 4.5 m down into the circular vent, but the data become too sparse for analysis below 3.5 m depth. No vertical cross-sections were made for this point cloud, but four horizontal cross sections could be measured. Across the fissure, the vent width narrows abruptly from the northern side, whereas the deeper conduit pinches more gradually (Fig. 3.5c). Viewed in the plane of the fissure, the apparent vent length changes more gradually with depth because it is a function of the LiDAR field of view (Fig. 3.5b). This has the effect of falsely increasing the aspect ratio trending towards A.R. = 1 with depth, and making the delineation of vent to conduit transition more difficult. The vent and shallow conduit dip 85º to the south and appear to plunge 80º to the east along the line of the fissure, but the plunge reflects the LiDAR viewing angle into the vent for maximum depth penetration. The orientation of the LiDAR allowed for widths to be measured to a depth of 1.68 m, below which irregularities cause data gaps. These measurements are not all oriented in the same direction, due to the narrow

Table 3.1 Fissure widths derived from LiDAR point cloud data for vent 3/LiDAR area 1 (Figs. 5b, 5c). Measurements of the maximum width were taken at four depth intervals, as vent 3 was our "type vent" for the circular geometry.

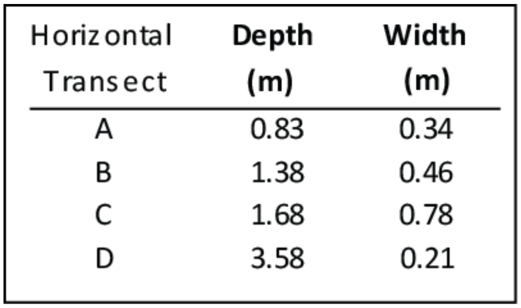

Horizontal Transect	**Depth (m)**	**Width (m)**
A	0.83	0.34
B	1.38	0.46
C	1.68	0.78
D	3.58	0.21

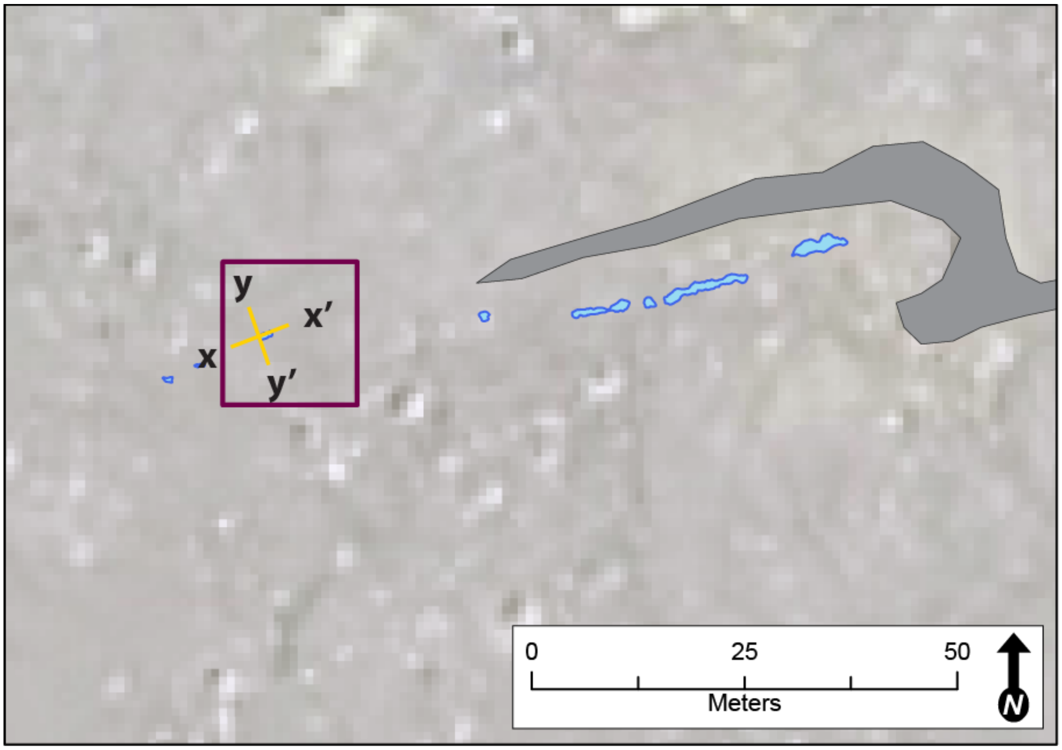

Figure 3.5 A Map showing segments I and II, location of LiDAR area 1 is marked with the purple box. Yellow lines indicate cross sections x-x' in Fig. 3.5b and y-y' in Fig. 3.5c

.

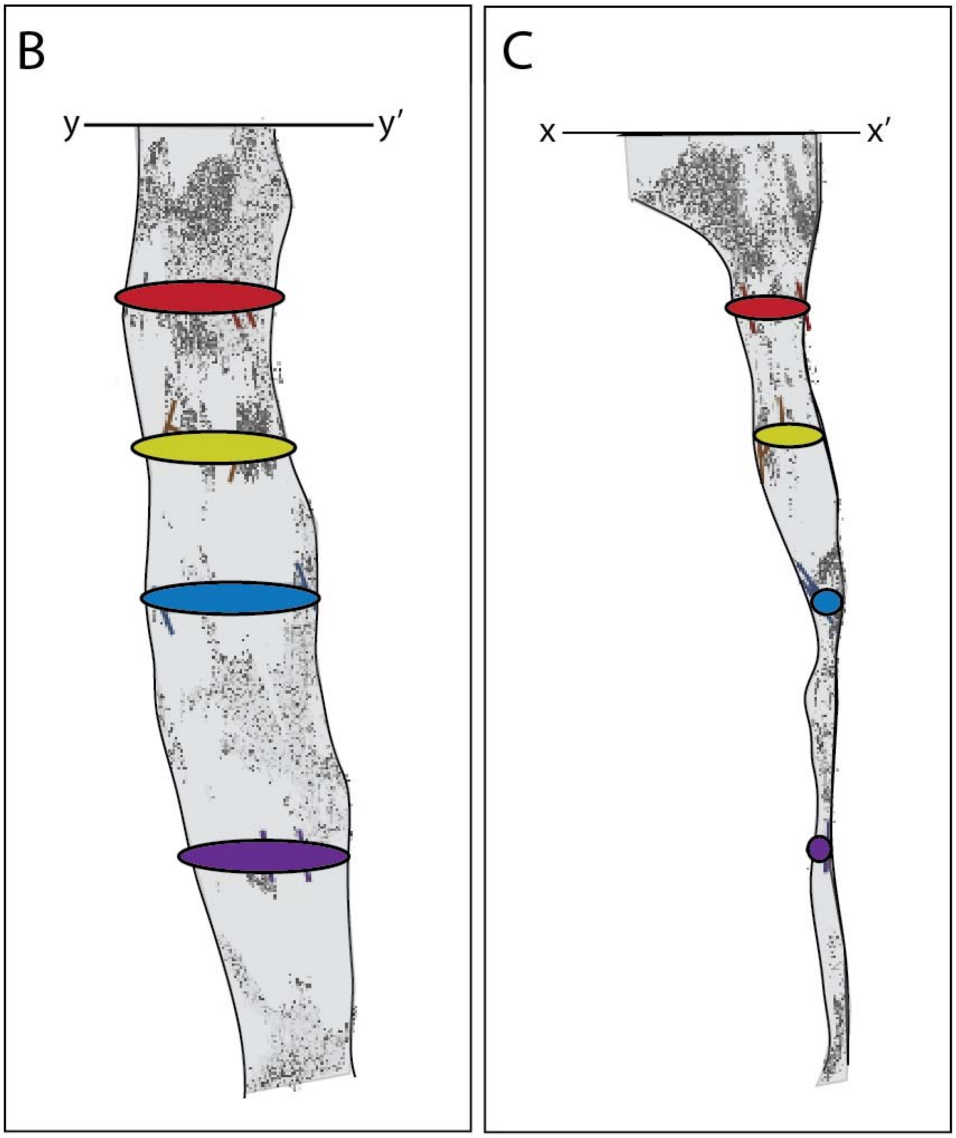

Figure 3.5 continued **B** View of LiDAR point cloud perpendicular to vent/conduit strike. View is to the north-northwest. Black lines denote boundaries of the LiDAR cloud. Colored ellipses indicate locations of vent width and length measurements. **C** View of LiDAR point cloud along strike. View angle is to the east.

.

nature of the sub-circular vent and shallow conduit. The transition from the conduit to vent is at 1.68 m depth (blue), where the fissure widens sharply. A second break in slope at 0.8 m depth (red) represents flaring of the fissure.

Our LiDAR area 2 data (vent 17, Table 3.2, Fig. 3.6) imaged the fissure to 16 m depth below the surface and yielded width measurements to 13 m deep in the conduit. At the ground surface, vent width is 2.4 (± 1) m, and narrows gradually until it is 1.2 (± 0.4) m at 12 m depth. Measurements could not be made below 13 m depth due to progressively larger gaps in the data. The vent and shallow conduit system in the plane of the fissure dip 72º to the north. Viewing angles of the LiDAR cause the system to appear to plunge 53º to the west along the fissure strike. The transition from shallow conduit to vent is at 3 m depth.

Our LiDAR area 3 data (vent 47, Table 3.3, Fig. 3.7) recorded a flared vent and fissure conduit combination to a vertical depth of 11 m below the surface. In the first 4 m, the vent is wide, with a mean width of 2.9 (± 1.3) m. Widths dramatically decrease beyond 4 m below the ground surface, narrowing to 0.8 (± 0.7) m. Below this depth, while parts of the system were imaged, there was no depth where data were recovered on both walls to allow width to be calculated. The transition from shallow conduit to vent is at 4 m depth, where the upper 4 m comprises the flared vent and the lower 7 m represents shallow conduit (Fig. 3.7). Of the sparse data returned from the lower 7 m, the fissure dips 84º north and appears to plunge 53º to the east, but the plunge may be a result of the viewing angle into the linear vent, similar to LiDAR areas 1 and 2.

Table 3.2 Fissure widths and lengths derived from LiDAR point cloud data for vent 17/LiDAR area 2 (Figs. 3.6b, 3.6c). This vent was our “type vent” for the fissure geometry. The point cloud extended to 16 m vertical depth, but gaps in the data (i.e. shadows in the point cloud) preclude width measurements below 13 m depth. Each horizontal transect, labeled A–N, intersects the point cloud at 1 m increments descending into the fissure and has multiple width measurements along its length. The mean of those measurements is listed in the table, along with the standard deviation from the mean. Linear distance covered is the length visible in the data point cloud, but as discussed in the text, is affected by the viewing angle of the LiDAR. Linear distance covered is a proxy for the number of width measurements (actual number shown in Figs. 3.6b, 3.6c), as they were spaced 1 m apart horizontally as well as vertically. Transects M and N did not have enough width measurements to calculate a standard deviation. .

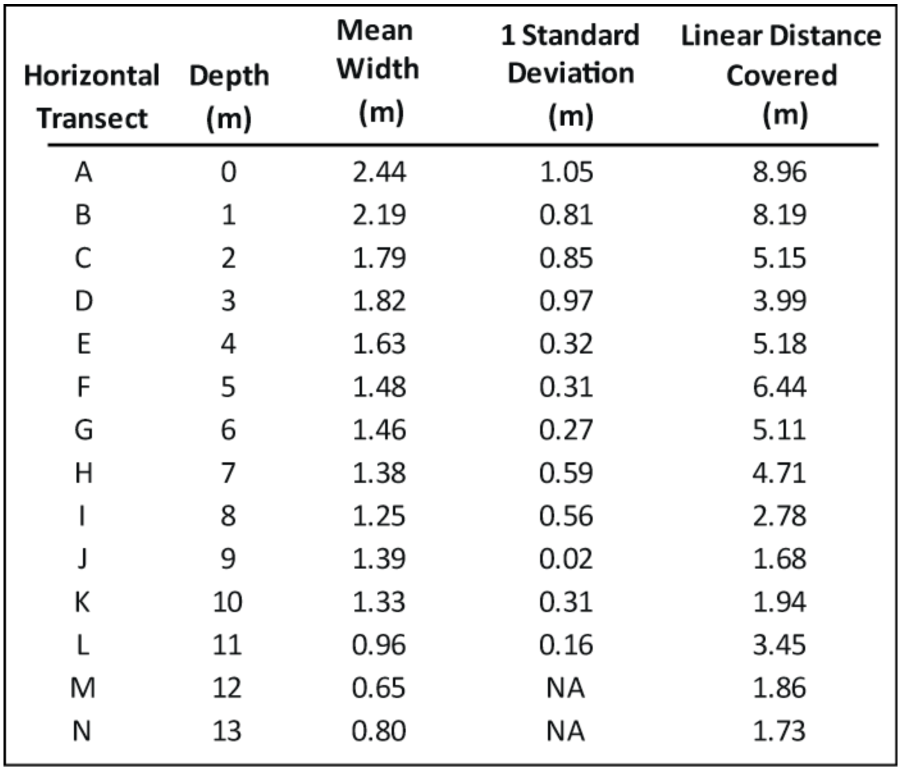

Horizontal Transect	Depth (m)	Mean Width (m)	1 Standard Deviation (m)	Linear Distance Covered (m)
A	0	2.44	1.05	8.96
B	1	2.19	0.81	8.19
C	2	1.79	0.85	5.15
D	3	1.82	0.97	3.99
E	4	1.63	0.32	5.18
F	5	1.48	0.31	6.44
G	6	1.46	0.27	5.11
H	7	1.38	0.59	4.71
I	8	1.25	0.56	2.78
J	9	1.39	0.02	1.68
K	10	1.33	0.31	1.94
L	11	0.96	0.16	3.45
M	12	0.65	NA	1.86
N	13	0.80	NA	1.73

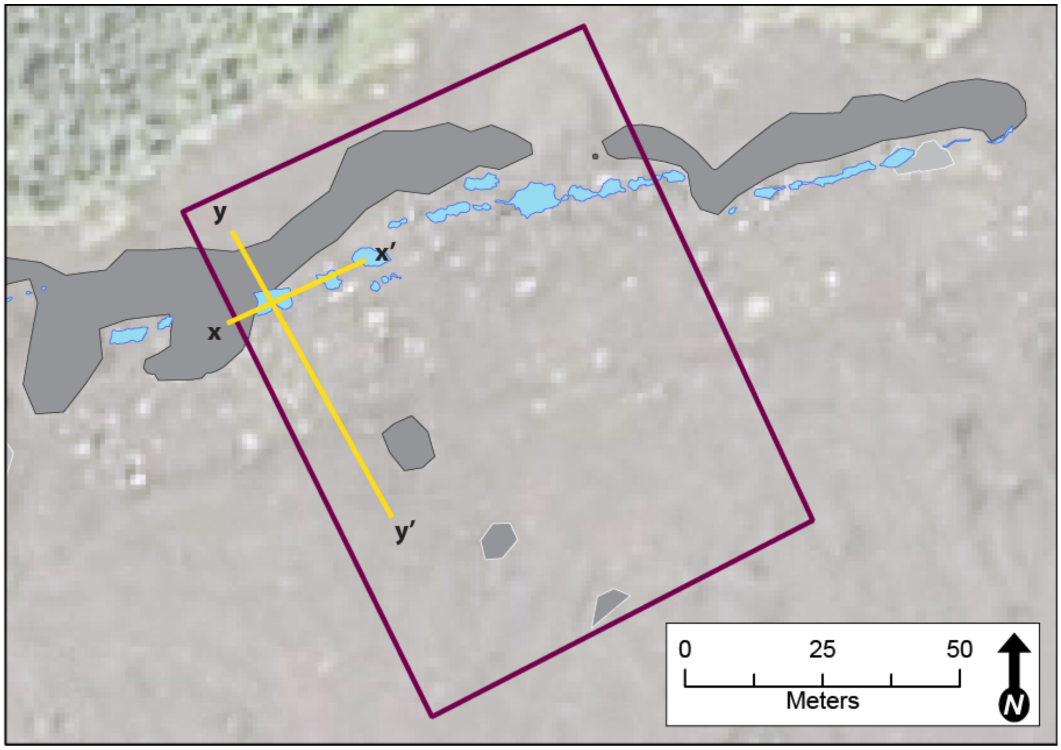

Figure 3.6 A Map showing all of segment III, location of LiDAR area 2 is marked with the purple box. Yellow lines indicate cross sections x-x' in Fig. 3.6b and y-y' in Fig. 3.6c.

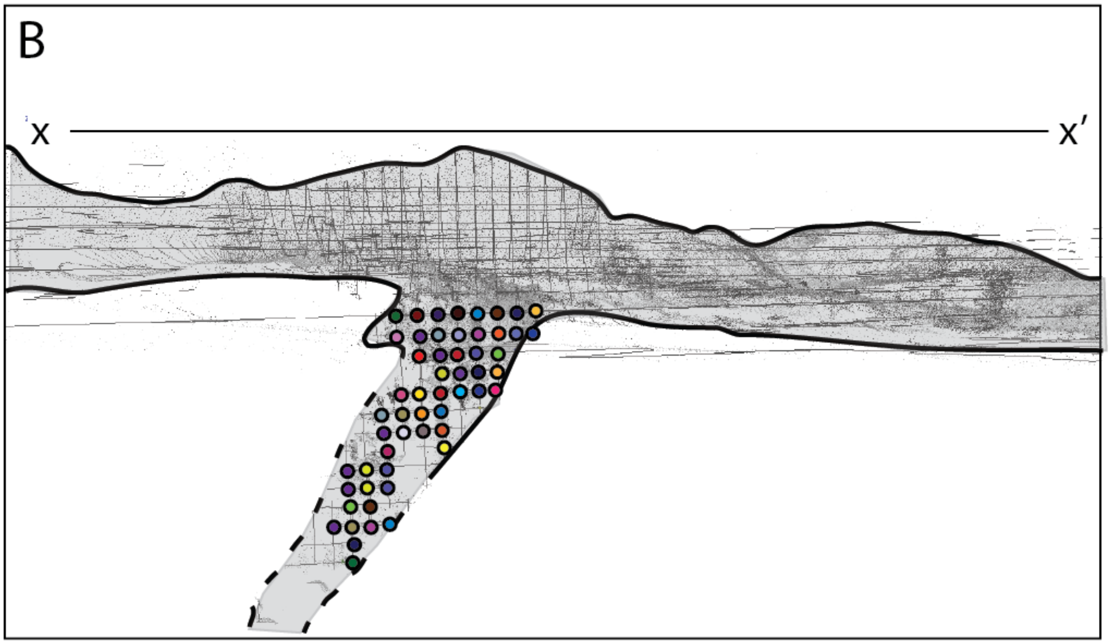

Figure 3.6 continued B View of LiDAR point cloud perpendicular to vent/conduit strike. View angle is to the northwest. Black line is dashed where the fissure wall is projected to be, but LiDAR data is scarce or has too many holes to know with certainty. Colored circles at grid point intersections indicate locations of vent width measurements.

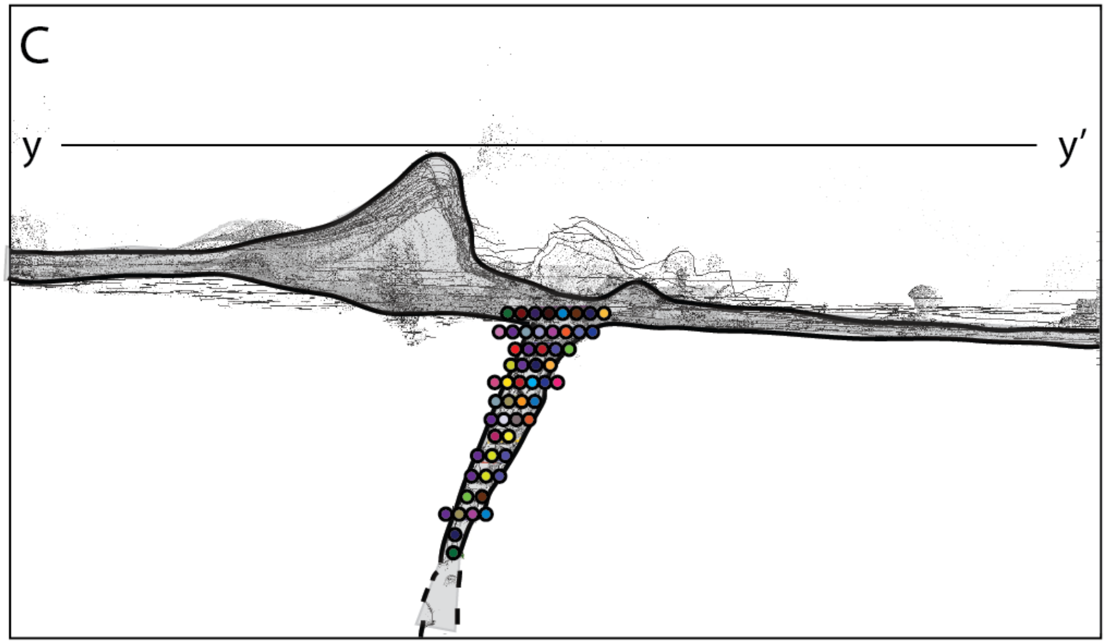

Figure 3.6 continued C View of LiDAR point cloud along strike to the east. Black lines denote ground surface in the closest parts of the LiDAR cloud, but ramparts can be seen above this line and are located east of the vent. Colored circles extending across the vent/conduit correspond to the depths of width measurements, and correlate to the same colors/measurements in Fig. 3.6b.

Table 3.3 Fissure widths and lengths derived from LiDAR point cloud data for vent 47/LiDAR area 3 (Figure 7b, 7c). This vent was our “type vent” for a general flared geometry, and is a flared sub-circular vent superposed on an unflared linear conduit. The point cloud extended into the shallow conduit to 12 m vertical depth, but data gaps in the data (i.e. shadows in the point cloud) preclude width measurements below 4 m depth. Each horizontal transect, labeled A – N, intersects the point cloud at 1 m increments descending into the fissure and has multiple width measurements along its length. The mean of those measurements is listed in the table, along with the standard deviation from the mean. Linear distance covered is the transect length visible in the data point cloud, and is a proxy for the number of measurements (actual number depicted in Figs. 3.7b, 3.7c). As discussed in the text, the viewing angle of the LiDAR provided a means of quantifying the conduit’s upper most exposure, but no part of the shallow conduit below 4 m depth has data on both fissure walls in any given location to allow width measurements in the point cloud (transects F – N). Width measurements in the vent region were spaced 1 m apart horizontally as well as vertically

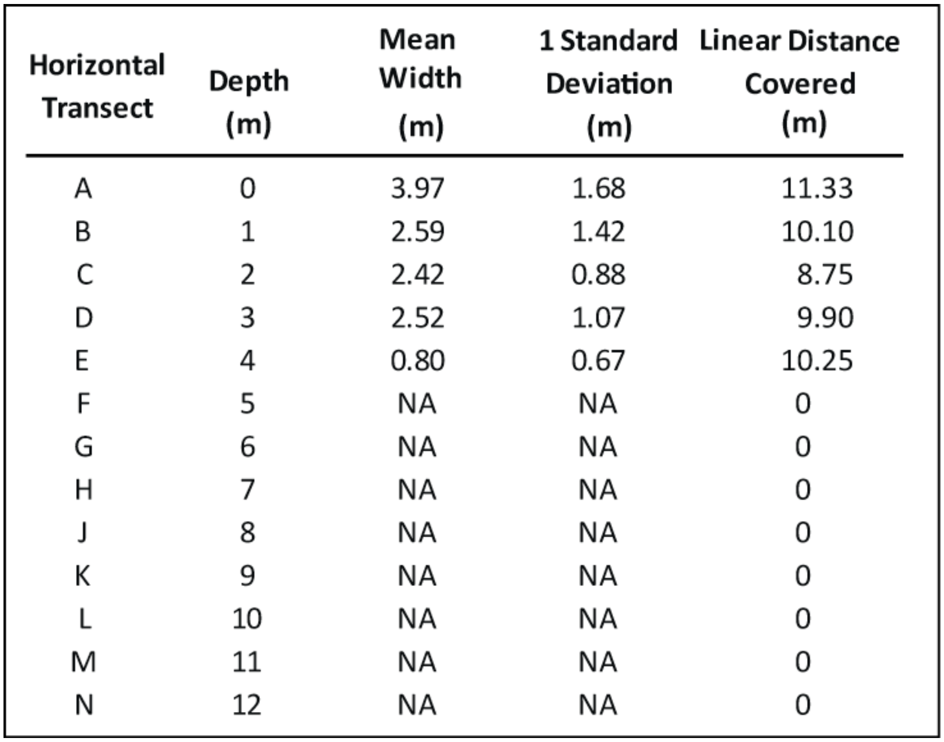

Horizontal Transect	Depth (m)	Mean Width (m)	1 Standard Deviation (m)	Linear Distance Covered (m)
A	0	3.97	1.68	11.33
B	1	2.59	1.42	10.10
C	2	2.42	0.88	8.75
D	3	2.52	1.07	9.90
E	4	0.80	0.67	10.25
F	5	NA	NA	0
G	6	NA	NA	0
H	7	NA	NA	0
J	8	NA	NA	0
K	9	NA	NA	0
L	10	NA	NA	0
M	11	NA	NA	0
N	12	NA	NA	0

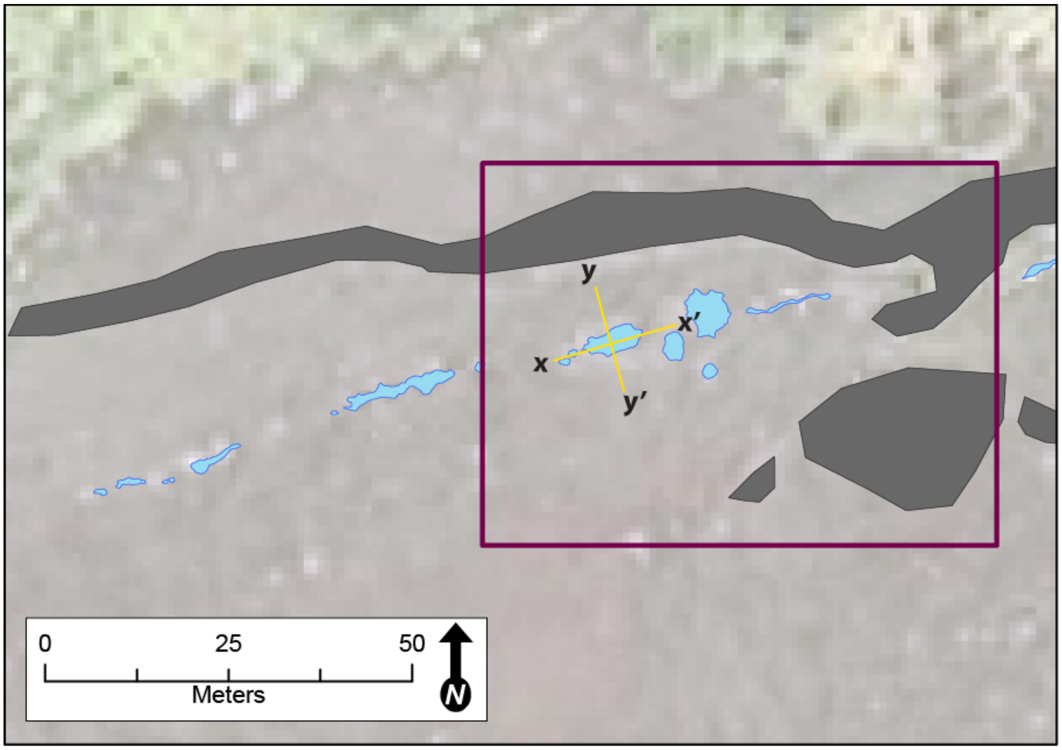

Figure 3.7 A Map showing part of segment V, location of LiDAR area 3 is marked with the purple box. Yellow lines indicate cross sections x-x' in Fig. 3.7b and y-y' in Fig. 3.7c.

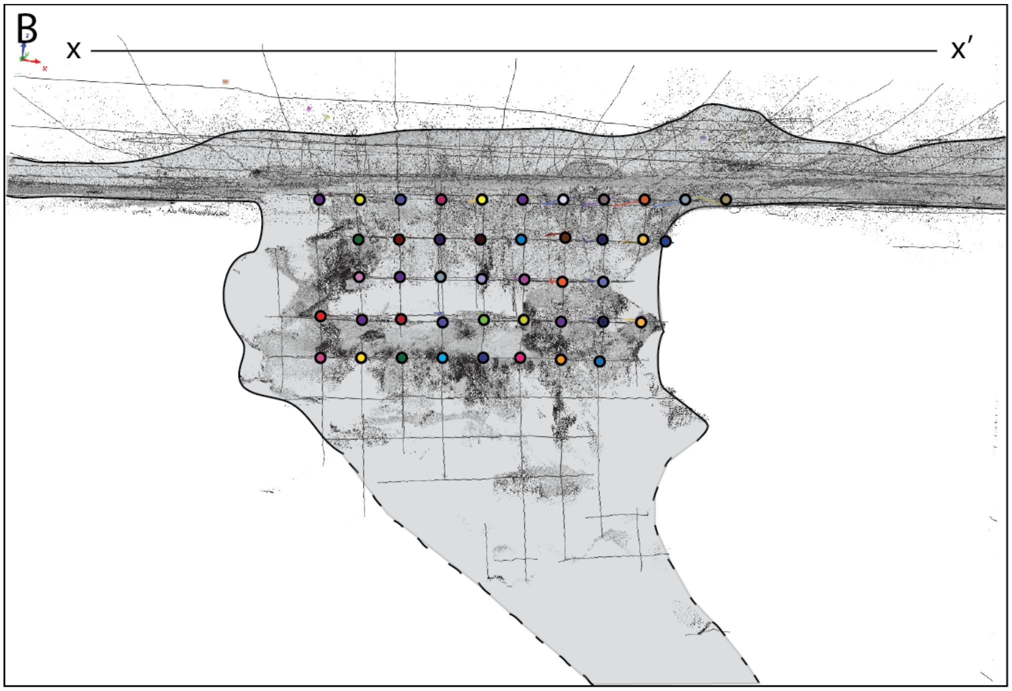

Figure 3.7 continued B View of LiDAR point cloud perpendicular to vent/conduit strike. View angle is to the north. Black lines denote boundaries of the LiDAR cloud. Black line is dashed where the fissure wall is presumed to be, but LiDAR data are too scarce or have too many holes to know with certainty. Colored circles at grid point intersections indicate locations of vent width measurements.

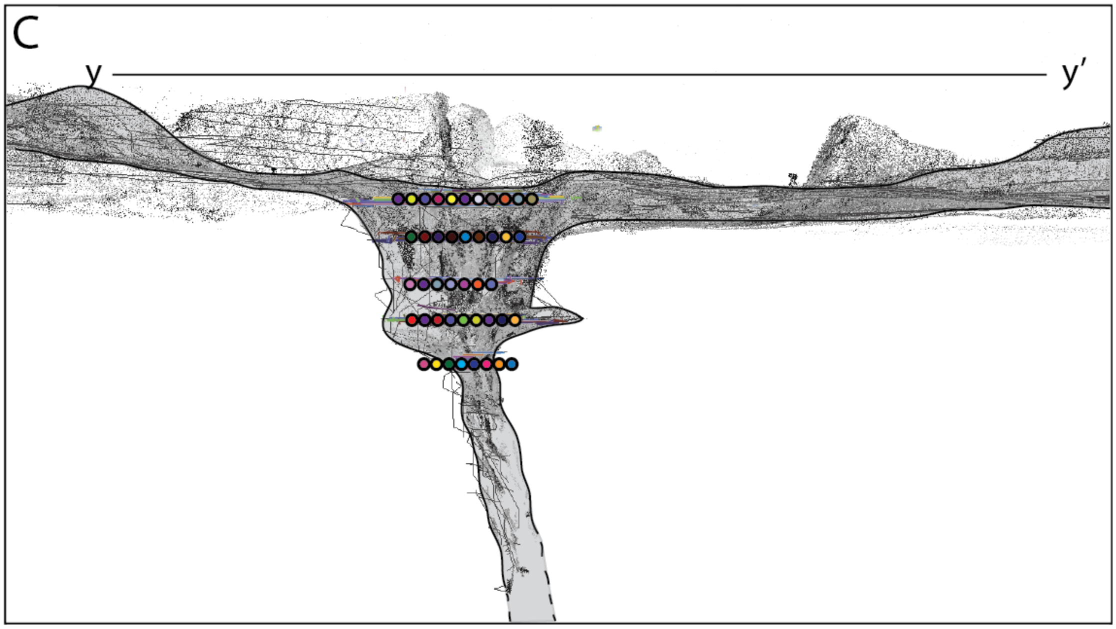

Figure 3.7 continued C View of LiDAR point cloud down strike to the east. Black lines denote ground surface in the closest parts of the LiDAR cloud, but ramparts can be seen above this line and are located east of the vent. Colored circles extending across the vent/conduit correspond to the depths of width measurements, and correlate to the same colors/measurements in Fig. 3.7b.

3.4.7 Depth and nature of the shallow conduit to vent transition

The depths measured for the fissure system through the entire field area (Table 3.4) range from 0.4 m (vents filled in by talus or drain-back) to over 100 m (the maximum length our plumb bob could extend). The mean recorded depth was 23 m. In most vents, one could typically feel the plumb bob ricocheting off irregularities of the vent or conduit wall indicating that irregularities persist with depth in the system.

Most of segment II, except for vents 13 and 14, is at least 100 m deep. On the west end of segment II, the plumb bob bounced off of irregularities during parts of the descent, but on the east side of segment II, especially vent 12, it dropped smoothly. On segment III, vents 17 (LiDAR area 2) and 27 are over 100 m deep. Vent 35 on segment IV also reached 100 m at both ends of the linear vent. The western end of vent 45 on segment V is at least 100 m deep and is separated from the rest of the linear vent (< 100 m deep) by a spatter saddle.

The feeder conduit is likely continuous along each fissure segment when it is deeper than can be directly observed (i.e., greater than ~10 m). At greater depth, which I have not been able to measure, the conduit must be continuous along entire fissure system, as the vents were all fed by the same dike.

Table 3.4 Table of orientation, depth, and length measurements of each vent. Strike, when the fissure vent was long enough to have an orientation, was measured with a Brunton compass. One strike measurement was taken for the whole vent, from the western tip to the eastern tip. Fissure depth was measured in each vent by a plum bob attached to a 100 m tape measure. Depth was recorded at the transition between when the plum bob would freely drop and when the tape became slack. For some vents, the plumb bob did not reach the bottom of the fissure and the maximum length of the tape is recorded as the measurement. The distance along the vent length of each depth measurement (as well as total vent length), from the *vent's western tip*, is listed when the vent is a fissure geometry. Vent 22 is filled with plant material and dead foliage, making a depth measurement impossible and is listed as "na."

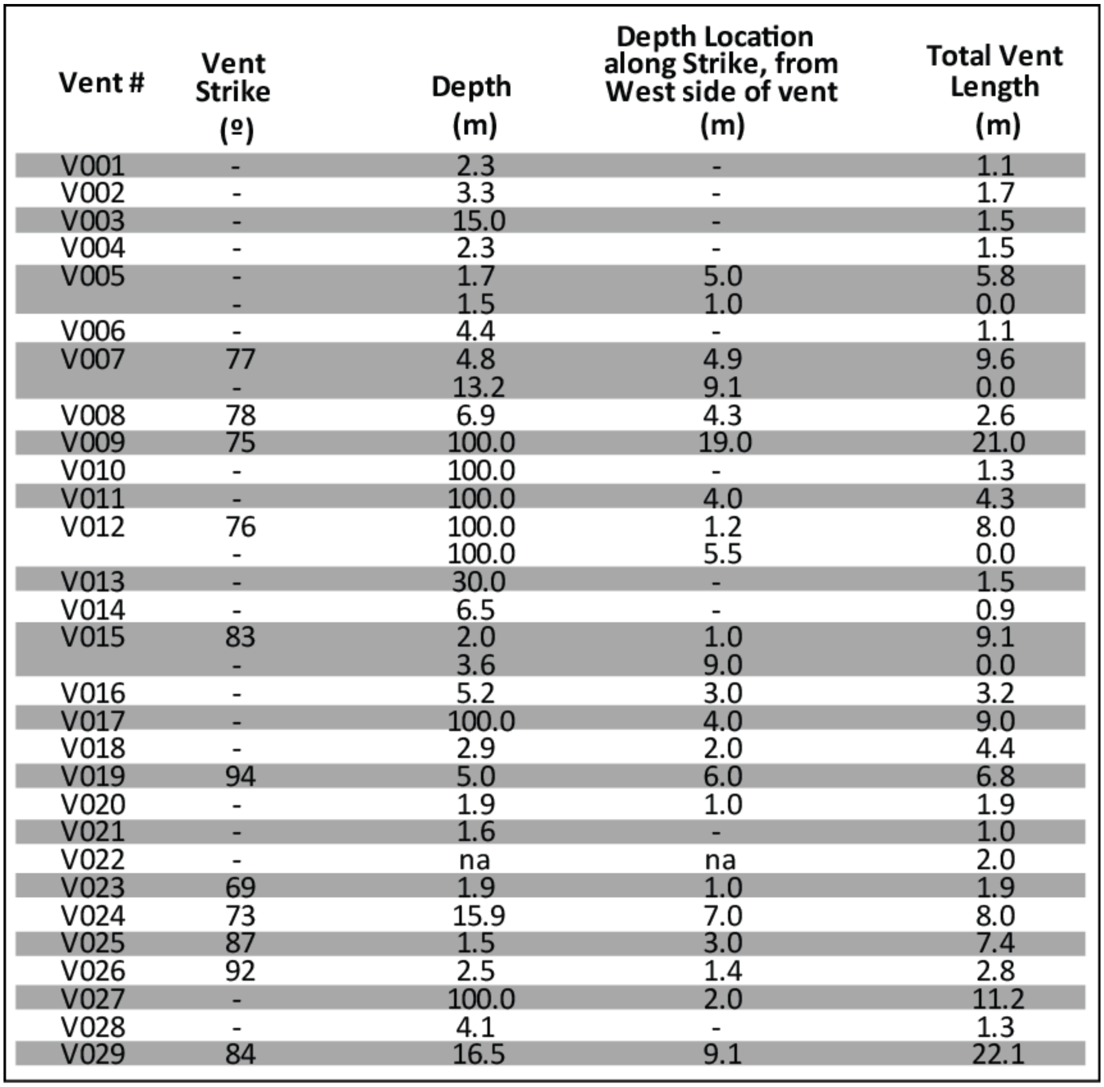

Vent #	Vent Strike (º)	Depth (m)	Depth Location along Strike, from West side of vent (m)	Total Vent Length (m)
V001	-	2.3	-	1.1
V002	-	3.3	-	1.7
V003	-	15.0	-	1.5
V004	-	2.3	-	1.5
V005	-	1.7	5.0	5.8
	-	1.5	1.0	0.0
V006	-	4.4	-	1.1
V007	77	4.8	4.9	9.6
	-	13.2	9.1	0.0
V008	78	6.9	4.3	2.6
V009	75	100.0	19.0	21.0
V010	-	100.0	-	1.3
V011	-	100.0	4.0	4.3
V012	76	100.0	1.2	8.0
	-	100.0	5.5	0.0
V013	-	30.0	-	1.5
V014	-	6.5	-	0.9
V015	83	2.0	1.0	9.1
	-	3.6	9.0	0.0
V016	-	5.2	3.0	3.2
V017	-	100.0	4.0	9.0
V018	-	2.9	2.0	4.4
V019	94	5.0	6.0	6.8
V020	-	1.9	1.0	1.9
V021	-	1.6	-	1.0
V022	-	na	na	2.0
V023	69	1.9	1.0	1.9
V024	73	15.9	7.0	8.0
V025	87	1.5	3.0	7.4
V026	92	2.5	1.4	2.8
V027	-	100.0	2.0	11.2
V028	-	4.1	-	1.3
V029	84	16.5	9.1	22.1

.

Table 3.4 continued

Vent #	Vent Strike (º)	Depth (m)	Depth Location along Strike, from West side of vent (m)	Total Vent Length (m)
V030	-	0.4	-	1.3
V031	75	30.0	1.0	24.9
	-	4.7	3.7	0.0
	-	30.0	23.8	0.0
V032	-	41.2	1.5	4.0
V033	-	13.4	1.5	2.0
V034	-	1.4	-	1.4
V035	70	100.0	11.2	16.7
	-	100.0	20.4	0.0
V036	74	15.7	13.7	4.5
V037	-	30.0	26.5	24.7
V038	-	4.4	1.0	3.0
	-	4.1	2.5	0.0
V039	-	3.8	2.0	5.0
V040	-	4.8	2.0	11.0
V041	-	1.2	1.0	3.8
V042	-	3.0	1.0	1.5
V043	-	1.5	1.4	6.5
V044	-	7.3	1.2	17.3
V045	-	100.0	0.5	10.0
	-	4.0	8.0	0.0
V046	-	0.6	-	2.6
V047	-	22.3	3.0	13.2
V048	-	1.5	2.0	4.1
V049	-	2.4	1.5	2.7
V050	-	24.7	2.0	6.2
V051	82	6.5	7.3	21.6
V052	72	4.2	5.5	35.0
	-	4.0	25.7	0.0
V053	73	30.0	8.4	27.0
	-	17.1	17.2	0.0
V054	75	12.7	8.5	67.5
	-	4.5	29.8	0.0
	-	30.0	55.8	0.0

.

3.5 Interpretation and Discussion

3.5.1 Fissure system geometry

The overall fissure geometry and the account by Swanson et al. (1979) indicate the Mauna Ulu fissure was a rectilinear dike at depth that adjusted to slightly rotated surface stress orientation, creating the observed series of fissure segments. It was postulated in Swanson et al. (1979) that the portion of the fissure still preserved was erupted along an existing fault in the extreme eastern portion of the Koʻae fault zone. The geometry of the Mauna Ulu fissure is similar to that of non-eruptive cracks (100 m south) and non-eruptive fissures elsewhere on Kīlauea, supporting their postulation. I agree with Swanson et al. (1979), that the 1969 fissure exploited an existing fault in the Koʻae Fault Zone as it propagated west through our field area. This took 3 hours for 1 km of late-stage westward extension as compared to 15 min for bilateral extension for the initial, but now buried, 4 km of the fissure east of the field area.

Fissure segment sinuosity in the field area may be a reflection of 1) the surface stress field, possibly as a precursor to en echelon formation, or 2) large scale expressions of crack tips beginning to interact in the manner described by Pollard et al. (1982). It is unclear whether the sinuosity and en echelon steps are primary features of the fault plane that was later exploited by the dike, or whether these features were superposed by the propagating dike in 1969. Building from Ryan and Sammis (1978), Pollard et al. (1982), and Goehring et al. (2006), the irregularities in fissure segments can be interpreted as drainback-covered mode I openings of shrinkage and cooling cracks in lava flows that covered the ground surface in the previous eruption in that area (approximately 1600s). It is likely that fault propagation eastward from the Koʻae fault zone utilized these joints and weaknesses (Pollard and Aydin, 1988; Holland et al., 2006).

3.5.2 Vent geometry

There is no obvious relationship between the eruption rates (or fountain heights) as inferred from the heights of spatter ramparts (documented in Chapter 2) and flared or non-flared vent geometries. The highest spatter accumulation rates instead occur at small offsets and larger en echelon steps in the fissure, where ejecta accumulated from the combined output of two non-collinear vents. Walls of flared vents always possess flow textures indicative of drain back. Drainback was likely accompanied by low spattering that produced the isolated dense spatter seen around many vents (described in Chapter 2).

During peak discharge of the May 24, 1969 fissure eruption at Kīlauea, lava covered the fissure to depths of 2 to 3 m above the present ground surface, which itself is the 1969 deposit that lies up to 1.5 m above the pre-eruption ground surface at the vent (Chapter 2). The downward transition from localized vent to continuous fissure, where present, is located mostly between 1 and 2 m depth, and implies that the transition can lie in either the lower 1969 lava (above the pre-eruptive ground surface) or in the top few meters of the pre-eruptive ground surface. The fissure to vent transition cannot be measured in the narrower range of fissure widths because there is no flaring.

Combining my results with conclusions from the theoretical work of Wilson and Head (1981) and Mitchell (2005), and with the observations and timelines given in Swanson et al. (1979), I interpret the narrow fissures with no flaring to likely represent the original shape of the dike or exploited fault plane. Where vents are flared, and taking into account the work on thermal and mechanical erosion of conduit walls, I put forward the following possible interpretations:

- *Mechanical erosion:* Major flaring is a result of mechanical erosion of the conduit walls to achieve a lithostatic pressure balance in the erupting mixture.

- *Thermo-mechanical erosion:* Minor flaring is a result of flow abrasion by the ascending magma-gas mixture and/or sub-solidus heating of the wall rock, which facilitates abrasion by the mixture. Vents may have also widened during viscous late stage drain-back as lava flowed over the vent walls in a reverse direction.

- *Thermal erosion:* Pure thermal erosion is unlikely to have played a major role during the May 24–25 eruption, as many of the models discussed in the background section required significantly longer than one day to initiate melting of the basalt quenched on the fissure walls. The Mauna Ulu Ep 1 WZ vents erupted for 17.25 hr, and thus there was not enough time to allow for the wall rock to melt sufficiently. If any melting did occur on the vent walls, the penetration depth was not likely to be a significant contributor to the vent flaring measured in the field.

Cooling induced viscosity increase causing sluggish flow or flow stagnation within the dike segments can explain the localization of fountains as they waned inwards from the narrow tips of the en echelon steps within. Flow localization also sets the premise that fountains did not shift position along the fissure, but remained fixed in space during temporal evolution of the vents. Wylie et al. (1999) stated that thermo-viscous fingering instabilities occur at low discharge rates, and do not strictly correspond to significantly reduced driving pressure from the source. The May 24-25 fissure provides conditions favorable for thermo-viscous fingering instabilities as the effusion rate was low and steady, and the geometry is broadly rectilinear. Magma driving pressure must have declined substantially at some point, however, as lava ponded on the surface was able to drain back into the system (Chapter 2). It seems likely that the same pathways defined by instabilities used for magma ascent were also used for magma drainback and descent. Furthermore, drainback lava that descended in these pathways had a sufficiently low viscosity (i.e. remained hot enough) that vents and the shallow conduit were unobstructed for several meters to >100 m depth. The dike may currently be held open in the manner described by Daniels et al. (2012), where lava cooling at the tips of segments restricts the center from elastically closing after the magma had drained away. However, it cannot be ruled out that the fault the dike intruded was opened in a mode 1 manner during eruption and never relaxed back after the eruption was over. Geodetic data from HVO show minimal ground motion changes over the last several decades in this area of Kīlauea (personal communication, Don Swanson).

3.5.3 Constraints on fissure width for models of weak basaltic fountains

Vent or fissure radius is an important input parameter for models of Hawaiian eruption dynamics. Most models do not explicitly state a source for this input, but use a range of values between 3 and 14 m for circular vents (Wilson and Head, 1981; Head and Wilson, 1989; Parfitt and Wilson, 1995), and 0.2–10 m for linear vents (Wilson and Head, 1981; Hardee, 1986; Head and Wilson, 1989; Parfitt and Wilson, 1994). Our data agree with the fissure widths originally proposed by Wilson and Head (1981) and suggest that a surface width value of ≤1 m is appropriate for non-flared linear vents, whereas a surface width value of ~1.5 m is applicable for flared linear vents. For more realistic outcomes, future modeling of low-intensity fissure fountains should therefore adopt width values in the lower end of the range previously used.

3.6 Conclusions

This contribution has described the detailed geometry of the May 1969 Mauna Ulu eruptive fissure at Kīlauea. It is characterized by en echelon geometry, subtle sinuosity, noticeable irregularity of fissure width, and development of at least 54 vents along 880 m of fissure. I interpret the en echelon pattern as an early feature derived from a single 80° trending dike that rose with minimal lateral propagation to a shallow level from Kīlauea’s ERZ before segmenting, and subsequently extending westward 1 km through interacting with the ENE-trending Koʻae fault system. Fissure sinuosity likely developed from the stress field of the ERZ and fault interactions in the eastern Koʻae Fault Zone, regardless of whether the stress field is primary to the fault intruded or the intruding dike. Fissure irregularity is most likely the result of pre-existing cooling joints in the ground surface that were opened in a mode 1 fashion during dike emplacement. The flared versus non-flared vent geometries show no obvious relationship to fountain height (inferred from rampart geometry). Vent localization was the inevitable consequence of the cooling induced viscosity increase leading to flow stagnation . Flaring, where present, is a result of syn-eruptive mechanical erosion and aided with thermo-mechanical abrasion. A lack of flaring, combined with narrow fissure widths, indicates that the original geometry of the magmatic pathway is preserved at the Mauna Ulu fissure.

Chapter 4

Contrasting patterns of vesiculation in low, intermediate, and high Hawaiian fountains: a case study of the 1969 Mauna Ulu eruption

4.1 Introduction

Rapid fluctuations in eruptive behavior are observed during eruptions at basaltic volcanoes like Kīlauea, with growing evidence suggesting behavior cannot be correlated only to eruption rate but also to the fluid dynamics of two-phase (melt-gas) ascent and segregation in the shallow volcanic plumbing system (Wilson, 1980; Wilson and Head, 1981; Head and Wilson, 1989; Cashman and Mangan, 1994; Parfitt and Wilson, 1995; Jaupart, 1996; Papale, 1999; Parfitt, 2004; Gonnerman and Manga, 2007; Kamenetsky et al., 2007). The manner of melt-gas segregation (Mangan et al., 1993), and the depths at which it occurs (Gerlach and Graeber, 1985; Gerlach et al., 2002), are thought to be particularly important controls on style (Allard et al., 2006; Spilliaert et al., 2006). Pre-eruption abundance of dissolved gases (Anderson and Brown, 1993; Johnson et al., 1994; Dixon, 1997; del Carlo and Pompilio, 2004; Papale, 2005), the dimensions of the plumbing system (Bower and Woods, 1998), the degassing depths and rates of different gas species (Metrich et al., 2004; Papale, 2005; Papale et al., 2006; Spilliaert et al., 2006; Burton et al., 2007; Edmonds and Gerlach, 2007), melt and bulk rheology (Webb and Dingwell, 1990; Manga et al., 1998; Saar et al., 2001; Pal, 2003; Llewellin and Manga, 2005; Caricchi et al., 2007; Hui and Zhang, 2007), rates of bubble rise and growth, and the extent of syn-eruptive growth of crystals (Mangan et al., 1993; Cashman and Mangan, 1994; Lautze and Houghton, 2006, 2007) combine to define complex feedbacks that permit reversible shifts in eruption mechanisms, style, and intensity (Dingwell, 1996; Wilson, 1999; Zhang, 1999; Spieler et al., 2004; Namiki and Manga, 2005; Taddeucci et al., 2004; Ripepe et al., 2005).

Hawaiian fountains, defined as up-rushing jets of gas and incandescent pyroclasts (Wolff and Sumner, 2000), represent the weak end-member of sustained explosive eruptions (Walker, 1973). By explosive, I refer to the disruption of magma into fragments by gas expansion upon ejection (Wolff and Sumner, 2000). Kīlauea volcano is the type locality of Hawaiian-style explosive eruptions, or Hawaiian fountains, but this style has been observed at many other basaltic volcanoes (e.g., Fedotov et al., 1980, Polacci et al., 2006). Historical Hawaiian fountains around the world vary in height by three orders of magnitude from <10 m to more than 1.5 km (Alparone et al., 2003). At Kīlauea specifically, documented heights range from 8 to 580 m, with various vent geometries from single circular vents to short fissure segments within kilometer-long fissure systems (Richter et al., 1970; Swanson et al., 1979, Wolfe et al., 1998).

4.1.1 Previous work on mechanisms of Hawaiian eruptions

Kīlauea’s recent pyroclastic history includes three high fountaining (>400 m) eruptions (Kīlauea Iki in 1959 [Richter et al., 1970], Mauna Ulu in 1969–1974 [Swanson et al., 1979, Tilling et al., 1987], and Pu‘u ‘Ō‘ō in 1983–1986 [Wolfe et al., 1988]), which had multiple episodes separated by quiescent intervals of gas pistoning, persistent passive degassing, and spattering. Other historic Kīlauea fountaining eruptions have been characterized by single episodes of low (<50 m) fountain activity from fissure sources.

Two eruption dynamics models currently exist for Hawaiian fountaining. In both, fountains are produced by rising magma that exsolves volatiles as bubbles, which are buoyant in proportion to bubble size. Some workers (e.g., Wilson, 1980; Wilson and Head, 1981; Parfitt and Wilson, 1995; Parfitt et al., 1995; Slezin, 2003; Parfitt, 2004) propose that, for small gas bubbles and high magma ascent rates, late-formed bubbles are unable to rise appreciably relative to the melt phase, making them effectively coupled in the shallow conduit. These small bubbles produce a highly vesicular magma, expanding and fragmenting at a shallow depth within the conduit. Others suggest that collapse of foam in a shallow magma storage zone results in continuous annular two-phase flow of gas and melt up the conduit (Vergniolle and Jaupart, 1986, 1990; Jaupart and Vergniolle, 1988, 1989; Vergniolle and Mangan, 2000). Our focus is not on resolving which is correct, but rather on examining how fountain height and pyroclastic vesicle textures are correlated. In the end, as I will discuss, our interpretations favor the model put forth by Wilson (1980) and Parfitt (2004) because the textures of the pyroclasts do not indicate a foam collapse event (i.e., there are no preserved outgassing or collapse bubble shapes).

Differences in the timing and rates of bubble nucleation, growth, and coalescence can be quantified by microtextural vesicularity studies, which have shown that basaltic eruption products are highly variable in vesicle number densities (VND), size distributions (VSD), and volume distributions (VVD), (e.g., Cashman and Mangan, 1994; Lautze and Houghton, 2006; Sable et al., 2006, 2009; Costantini et al., 2010; Stovall et al., 2011). Location and duration of bubble nucleation, an inevitable consequence of increasing melt supersaturation during shallow magma ascent, are critical factors in driving the intensity and style of the activity (e.g., Gerlach and Graeber, 1985; Toramaru, 1995). Once early gas bubbles nucleate, both diffusive and decompressive growth begins. The largest bubbles can then rise buoyantly through the magma at variable rates relative to the melt phase (e.g., Burton et al., 2007; Edmonds and Gerlach, 2007). Volatiles can continue to be supersaturated as initial bubbles help the magma ascend, driving continued nucleation at shallow levels in those portions of the melt remote from existing bubbles. Laboratory and numerical studies have shown that the timing and degree of bubble coalescence are critical in distinguishing between styles of basaltic volcanism (e.g., Gonnerman and Manga, 2007; Namiki and Manga, 2006, 2008). Measurements of bulk vesicularity, VND, VSD, and VVD in basaltic pyroclasts are powerful tools with which to understand shallow conduit processes including decompression, degassing, outgassing, and shallow magma ascent histories (e.g., Lautze and Houghton, 2005; Sable et al., 2006, 2007; Costantini et al., 2009; Stovall et al., 2011, 2012).

Vesicularity studies on pyroclasts from Hawaiian fountains are limited. Few quantitative data exist except for the pioneering work on high fountains at Puʻu ʻŌʻō (Mangan et al., 1993; Cashman and Mangan, 1994; Mangan and Cashman, 1996) and recent studies of 3 episodes of the 1959 Kīlauea Iki eruption by Stovall et al. (2011, 2012). An order of magnitude variation in bubble number densities in single pyroclasts attests to the complexity of shallow degassing and outgassing on short length scales. The relative influences of bubble nucleation, growth, coalescence, and collapse can be inferred from a combination of number density and vesicularity data (e.g., Stovall et al., 2011; 2012). I combine vesicularity data from 4 diverse episodes of the Mauna Ulu eruption, a complex and long-lived eruption, to include low fountaining behavior (discharge rates an order of magnitude lower than previously documented), thus extending the range of documented Hawaiian events. Our goal is to understand the role of degassing and outgassing in modulating diversity across the complete range of Hawaiian explosive volcanism (mass discharge rates of 4 $x10^4$ to 1 $x10^6$ kg s^{-1}).

4.2. Mauna Ulu 1969 – selection of episodes and samples for study

The Mauna Ulu eruption of 1969–1974 was Kīlauea's second longest and second most voluminous flank eruption in its recorded history (Fig. 4.1, Swanson et al., 1979, Tilling et al., 1987). Twelve fountaining episodes occurred from May 24, 1969 to Dec 31, 1969. During fountaining episodes, lava accumulated in the vent creating syn-eruptive lava flows until the supply rates dropped, fountains heights decayed, and lava drainback began. Between episodes, magma rose and fell episodically in the vent, accompanied by spattering and/or gas-pistoning, and sometimes spilling out to form short lava flows. All of the inter-episode activity was irregular (i.e., never periodic).

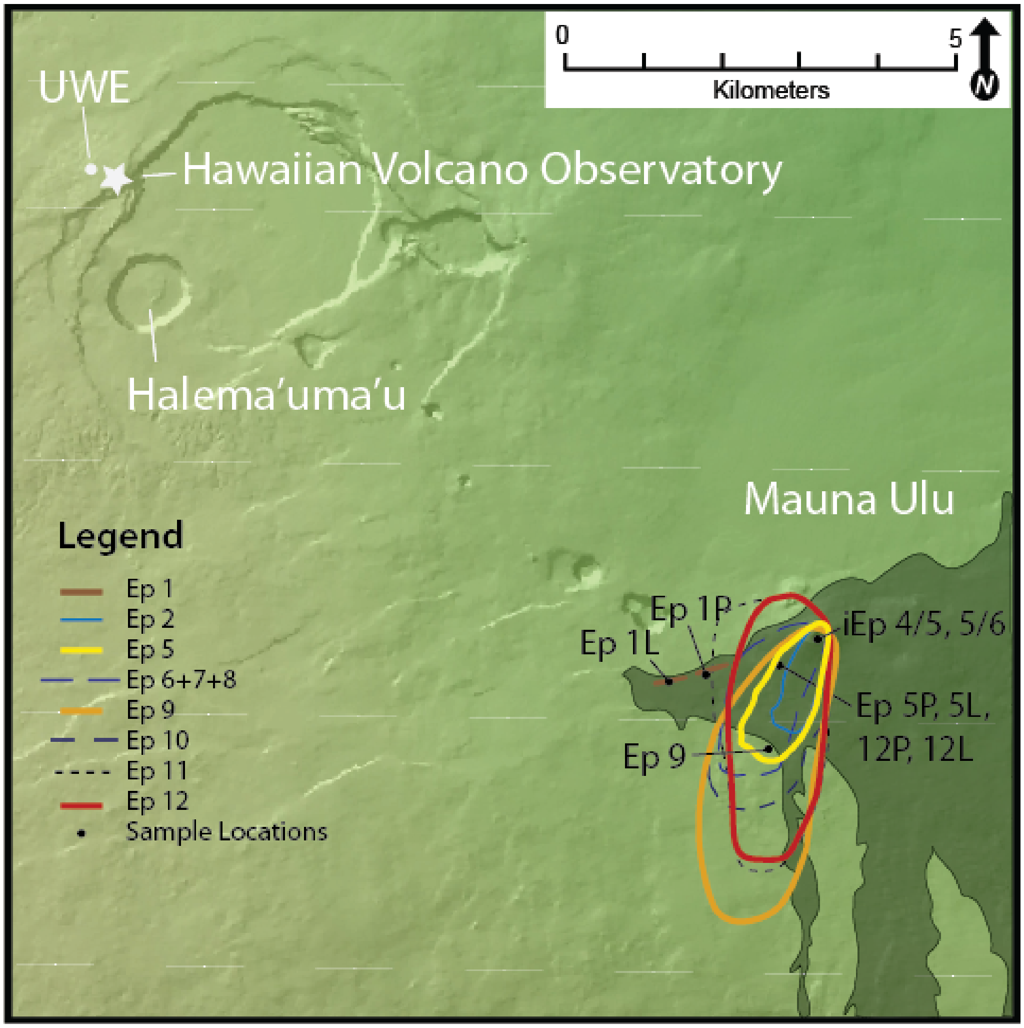

Figure 4.1 Mauna Ulu is located on the East Rift Zone, southeast of Kīlauea 's summit, the Hawaiian Volcano Observatory, and Halemaʻumaʻu, where the 2008–present-day activity is located. Also shown is the station for tilt readings (UWE) presented in Fig. 4.2. In the lower right is the outline of the Mauna Ulu 1969–1974 eruption deposits. The darker shaded area indicates part of the lava flow field, colored contours outline pyroclastic deposits of the eruption studied in this paper, and black dots indicate locations of analyzed samples.

Episode 1 built spatter ramparts along segments of a 5 km fissure. During later fountaining episodes, a single 50 m high tephra cone, comparable in size and shape to that of Kīlauea Iki (Swanson et al., 1979), formed around two vents. The westernmost kilometer of the episode 1 ramparts remains preserved and accessible today, but much of the episodes 2–12 tephra deposit and cone were buried by up to 70 m of lava flows (Swanson et al., 1979). Dispersal maps (redrawn and combined in Fig. 4.1) and maximum cone heights were recorded by Swanson et al. (1979), but dispersal data (thickness, grainsize, density) were not collected during the eruption. This study focuses on selected episodes from the Hawaiian fountain activity; all monitoring data sets recorded by HVO (fountain heights, cumulative eruptive volumes, summit extension, summit tilt, and seismicity from the summit, upper east rift zone and middle east rift zone [Swanson et al., 1979]) between May and December, 1969 are shown in Fig. 4.2.

Fountain activity over the twelve episodes (described in detail in Swanson et al., 1979) varied greatly in height and source vent geometry, but episodes were fairly similar in duration (< 75 hr). Source vent geometries ranged from a classical en echelon fissure system (Ep 1) to single and double sub-circular vents. Fountain heights were 30–540 m (the second highest ever recorded at Kīlauea). For the purposes of this dissertation, I define low fountains as <100 m in height, intermediate fountains as 100–400 m in height, and high fountains as

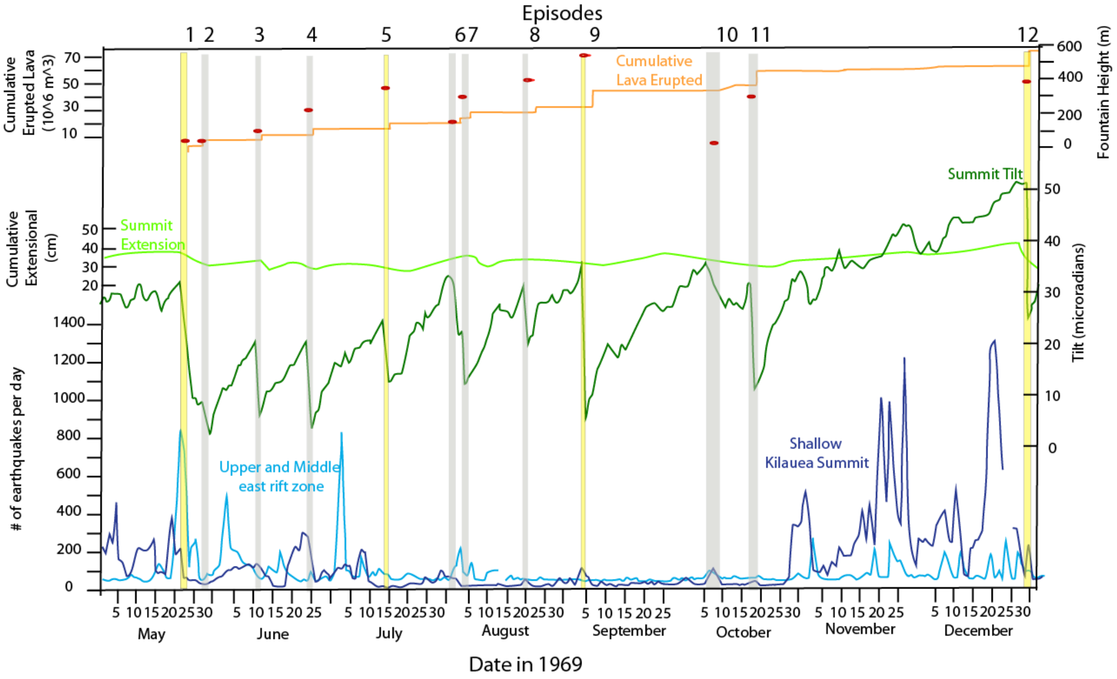

Figure 4.2 Summary of all geophysical data taken by HVO during stage 1 (May–December, 1969) of the Mauna Ulu eruption, combined and reproduced from Swanson et al. (1979). The twelve fountaining episodes are indicated by the vertical bars, where the thickness of the bar correlates to duration of fountain activity. Yellow bars indicate episodes included in this paper. Data sets from top to bottom, labeled on the left axis, are cumulative erupted lava (orange line), cumulative summit extension (light green line), and number of earthquakes per day at the summit (dark blue line) and along the upper and middle east rift zone (light blue line). Data sets from top to bottom, labeled on the right axis, are fountain height (red ellipses) and summit tilt (dark green line). The x-axis is the date in 1969, labeled by month and every 5th day.

.

>400 m in height (Houghton, unpublished data). Between fountaining episodes (Eps), I term the intervals of weak spattering, gas pistoning, and lava effusion (Swanson et al, 1979) the ‘inter-episodes’ (iEp) (e.g., activity between the fountains of episodes 1 and 2 is iEp 1/2).

Episodes selected for study in this paper were chosen based primarily on sample availability and a desire to cover the range of types of activity. It is no longer possible to sample with certainty the products of most episodes, therefore, for all episodes except Ep 1 and Ep 9, I was constrained to the small samples preserved in the USGS collections. Episode 1 was the only fissure-fed event with <50 m high fountains, and I could sample tephra from it in 2009–2010. Episode 5 was a 375 m high intermediate fountain from two sub-circular vents 75 m apart. USGS samples are available from the peak of fountain activity as well as iEp 4/5 and iEp 5/6. Episode 9 was a fountain 540 m in height from a single circular vent and was the most powerful fountaining episode during the 1969 Mauna Ulu eruption. Alone among the episodes, it produced dominantly reticulite, so that the products are clearly recognizable and allow us to sample it with certainty in the medial field. Episode 12 was an intermediate fountain 390 m high, from two vents that evolved into a single vent, and was chosen to include the final episode of the eruption.

4.3 Materials and Methods

4.3.1 Sampling

Sample collection occurred in 1969 by USGS and in 2009/2010 by the University of Hawaiʻi (UH). In 1969, the USGS collected samples at the time of eruption during fountains of Ep 5 and Ep 12, as well as spattering from iEp 4/5 and iEp 5/6. The USGS collected Ep 5 and Ep 12 samples at the ʻĀloʻi crater overlook parking lot (Fig. 1), which is now buried. Sample 5P (P = peak activity) was collected during the peak phase of fountain activity at ~04:00 HST on July 15, 1969, and sample 5L (L = late activity) was collected at 06:45 on the same day. Sample 12 was collected at noon on Dec 30th. Inter-episodes iEp 4/5 and iEp 5/6 were sampled at the Mauna Ulu summit vent(s) on July 7, 1969 and July 30, 1989 respectively. All the USGS sample sizes are <25 clasts, reducing the statistical quality of our vesicle data, but assuring that episode of origin is specifically known.

In 2009–2010, UH collected samples from the Ep 1 fissure rampart and medial fall deposits of episodes 3–12 (1.5 km southwest (SW) of source, the closest pyroclastic site available to Mauna Ulu at the present time). Two proximal Ep 1 fissure samples (Fig. 4.1) were taken of tephra from the peak fountain activity (10 m south of the fissure) and late-stage spatter (40 m north of the fissure). No distal pyroclastic deposit formed in Ep 1 (Chapter 2). The proximal cone and tephra blanket created by Eps 2–12 are buried under the Mauna Ulu shield, and individual episodes in the medial sample site (Fig. 4.1) cannot be recognized, except for the Ep 9 reticulite. In the absence of clear internal stratigraphy for most episodes at the medial site, I collected density samples at regular intervals (Fig. 4.3) from the base of the stratigraphy (Ep 3, the first episode to produce a fall deposit at this distance) to the Ep 9 marker horizon, a reticulite-rich unit, and from the Ep 9 marker to the top of the sequence (Ep 12). I use a combination of the USGS and UH samples in our study for measurements of vesicularity and VSD.

4.3.2 Density and bulk vesicularity

We measured density in the lab following the techniques described in Houghton and Wilson (1989). Altogether, for Ep 1 I measured 100 peak tephra clasts and 100 late stage spatter clasts, for Ep 9 I measured 100 clasts, and for the USGS samples of Ep 5, Ep 12, iEp 4/5, and iEp 5/6, I measured 15, 24, 14, and 10 clasts respectively. I calculated vesicularities using a dense rock equivalent (DRE) of 2800 kg m^{-3}. Of these clasts, I selected for thin sections 7 clasts for Ep 1P and Ep 1L, 4 clasts for Ep 9 and Ep 5, and 2 clasts for Ep 12, iEp 4/5, and iEp 5/6. Thin sections have clear epoxy to preserve vesicle textures, and were chosen to represent accurately the mode vesicularities, as well as the minimum and maximum vesicularities for the larger UH samples. Of the samples chosen for thin sections, the 1–2 most representative slides were chosen for quantification and are presented here.

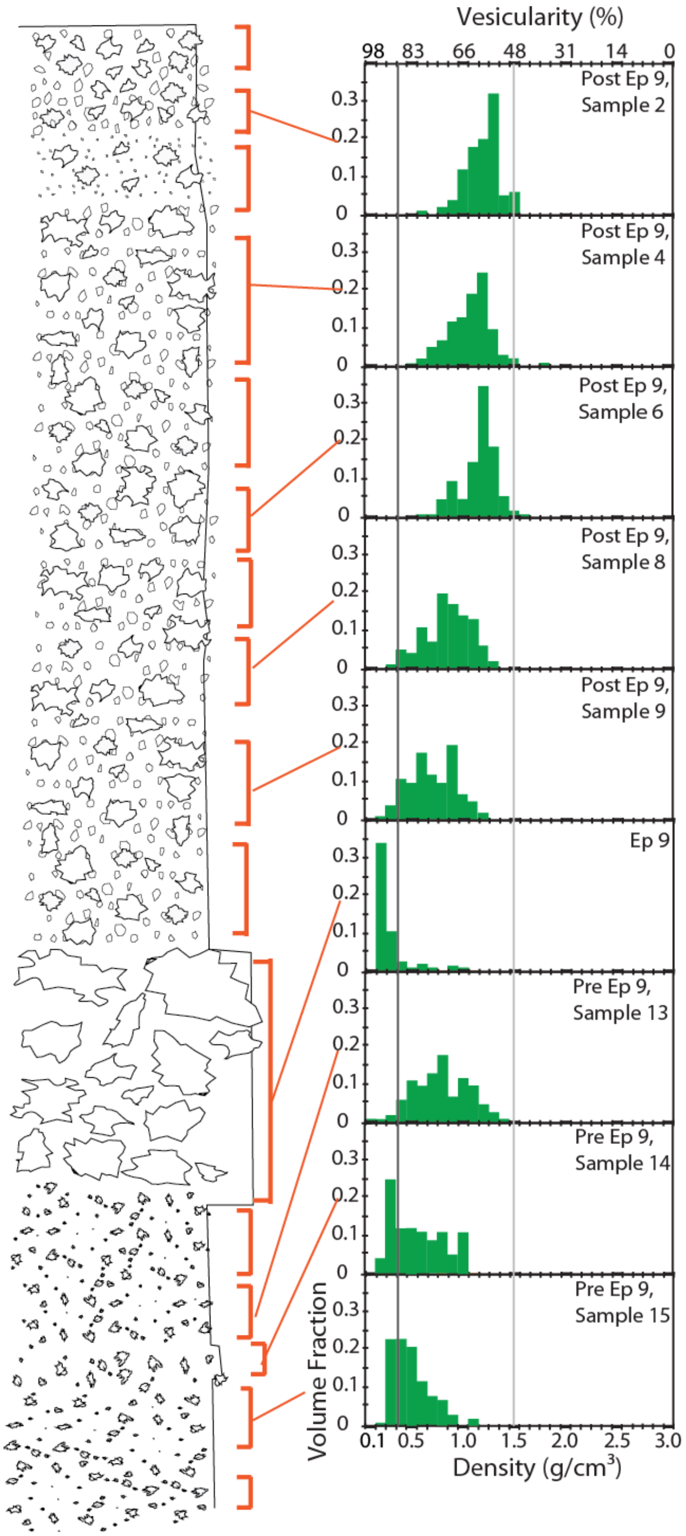

Figure 4.3 Stratigraphic log of the medial sampling location (1.5 km SW of Mauna Ulu). The thick reticulite bed of Ep 9 was the only identifiable layer. The rest of the deposit is massive. Regular intervals were used for density sampling, and a selection of the histograms are shown. The light grey line corresponds to a density of 1.5 g/cm^3 (48% vesicularity) and the dark grey line corresponds to a density of 0.35 g/cm^3 (88% vesicularity).

4.3.3 Textural analysis

4.3.3.1 Vesicle number, size, and volume

Textures were documented at three magnifications (x) (scan, 25x, 100x) in nested trees following the technique described in Shea et al., (2010). Scans were obtained via transmitted light on a Hewlett-Packard flatbed scanner at 1200 dots per inch (dpi). All other magnifications were acquired using a Japan Electronics Optics Laboratory (JEOL-5900lv) scanning electron microscope (SEM) operating at 15 kilovolts accelerating voltage and 1 nanoampere beam current in the backscatter electron image mode. All images were cleaned in Adobe Photoshop and turned binary, with white designating melt and black designating vesicle cross sections. Bubble size distributions (N_a, the number of bubbles per unit area) in 2D were converted to three dimensional (3D) volume size distributions (N_v, number of bubbles per unit volume) and VND (Sahagian and Proussevitch, 1998). A correction for the melt volume (N_v^m; Klug et al., 2002) was also performed to avoid underestimating number densities of highly vesicular samples.

4.3.3.2 Vesicle shape

A balance exists between processes that promote nonspherical shapes (shearing, compressional flattening, and/or coalescence of bubbles) and those that promote spherical shapes (nucleation of new spherical bubbles and capillary forces that act to relax complex bubbles). In particular, it is necessary to weigh the timings of bubble nucleation, the cessation of bubble coalescence, and quenching of pyroclasts against the time scales of bubble relaxation and of residence in the shallow conduit (Moitra et al., 2013; Namiki and Manga, 2008). Vesicle shapes reflect the time available, prior to quenching, for bubbles to relax from complex shapes into spheres. Relaxation times are long in silicic melts but short in most basalt melts. Moitra et al., (2012) estimate that the characteristic relaxation time for bubbles in Hawaiian fountains is 10^{-2} to 10^{-3} s.

Moitra et al., (2013) used a parameter (1- Ω) to characterize vesicle shape, where Ω is the regularity, or degree of deviation from a perfect ellipse in 2D, and defined as:

$$\Omega = \frac{A}{\pi\lambda_l\lambda_s}$$

where A is the area of the vesicle, and λ_l and λ_s are respectively the semi-major and semi-minor axes of the best fit ellipse. For circles, Ω = 1. Moitra et al., (in press) show that Hawaiian clasts from the high fountain of Kīlauea Iki, 1959, have a population of near-spherical bubbles. Vesicles used in our VSDs were also analyzed for shape characteristics using regularity. ImageJ calculated the area of each vesicle as well as the length of the long and short axes of the best-fit ellipse. My approach differs from Moitra et al., (2013) in one respect: where Moitra et al. calculated bubbles' regularity on decoalesced binary images in only one magnification (100x), I calculate regularity values from decoalesced binary images for only those bubbles used in the VNDs, across all magnifications (scan, 25x, and 100x) in order to correlate the regularity to our VNDs and analyze the system as a whole.

4.4 Results

4.4.1 Deposit

4.4.1.1 Sample Characteristics

Episode 1 deposits form a series of agglutinated ramparts (Chapter 2), dominated by partially to intensely welded vesicular bombs and lapilli. A pocket of non-welded Ep 1P main-stage tephra from the peak of activity contains the most fluidal and glassy lapilli that I were able to sample in 2009/2010 from the 1969 eruption. A second Ep 1L sample was collected from scattered, partially outgassed spatter clasts tens of centimeters in diameter that accumulated as a discontinuous layer on top of the ramparts at the close of Ep 1. The Ep 9 deposit is dominated by highly uniform, extremely vesicular reticulite clasts ranging in size from small lapilli to 25 cm bombs. All remaining samples collected at this site above and below Ep 9 are dominated by pumice (Fig. 4.3). The smaller USGS samples from Ep 5, Ep 12, iEp 4/5, and iEp 5/6 are collections of fluidal black clasts with glassy microvesicular rinds, some containing pumiceous interiors. There is a complete absence of wall-rock clasts in the 1969 deposits I collected. Episodes 1 and 9 constitute the low and high fountain end members-respectively in our analysis.

4.4.1.2 Bulk density/vesicularity

The samples of the early and late ejecta from Ep 1 (Table 4.1, Fig. 4.4a–c) show similar, broad but well-defined density modes corresponding to 62% (main tephra) and 55% vesicularity (late stage spatter). In comparison, the Ep 9 reticulite defines a sharp mode at 96% (Fig. 4.4d–e) with a small tail of denser clasts between 87 and 65%. A suite of 5 regularly spaced samples (Fig. 4.3) between Ep 3 and Ep 9 (i.e., between May 25, 1969 and September 6, 1969) presumably covering episodes 3–8 shows a clear trend of decreasing overall modal vesicularity and a progression from unimodal to bimodal VSD. The lower three samples have unimodal vesicularities centered at 89% and the upper two have bimodal distributions with mode shifts to 71% and 65%. The equivalent suite of 10 samples (Fig. 4.3) above Ep 9, representing Eps 10–12, is all unimodal and shows progressive shifts towards lower vesicularity. In these samples, the lower three have vesicularity modes from 80 to 71%, the middle four from 59 to 55%, and the upper three from 62 to 69%.

4.4.2 Qualitative observations of microtextures

Significant textural diversity exists among the 11 clasts from this study (Fig. 4.5). Lapilli from the peak of the Ep 1 low fountaining have abundant, relatively small, spherical vesicles with rather thick glass walls. In comparison, late Ep 1 spatter pyroclasts contain numerous millimeter-sized bubbles (Fig. 4.6) with clear evidence of coalescence (Fig. 5A). The six images in Fig. 5B show bubble textures typical of iEp 4/5, Ep 5, and iEp 5/6, i.e., the transition into and out of an intermediate-height fountaining episode. Bubbles are smaller and number densities clearly higher (Fig. 6) in Ep 5 with respect to iEp 4/5 and iEp 5/6. Both Ep 5 samples, collected about 2 hr apart, contain numerous 50–300 μm bubbles. Such bubbles are nearly absent in the four samples from the inter-episodes, which are dominated by large, mostly round yet coalesced 0.8–2 mm vesicles (Fig. 6). Bubble walls in the inter-episode clasts are commensurately

Table 4.1 Bubble parameters highlighted by time period analyzed. Episode 5 and the inter-episodes are grouped together because they indicate a trend with time through an episode.

Episode	Clast #	Density	Phenocryst Corrected Density	Vesicularity	$N_{v\,tot}$	$N_v^{m}{}_{tot}$
		g/cm^3	g/cm^3	%	#/cm^3	#/cm^3
1	1t C05 (main tephra)	0.97	0.96	65	8.9 x 10^{05}	2.5 x 10^{06}
1	1s C29 (late spatter)	0.98	0.97	64	8.3 x 10^{04}	2.3 x 10^{05}
4/5[a]	45-1-2	0.70	0.69	76	5.8 x 10^{04}	1.1 x 10^{05}
5[a]	5-1-2	0.67	0.66	77	2.3 x 10^{05}	9.7 x 10^{05}
5[a]	5-2-2	0.63	0.62	78	5.2 x 10^{05}	2.4 x 10^{06}
5/6[a]	56-5-1	0.35	0.34	88	4.9 x 10^{03}	4.1 x 10^{04}
5/6[a]	56-5-2	0.32	0.31	89	1.3 x 10^{04}	1.2 x 10^{05}
9	6-11-18	0.03	0.03	98	1.7 x 10^{04}	1.7 x 10^{06}
12[a]	12-2-b1-4	0.33	0.36	88	5.6 x 10^{04}	4.6 x 10^{05}
12[ab]	12-2-b1-1 (rind)	0.35[c]	0.36[c]	67[d]	3.9 x 10^{04}	1.2 x 10^{05}
12[ab]	12-2-b1-1 (interior)	0.35[c]	0.32[c]	71[d]	6.8 x 10^{03}	2.3 x 10^{04}

a: USGS samples
b: sample is hetergeneous, therefor processed slightly differently
c: whole clast density and density corrections
d: image tree vesicularity for only the portion analysized (i.e. not whole clast vesicularity)

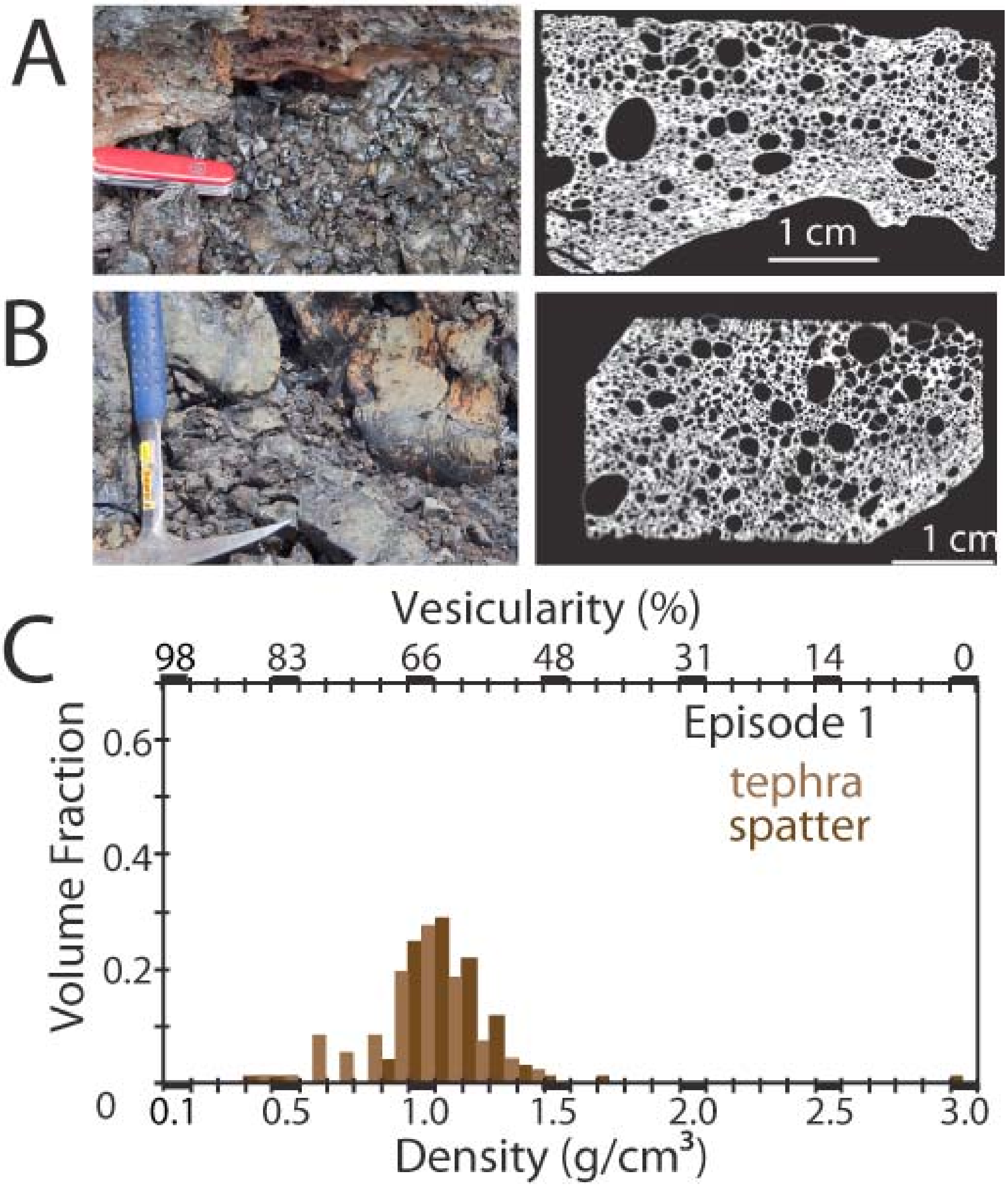

Figure 4.4 Density data for the Mauna Ulu units clearly identifiable in the field: Ep 1. Representative clast and corresponding thin section images for **A** pumice and **B** spatter. Field photos courtesy of David Dow, USGS. **C** Density histograms for Ep 1P (tephra) and Ep 1L (spatter), collected in 2009-2010 respectively.

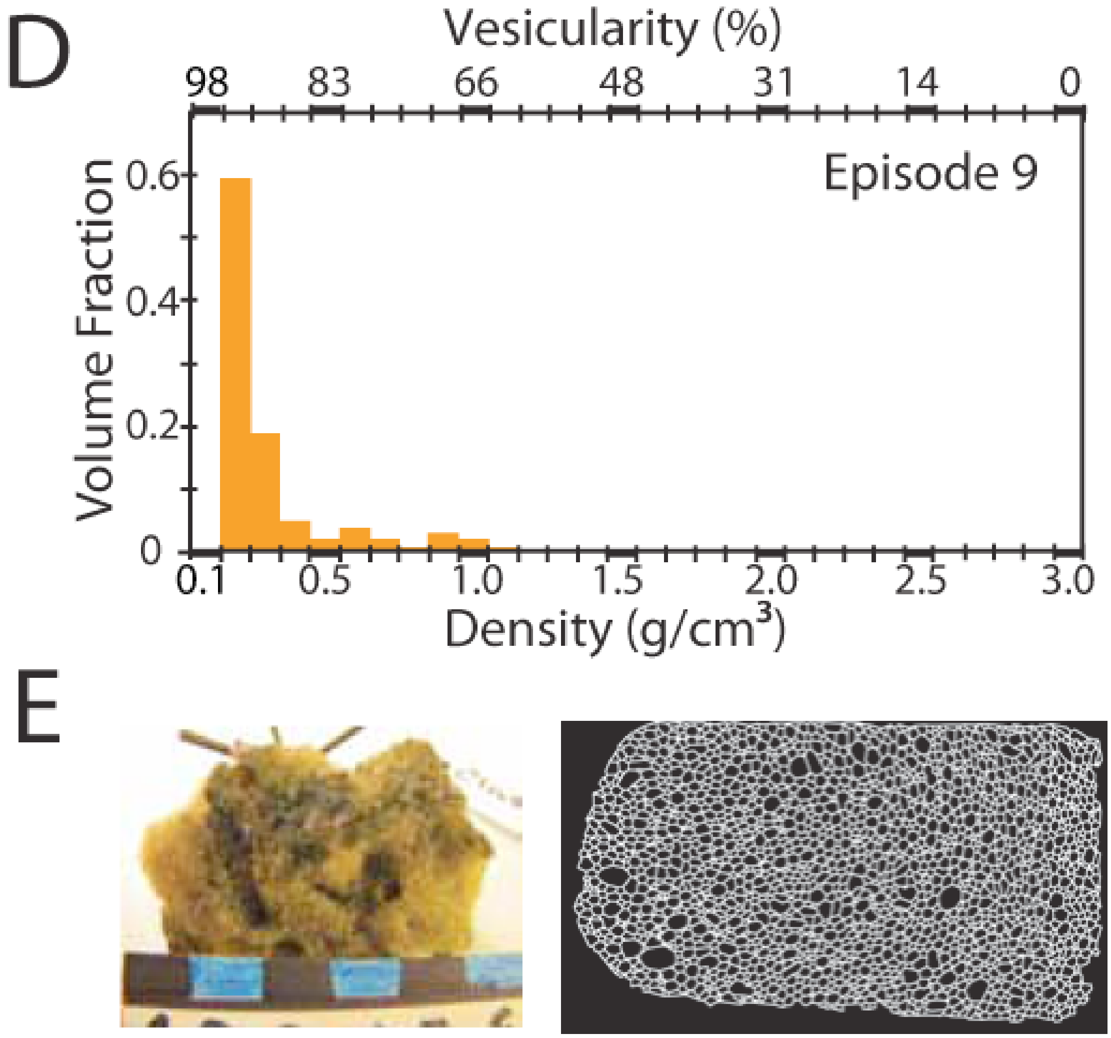

Figure 4.4 Density data for the Mauna Ulu units clearly identifiable in the field: Ep 9. **D** Density histogram for Ep 9 reticulite. **E** Select clast and corresponding thin section image of a representative reticulite clast.

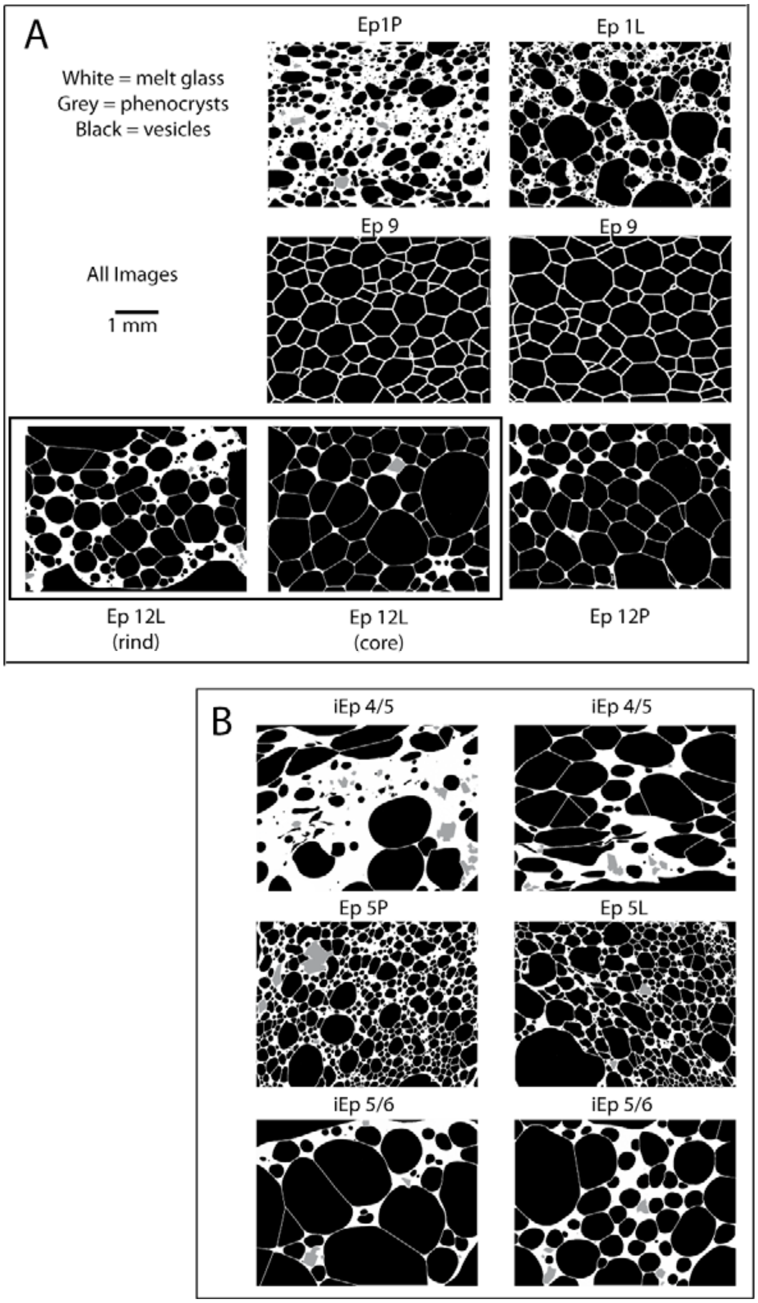

Figure 4.5 Scanning electron microscope images for all samples at 25x magnification. A and B are both at the same scale, which is noted in A only. **A**: individual episodes of activity in chronological order for Eps 1, 9, and 12. **B**: Ep 5, including samples just before (iEp 4/5) and after (iEp 5/6) the fountaining episode in chronological order showing textural changes through time.

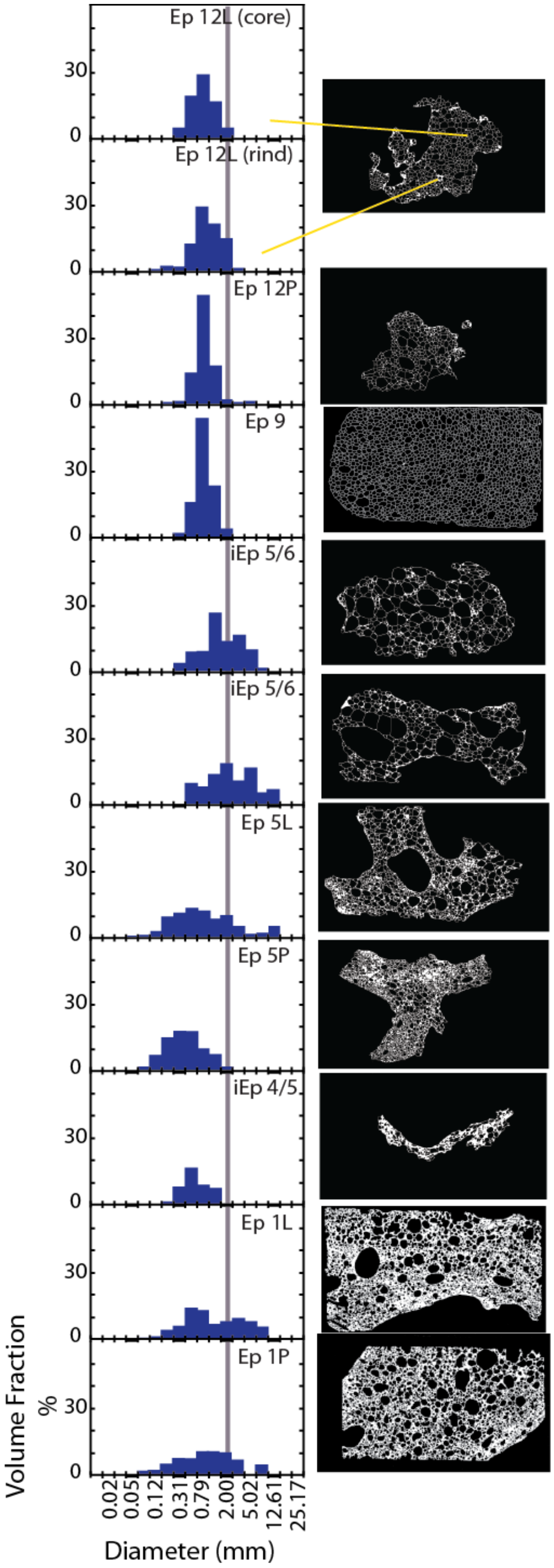

Figure 4.6 Histograms showing the volume fraction distribution of bubble diameters (mm) on the left and corresponding thin section scan images on the right. Data are in stratigraphic order, with the oldest sample (Ep 1P) at the bottom and the youngest sample (Ep 12L) at the top. The grey line denotes the 2 mm bubble diameter bin in each histogram.

thicker than those in the Ep 5 clasts. The Ep 9 reticulite has a texture unique among the Mauna Ulu clasts (Fig. 4.5a). Intermediate-sized bubbles, 0.5–1.0 mm (Fig 4.6), dominate the bubble population and are separated by exceptionally thin and straight septa and filaments. I show three Ep 12 images, two from one heterogeneous Ep 12 pumice (rim and core respectively) and a third image from a more homogeneous pumice. Clast 12P and the interior of clast 12L have in common abundant large bubbles similar to the inter-episode clasts but with more complex shapes and significantly thinner vesicle walls. The clast 12L rim has a greater abundance of smaller bubbles and thicker glass walls.

4.4.3 Quantitative microtexture observations

4.4.3.1 Vesicle number densities

The uncorrected VND range from 5×10^3 to 9×10^3 bubbles cm^{-3} (Table 4.1). Applying the melt correction from Klug et al. (2002) broadens the range from 2.3×10^4 to 2×10^6 bubbles cm^{-3}. The highest number densities are preserved in the products of the initial (Ep 1P) and highest (Ep 9) fountaining episodes, on opposite ends of the Hawaiian-style eruption spectrum. Episode 1 main tephra has an order of magnitude more bubbles than the late stage Ep 1L spatter. I see a similar trend between Ep 5 tephra and the bracketing inter-episode tephra. In addition, the earlier erupted Ep 5P clast has a significantly higher bubble number density than the clast collected during waning activity. Intermediate fountain heights (Ep 5P, Ep 12P) have similar VNDs to each other and are between those of Ep 1 and Ep 9. The interior of the heterogeneous Ep 12 clast has an order of magnitude lower number density than the rind.

4.4.3.2 Vesicle size distributions

A wide range of VSD is present, with the extremes represented by the strongly unimodal reticulite of Ep 9 and the broadly bimodal size distribution of Ep 1L (Fig. 4.6). Clast Ep 1P has the broadest range in vesicle sizes and the highest abundance of <250 μm bubbles. Clast Ep 1L is broadly bimodal, with peaks at 500 μm and 3 mm, which makes it distinct among the samples (Fig. 4.6). The sizes of bubbles range widely in the two clasts from Ep 5 and iEp 4/5, but clast 5L is markedly coarser and has a distinct secondary peak at 1 cm. The largest vesicles are seen in the inter-episode samples, iEp 4/5 and iEp 5/6. The iEp 4/5 clast is the only one to show marked bubble flattening on some bubbles, thus the VSD should be interpreted with caution. Intra-episode 5/6 tephra shows the coarsest VSDs among the 11 samples (Fig. 4.6). Both samples are weakly bimodal, with primary peaks at 1–2 mm and secondary peaks at 3–5 mm. Bubble sizes in the Ep 9 reticulite span a narrow range (50 μm–2 mm) with the mode at 80 μm. The Ep 12 scoria also has a narrow range, with a mode of 80 μm, but spans a slightly wider range in vesicle sizes from 30 μm to 5 mm (Fig. 4.6). Unimodal distributions are primarily associated with the higher fountains of the later episodes.

4.4.3.3 Vesicle shape data

Vesicle shapes consists of near circular bubbles with $(1-\Omega)$ values of 10^{-8} to 10^{-9} (as compared to 10^{-5} for the Kīlauea Iki clast in Moitra et al., [2013]). The only deviations from circular vesicles in 2D are small, flattened bubbles either immediately adjacent to large spherical bubbles or on the margins of spatter.

4.5. Interpretation

4.5.1 Vesicle shape data

Short relaxation times allow bubbles to relax rapidly back to spherical shapes in Hawaiian eruptions (Moitra et al., 2013). I conclude from our pyroclasts that preservation of complex and coalesced shapes (low regularity values) therefore requires that coalescence is ongoing at the time of melt quenching. Complexly shaped vesicles though, are a minority in the vesicle population of our pyroclasts.

4.5.2 Vesicle number densities (VND)

Vesicle number densities in magmas mostly come from more silicic systems, with Cashman and Mangan (1994) and Stovall et al., (2011, 2012) quantifying the mafic end member. The VND of silicic melts scale with the degree of volatile supersaturation at nucleation (Toramaru, 1995; Mangan et al., 1993; Mangan and Cashman 1996). Time scales for volatile diffusion greatly exceed the time scales of decompression, and so regions of melt remote from early formed vesicles remain supersaturated and continue to nucleate bubbles throughout shallow conduit ascent (Gonnermann and Houghton, 2012).

Number densities for silicic melts can reveal (1) the rate of magma ascent in the top 300–400 m of the conduit, and (2) the relative time scales of bubble nucleation and bubble coalescence. In Hawaiian pyroclasts, however, they are harder to interpret, as they reflect competing influences of bubble nucleation (promoting high number densities) and coalescence (reducing number density) that are less restricted by melt viscosity than in more silicic melts. In essence, to understand magma dynamics in the shallow conduit, and its relationship to eruption rate, I must deconvolute the influence of (2) from (1).

Magma residence time in the conduit controls post-nucleation bubble growth and coalescence. Long residence times (tens of seconds) favor coalescence and shorter residence times (seconds) favor growth (Mangan et al., 1993) where thermally insulted clast interiors show a lengthened time scale of bubble growth/coalescence compared quenched rims (Stovall et al., 2011, 2012). There is direct evidence for both processes at Mauna Ulu. The former was most discernible in Ep 1 and the latter during the higher fountaining episodes. Chapter 2 noted that lava stage levels for Ep 1 were up to 3 m deep above the vents for 0.4–2 hr when supply rate equaled the rate of dynamic lava drainage away from the fissure system, thus the bubble residence time is slightly greater. Stovall et al (2011) estimate the residence time of pyroclasts in moderately high fountains to be of the order of 8 s. This suggests that slowed rise promotes bubbles' interactions during surface or near-surface backlog of magma and may have a more profound influence on the vesicularity of some Mauna Ulu pyroclasts than bubble dynamic expansion and coalescence in the fountain. To examine these competing processes, I used a ratio of the volume of gas to the volume of melt ($V_g/V_{m)}$ versus N_v^m plot (Fig. 4.7) to interpret bubble growth processes and correlate that data with observations of residence time. The V_g/V_m ratio is largely independent of N_v^m because of the negligible volume of even large numbers of very small bubbles; the ratio scales with free growth and coalescence. Free growth without continued nucleation (or bubble collapse and outgassing without coalescence) produces increased V_g/V_m at constant N_v^m. Coalescence or nucleation without expansion or bubble collapse and outgassing produces a change in N_v^m, at steady V_g/V_m.

In Fig. 4.7, Ep 1, Ep 5, and iEp 5/6 clasts show the latter trend of significant variations in N_v^m, with little change in V_g/V_m. This suggests bubble growth was negligible and the populations, as preserved, evolved by coalescence alone. Episode 9 has a trend marked as growth (upwards) even though I only have 1 sample because of the textural implications of its formation: rapid growth of recently nucleated bubbles. The Ep 12 rim and core clast is more similar to the data of Stovall et al. (2011, 2012), reflecting on-going bubble expansion in the fountain after fragmentation in the fountain. I interpret the progression of iEp 4/5, Ep 5, and iEp 5/6 to show a physical record of the influx of gas that triggered a fountaining episode.

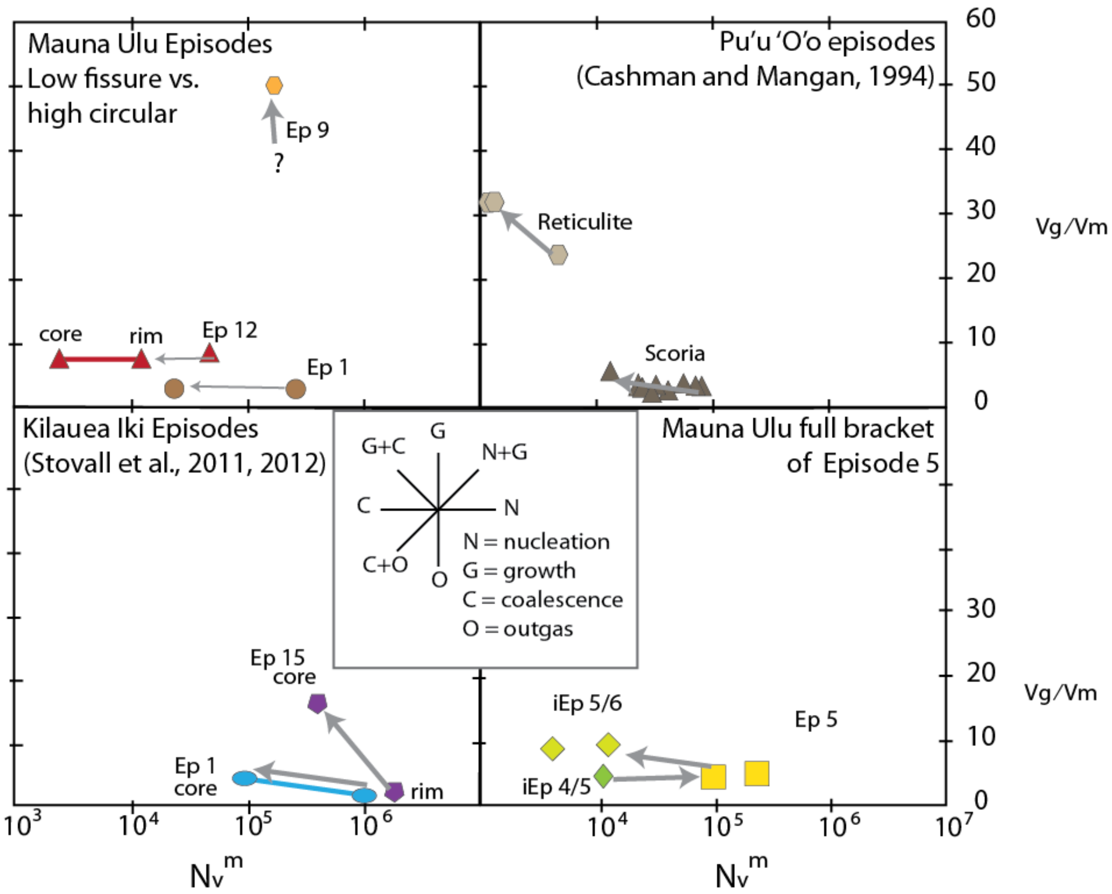

Figure 4.7 Four plots of the melt-corrected number densities verses melt ratio. A key in the center of the lower plots shows theoretical and observational trends for interpreting relative dominance of bubble nucleation, growth, coalescence, and outgassing, and what bubble-trend directions typically mean. Gray arrows on the plots indicate direction of trend that can be interpreted from the key. In the top left plot, data for individual episodes from Fig. 4.5a are shown (Ep 1 = brown circles, Ep 9 = orange hexagons, Ep 12 = red triangles). In the bottom right are the samples shown in Fig. 4.5b (iEp 4/5 = dark green diamonds, Ep 5 = yellow squares, iEp 5/6 = light green diamonds). Similar data, for comparison, are plotted in the lower left for Kīlauea Iki (Ep 1 = blue ovals, Ep 16 = purple pentagons, Stovall et al., 2011), and in the upper right for Pu‘u ‘Ō‘ō (grey hexagons = scoria, tan triangles = reticulite, Cashman and Mangan, 1994). For Mauna Ulu Ep 12 and Kīlauea Iki Ep 1, clasts that have both analyzed rims and cores are denoted with a solid connector line and labeled rim and core as appropriate.

4.5.3 Vesicle size and volume distribution

Clasts from periods of moderate and high fountaining (Eps 5, 9, 12) have narrower ranges of vesicle size and smaller mean diameters (Fig.4.6) than those from low fountaining (Ep 1) and the inter-episodes, are also bimodal. I relate this directly to the relative time spent in the vent and very shallow conduit. During moderate to high fountaining, this residence time was on the order of seconds and bubble growth after nucleation was thus limited. During low fountaining, and especially in the inter-episodes, a slightly longer residence time due to slower ascent allowed for increased bubble growth and coalescence, which continued after nucleation ceased but prior to fragmentation. This is seen by noting the absence of the smallest bubbles in the iEp 5–6 clasts compared to the two Ep 5 clasts (Fig. 4.5, 4.6). The effect of further growth and coalescence of bubbles after fragmentation, i.e., in the fountain, is seen in the two images from pyroclast Ep 12L (Fig. 4.5, 4.6). This is less dramatic than that observed in the Kīlauea Iki 1959 fountains (Stovall et al., 2011, 2012). Bubble sizes (Fig. 4.6) in the Ep 9 reticulite span a narrow range (50 µm–2 mm) that is larger than theoretical critical radii of 1.7–17 µm (depending on the density of homogeneous nucleation) for newly nucleated bubbles (Gonnerman and Manga, 2007). This suggests that, during Ep 9, nucleation was intense but short-lived, and bubble growth continued prior to quenching of the pyroclasts, presumably in the high fountain.

4.6. Discussion

4.6.1 Correlating fountain heights with bubble nucleation, growth, and coalescence

Each of the twelve fountaining episodes from the 1969 Mauna Ulu eruption was driven by the arrival of a fresh pulse of magma into the east rift zone (Swanson et al., 1979), and was accompanied by a new onset of bubble nucleation. Both the fountain heights and mass discharge rates attained in each episode appear to be a function of contrasting rates and timings of bubble nucleation, growth, and coalescence (Table 4.2). Ep 9 was the only fountain to reach heights over 500 m, and Fig. 4.2 shows that the largest drop in summit tilt took place during Ep 9. The extreme vesicularities in the Ep 9 sample match those found by Mangan and Cashman (1996) at Puʻu ʻŌʻō. The reticulite has a slightly lower VND than that of the Ep 5 pyroclasts. However the narrow VSD of Ep 9 strongly suggests a short time window for bubble nucleation. I postulate that Ep 9 records the most rapid transfer of new magma from the summit reservoir with respect to the rest of the eruption because of the large summit tilt changes, high VND, and very narrow VSD. A short interval of rapid bubble nucleation would leave the system ripe for rapid buoyant ascent in the shallow conduit accompanying bubble nucleation and growth, followed by subsequent reticulite formation in the fountain. After rapid nucleation, ascent time must have been short during which bubbles grew to a size dominated by 80 μm diameters, which involved maximally packing bubbles without significant coalescence or nucleation of new bubbles. I only have 1 sample from Ep 9, but its position on Fig. 4.7 suggests rapid growth of all bubbles, with minimal coalescence relative

Table 4.2 Summary of interpretations of vesiculation processes based on microtextural evidence..

Ep	Description	V_g / V_m	N_v^m	Eq. D. Mode (mm)	Median Regularity	Interpretation
1P	fissure-fed, < 50-m high, peak	2.9	2.5×10^6	0.79	3×10^{-11}	Peak discharge of early volatile-rich melt, from extended source
1L	fissure-fed, < 50-m high, waning	2.9	2.3×10^5	0.50	2×10^{-10}	Waning discharge through ponded lava, increased outgassing
iEP 4/5	gas pistoning and spattering	4.1	1.1×10^5	0.50	5×10^{-9}	Ponding of magma, extensive outgassing before ejection
5P	375-m fountain (2 vents), peak	4.2	9.7×10^5	0.50	4×10^{-9}	Rapic nucleation overprinted by growth and minor coalescence
5L	375-m fountain (2 vents), waning	4.5	2.4×10^6	0.32	2×10^{-9}	Waning discharge through ponded lava, increased coalescence and outgassing
iEp 5/6	gas pistoning and spattering	8.2	4.1×10^4	2.00	2×10^{-11}	Ponding of magma, extensive outgassing before ejection
iEp 5/6	gas pistoning and spattering	9.0	1.2×10^5	1.26	4×10^{-9}	Ponding of magma, extensive outgassing before ejection
9	540 m fountain, single vent	50	1.7×10^6	0.79	6×10^{-10}	Short-lived nucleation, rapid growth, short residence time in shallow conduit and vent
12P	final episode, 390-m fountain, 2 then 1 vent	8.7	4.6×10^5	0.79	1×10^{-9}	Continued vesiculation within pyroclasts in the fountain
12Lc	final episode, 390-m fountain, 2 then 1 vent	7.8	1.2×10^5	0.79	1×10^{-9}	Continued vesiculation within core of pyroclast in the fountain
12Lr	final episode, 390-m fountain, 2 then 1 vent	7.8	2.3×10^5	0.79	2×10^{-9}	Quenched rim of pyroclast which continued to vesiculate in the fountain

to all other episodes. Finally, vent geometry probably played an important role: Ep 9 erupted from a simple, single, sub-circular vent, as opposed to other episodes, when two coeval vents or a fissure system were active.

Episodes 5 and 12 were fountains of similar intermediate height and intensity. Episode 12 clasts are surprisingly uniform and resemble the Ep 9 reticulite in terms of VSD and circularity parameters. The Ep 12P clast, as well as the rind-interior nests of clast 12L (done in the style of Stovall et al., 2011), have VSD/VVD data that suggest late coalescence in the fountain is the driving factor for the slightly coarser VSD (Fig. 4.6).

The Ep 1P clast has a high VND, given that this episode was marked by only low fountaining, driven by a large number of small bubbles that might otherwise be interpreted to reflect high rates of shallow ascent of magma. I interpret the high VND to be a consequence of the eruption initiation, when fresh, undegassed magma reached the free surface for the first time.

4.6.2 Contrasts between peak-fountaining, waning fountaining and intra-episodes

Vesicle size, number density, and shape clearly change in Ep 1 between the main stage tephra and late stage spatter. I see an evolution of the bubble population to larger sizes during Ep 1, which I attribute to an extended opportunity for coalescence of the bubbles after cessation of nucleation (Fig. 4.6). In other words, the presence of accumulated lava above the vent (Chapter 2) allowed the bubble residence time in the magma to be extended by a few seconds, influencing the textures preserved in the pyroclasts. Episode 5, which had samples collected approximately 1.75 hr apart, shows a similar trend to Ep 1 whereby Ep 5L, collected later in time, has a coarser bubble population driven by more extensive coalescence, much like Ep 1L. Inter-episode bubble populations are typically coarser and have the lowest VNDs recorded at Mauna Ulu. The iEp5/6 pyroclasts clearly reflect an interval of slowed magma ascent in the vent after Ep 5, cessation of bubble nucleation and growth, and extended coalescence, with prolonged opportunity for relaxation of coalesced bubbles. The iEp 4/5 clasts have flattened and/or sheared small bubbles deformed during free growth of the largest bubbles, and I infer that time was insufficient in the pyroclast's history to allow the melt to relax around the bubbles. Plotting both the inter-episode and Ep 5 data on the V_g/V_m versus N_v^m plot (Fig. 4.7.), I deduce that magma ascent was slower and bubble residence time in the conduit was longer before and after the main fountaining, providing extended time for both free growth of individual bubbles and moderate degrees of coalescence.

4.6.3 Comparisons to other eruptions

Few data exist for other Hawaiian-style fountaining deposits, but the limited information reveals two striking contrasts between Mauna Ulu 1969 and Kīlauea Iki 1959 (Stovall et al., 2011, 2012) pyroclasts. First, irrespective of mass eruption rate, the Mauna Ulu pyroclasts always have bubble number densities that are one to two orders of magnitude less than their Kīlauea Iki counterparts. A further contrast lies in the duration and spacing of episodes in the two eruptions. Kīlauea Iki episodes, particularly after Ep 4, are markedly shorter and very closely spaced with respect to Mauna Ulu. Both contrasts can perhaps be linked to a greater role of carbon dioxide (CO_2) gas evolved at depth in promoting buoyant magma ascent in the Kīlauea Iki summit eruption with respect to the Mauna Ulu rift zone eruption.

4.6.4 Vesiculation histories and textural maturation

Quenching, either upon fragmentation, or during subsequent cooling in the fountain, may interrupt the pattern of vesiculation and vesicle evolution at different points, leading to diversity in vesicle number and size in pyroclasts from any one fountain. I see three patterns of bubble maturation in the Mauna Ulu pyroclasts (Table 2). First, between episodes, the magma is confined to the vent and subsurface plumbing, offering an extended time for rising decoupled bubbles to grow and coalesce before erupting as spatter and becoming incorporated into the deposit. The time scale for this process (spattering and gas pistoning) was typically hours to days (Swanson et al., 1979). Second, during fountain activity, magma ascent is more rapid, and the bubble residence time in the shallow conduit and vent is much shorter (seconds to tens of seconds, Stovall, et al., 2011, 2012), which yields less opportunity for bubbles to grow, coalesce, and relax back to a spherical shape. Rims and cores of larger pyroclasts from moderate to high fountains preserve a record of on-going vesicle maturation of thermally insulated pyroclasts during transport in the fountain after fragmentation. Under insulated conditions, bubbles evolve more dynamically with continued growth of bubbles and coalescence. A third vesiculation path was followed by the reticulite, which formed in a short-lived and exceptionally high fountain. It underwent late, short-lived bubble nucleation followed by rapid growth of a uniform bubble population. Growth was likely terminated by instantaneous quenching at the onset of permeability before significant coalescence had begun.

4.7. Conclusion

Patterns of shallow degassing and outgassing determined both the form and duration of fountaining episodes at Mauna Ulu. The timing and depth of 1) bubble nucleation, 2) diffusive and expansive growth, and 3) coalescence all varied significantly. The extremes show high absolute vesicularities, reflecting either very rapid bubble nucleation and free growth (e.g., Ep 9) or an extended opportunity for bubbles to grow and coalesce (inter-episodes). In the latter case, absolute vesicularities are driven by relatively small numbers of the largest bubbles, leading to higher vesicularity. The highest vesicle number densities were attained early in the eruption (Ep 1), but the wide size spectrum suggests that this reflected a prolonged period of nucleation. The degassing processes and ascent rates fed back on each other to emphasize these contrasts.

Chapter 5

Conclusions

5.1 Limitations on Current research

5.1.1 Chapter 2

Data acquisition at the time of the Mauna Ulu eruption was difficult, as there was no easy access to the fissure from the north side of the northern ramparts, especially while the eruption was ongoing. The observations made and photographs taken at the time were critical for this research, but there was relatively little to build from, and thus I had to change our research plan to address questions that I previously thought had been answered. Prior studies of Ep 1 at Mauna Ulu had only ~ 7 paragraphs of text across 3 publications, ~25 photographs, and no video. The rest of the Mauna Ulu fountain episodes and years of overflows, gas pistoning, and lava flow/tube formation were indeed well documented.

5.1.2 Chapter 3

Vent and shallow conduit quantification seemed ripe for use in a modeling approach of how fissure shape affects fountain behavior and rampart distribution. However, the mathematics and fluid dynamics involved were too dependent on parameters requiring extensive lab testing to determine empirical coefficients to be solved in the time of this dissertation. I was unable, using existing code, to address two basic questions: 1) how does vent flare influence fountain height, rampart geometry, and fountain location, and 2) how does sinuosity and irregularity modify fountain behavior, if at all?

The former could not be addressed as our fissure vents are the engineering equivalent to diffusers, and diffusers of different geometries or the same geometry have different empirically-derived coefficients in the fluid dynamical equations. Furthermore, for any given diffuser shape, there will be different empirical coefficients for different fluids that pass through it (i.e., air in ducts versus water in pipes versus magma in rock). Each vent would require an exact specification of its complex shape (and I only have LiDAR data for three vents) and would need a scale model in a laboratory through which analog magma would have to be fluxed in order to determine the empirical constant. This was not feasible in the course of the dissertation.

The latter question could not be addressed as the engineering literature deals extensively with pipe roughness that is <10% of the pipe's diameter (translated into terms of our fissure: the equations can handle irregularities on the fissure walls that are <10% of the fissure width). My measured values of irregularity are typically 40–60% the measured fissure width. To achieve a model that can handle irregularities on the order of ~50% fissure width, I would need individual equations to calculate the flow perturbations for *each* irregularity, which suddenly makes the mathematical problem significantly harder and more time consuming. Again, pursuing this approach was beyond the scope of this paper.

5.1.3 Chapter 4

The locations of our sampled tephra pits with respect to Mauna Ulu were not ideal, as lava flows buried the proximal cone and most of the medial deposit. The literature indicates that Eps 3–12 should have deposited material in our best sample location, 1.5 km SW of the vent area; however, only Ep 9 was distinguishable. Our data and interpretations on vesiculation processes would have been inhibited if I had not had access to USGS samples from more proximal locations, but these samples contained very few clasts.

Vesicle number densities and microtextural studies do not capture bubble populations in excess of 2–3 cm diameter. Broken spatter from Ep 1, as observed in the field, can have up to 12 cm vesicles. Photos during the eruption would indicate that the largest bubbles completely burst during eruptive activity. These largest bubbles could be on the order of 50 cm or more but leave no physical evidence of existence except in the photos.

5.2 Enhancement of current research

This research was significantly aided in three ways. First, the documentation that was available, including aerial photos from Sandia Labs, for the Ep 1 fissure eruption provided a way for the relative chronology to be constrained in absolute time and to validate the relative timings derived from field relationships and lava crust thicknesses. Second, our conceptual understanding of fountain fluid dynamics and eruptive behaviors, especially as fountains initiate activity, was augmented by USGS eruption videos from the March 5–9, 2011 Kamoamoa eruption of Kīlauea. I had not previously understood that lava could accumulate to significant depths more or less on top of the vent (moving at first very slowly away). I were also intrigued and stimulated by the observation that fragmentation can take place at the lava surface, which was often tens of centimeters *above* the surrounding ground surface. This is in contrast to all previous conceptual models of fountain fragmentation in which the fragmenting occurs *at* or *below* the ground surface. Third, the vesiculation studies were greatly aided by the archived USGS tephra samples, which were directly linked with specific fountains and absolute time.

5.3 Ideas for future work

Naturally, during the course of this research, many specific questions as well as broad topics materialized that could not be addressed in the course of this dissertation. These include:

- Expanding quantitative geometrical measurements with depth (and distance?) along the fissure.
- Constraining missing parameters (i.e., vent shapes/widths, etc.) from other previously well documented fissure eruptions, where possible, to expand the global database on fissures.
- Using real fissure geometries in fluid dynamical computer models instead of assuming simplistic conduit shapes.
- Understanding possible implications for fluid dynamics of shallow (<1 km) dike emplacement or dike margins?

    - Do sub-surface irregularities (i.e., irregularities in the dike before it reaches the surface), if present, influence flow of magma, or how the dike propogates forward? If so, how?
- Expanding microtextural studies to include other Mauna Ulu episodes, and episodes at Puʻu ʻŌʻō, so that, when coupled with Kīlauea Iki data, there will be a truly encompassing database of variability in Hawaiian fountains (single, paired, and multiple sources, as well as 100 and 200 m high fountains which at present are a hole in the dataset) as seen on Kīlauea.
    - Data could further be grouped with existing and new Etna and/or Izu-Oshima data to construct a more comprehensive database on fountain variabilities and what drives them.
- Further constraining volatile chemistry in melt inclusions and matrix glasses for fissure fountains.
- Determining how much of the volatile content goes into low fountains versus high fountains.
- Correlating vesicle textures with distance along a fissure.
    - Does cooling magma, which stagnates out along the fissure (at irregularities) help to localize vents, possess distinctive vesicle textures?
    - Can different rates of degassing and outgassing along the fissure length be seen in vesicle textures?
- Determining the best response to the next Hawaiian fountaining eruption (low or high).

- What measurements (fountain heights, tephra thickness, etc.), samplings (density, grainsize, componentry, chemistry, etc.), and observations (lava fountain interactions, rampart/cone collapses, pulsatory behavior, etc.) should be made?
- What sampling and observational frequencies are optimal?

Pursuing any or all of these further in future research could provide a deeper understanding of both fissure systems and basaltic systems. The results of such research would have broad reaching implications for volcanology.

5.4 Summary and contributions to physical volcanology

Fissure eruptions of basalt are the most common eruption style on Earth, including the sea floor, yet the least well studied. This research produced new detailed quantitative studies for three key aspects of fissure systems at Kilauea: 1) the geometry of the shallow conduit and its transition to the vent, 2) vesiculation and fragmentation mechanisms for low fissure-fed versus high cylindrical-sourced Hawaiian fountains, and 3) and the dynamic interplay between spatter accumulation and the generation of lava in the proximal setting. The analyses provide a foundation for understanding eruption dynamics, from shallow magmatic ascent to solidified eruptive products, for fissure-fed Hawaiian fountains.

Typically, vents in a fissure system become obscured by drainback, hidden under rampart talus, or are buried by lava. The Mauna Ulu fissure, being exposed to depths of tens of meters, has provided an exceptional opportunity to understand the geometry of a primary magmatic fissure pathway. This is the first step toward understanding shallow conduit geometry beyond simple, straight-walled, rectilinear, or cylindrical shapes. Constraining magmatic pathway geometries was recognized at the 2012 American Geophysical Union (AGU) Chapman conference on Hawaiian volcanism to be one of the key questions that needs to be addressed in future research on basaltic volcanoes. Expanding this knowledge, while difficult, has broad implications for data interpretation in many subdisciplines beyond physical volcanology, including seismology, infrasound, petrology, and geodesy.

Vesicularity studies have been made on products of all eruption styles, but only a few pertain to Hawaiian-style fountaining, and those studies all focus on intermediate and high fountains (>200 m). Hawaiian fountaining activity, however, is quite diverse, with widely varying mass eruption rates and source geometries. This dissertation research presents microtextural and vesicle data for the other end-member of Hawaiian-style fountain eruptions by addressing low fountains from a fissure source. Particularly important is the analysis of tephra from main-stage/peak fountaining, as it provides a first look at the early vesiculation of fissure fountains. While more studies could be done on products of fountains 50–200 m in height, this research provides an end-member to bracket more typical variations in Hawaiian fountain behavior.

Tephra deposits from Hawaiian fountains, whether purely ballistic or slightly to moderately wind advected, have interwoven relationships with coeval lava flows. While this has been commonly observed and qualitatively noted at many volcanoes, this dissertation presents quantitative data for these interactions, and I were able to back out a chronology of those interactions. Eyewitness accounts of the eruption provided a rudimentary timeline, which our calculations of rates and timings, based on deposits, confirmed and clarified. Using similar approaches at other fissure eruptions, especially those that were undocumented, could create an abundance of data on fissure fountain behavior and activity. Focusing first on documented fissure eruptions would add rigor to our methodologies and the models derived from it.

References

Allard, P., Behncke, B., D'Amico, S., Neri, M., Gambino, S., 2006. Mount Etna 1993–2005: Anatomy of an evolving eruptive cycle. Earth Sci. Rev., 78(1–2):85–114

Alparone, S., Andronico, D., Lodato, L., Sgroi, T., 2003. Relationship between tremor and volcanic activity during the Southeast Crater eruption on Mount Etna in early 2000. J. Geophys. Res., 108(B5):2241– 2245, doi:10.1029/2002JB001866

Anderson, A.T., Brown, G.G., 1993. CO_2 contents and formation pressures of some Kilauean melt inclusions, Am. Mineral., 78:794–803

Aramaki, S., Utsu, T., Watanabe, H., Ida, Y., Yukutake, T., Notsu, K., Shimozuru, D., 1988. In: S Aramaki (Ed.), The 1986–1987 eruption of Izu-Oshima volcano. Earthquake Research Institute: University of Tokyo; pp 1–61

Aydin, A., DeGraff, J.M., 1988.Evolution of polydonal fracture patterns in lava flows. Science, 239:471–4476

Behncke, B., Neri, M., 2003. The July–August 2001 eruption of Mt. Etna Sicily. Bull Volcanol 65(7):461–476

Bonaccorso, A., Bonforte, A., Calvari, S., Del Negro, C., Di Grazia, G., Ganci, G., Neri, M., Vicari, A., Boschi, E., 2011. The initial phases of the 2008–2009 Mt. Etna eruption: a multi-disciplinary approach for hazard assessment. J. Geophys. Res., 116:B03203, doi:10.1029/2010JB007906

Bower, S.M., Woods, A.W., 1998. On the influence of magma chambers in controlling the evolution of explosive volcanic eruptions. J. Volcanol. Geotherm. Res., 86(1–4):67–78, doi:10.1016/S0377-0273(98)00081-X

Bruce, P.M., Huppert, H.E.,1989. Solidification and melting along dykes by the laminar flow of basaltic magma. In Ryan, M.P., (Ed.) Magma Transport and Storage. Wiley, New York, pp 87–101

Burton, M., Allard, P., Mure, F., La Spina, A., 2007. Magmatic gas composition reveals the source depth of slug-driven Strombolian explosive activity. Science, 317(5835):227–230

Caricchi, L., Burlini, L., Ulmer, P., Gerya, T., Vassalli, M., Papale, P. 2007. Non-Newtonian rheology of crystal-bearing magma and implications for magma ascent dynamics. Earth Planet. Sci. Lett., 264:402–419

Cashman, K.V., Mangan, M.T., 1994. Physical aspects of magmatic degassing II. Constraints on vesiculation processes from textural studies of eruption products. In: In: Carroll, M.R., Holloway, J.R., (Eds.), Volatiles In Magmas. Rev. Mineral., Mineral. Soc. Am., 31:447–478

Cayol, V., Cornet, F.H., 1997. 3D Mixed boundary element for elastostatic deformation field analysis. Int. J. Rock. Mech. Min. Sci., 34(2):275–287

Costantini, C., Bonadonna, C., Houghton, B.F., Wehrmann, H., 2009. New physical characterization of the Fontana Lapilli basaltic Plinian eruption, Nicaragua. Bull. Volcan., 71:337–355

Costantini, L., Houghton, B.F., Bonadonna, C., 2010. Constraints on eruption dynamics of basaltic explosive activity derived from chemical and microtextural study: the example of Fontana Lapilli Plinian eruption, Nicaragua. J. Volcan. Geotherm. Res., 189:207–224

Dance, M., Hancock, P.L., Sparks, R.S.J., Wallman, A., 2001. Fracture and surface crust development in a Holocene pahoehoe lava flow on the island of Tenerife, Canaries. J. Structural. Geol., 23:165–182

Daniels, K.A., Kavanagh, J.L., Menand, T., Sparks, S. 2012. The shapes of dikes: Evidence for the influence of cooling and inelastic deformation. Geol. Soc. Am. Bull., 124(7–8):1102–1112. Doi:10.1130/B30537.1

Day, S.J., Carracedo, J.C., Guillou, H., Gravestock, P., 1999. Recent structural evolution of the Cumbre Vieja Volcano, La Palma, Canary Islands: volcanic rift zone reconfiguration as a precursor to volcano flank instability?. J. Volcanol. Geotherm. Res., 94:135–167

Decker, R.W., 1987. Dynamics of Hawaiian Volcanoes: an overview. In: Decker, R.W., Wright, T.L., Stauffer, P.H. (Eds): Volcanism in Hawaii, US Geol. Surv. Prof. Pap. 1350(2):997–1018

DeGraff, J.M., Aydin, A., 1987. Surface Morphology of columnar joints and its significance to mechanics and direction of joint growth. Geol. Soc. Am. 99:605–617

Del Carlo, P., Pompilio, M., 2004. The relationship between volatile content and the eruptive style of basaltic magma: the Etna case. Annals of Geophys. 47:1423–1432

Delaney, P.T., Pollard, D.D., 1981. Deformation of host rocks and flow of magma during growth of minnette dikes and breccias-bearing intrusions near Ship Rock, New Mexico. U.S. Geol. Surv. Prof. Pap. 1202:1–61

Delaney, P.T., Pollard, D.D., 1982. Solidification of basaltic magma during flow in a dike. Am. J. Sci., 282:85–885

Delaney, P.T., Pollard, D.D., Ziony, J.I., McKee, E.H., 1986. Field relations between dikes and joints: emplacement processes and paleo stress analysis. J. Gephoys. Res., 91(B5):4920–4938

Dingwell, D.B., 1996. Volcanic dilemma: flow or blow?. Science, 273(5278):1054–1055, doi: 10.1126/science.273.5278.1054

Dixon, J.E., 1997. Degassing of alkalic basalts. Am. Mineral., 82:368– 378

Dixon, J.E., Stolper, E.M., Holloway, J.R., 1995. An Experimental Study of Water and Carbon Dioxide Solubilities in Mid-Ocean Ridge Basaltic Liquids. Part I: Calibration and Solubility Models. J. Petrol., 36(6):1607–1631

Duffield, W., 1972. A Naturally Occuring Model of Global Plate Tectonics. J. Geophys. Res., 77(14):2543–2555

Dzurisin, D., Koyanagi, R.Y., English, T.T., 1984. Magma supply and storage at Kīlauea volcano, Hawaii, 1956–1983. J. Volcanol. Geotherm. Res., 21(3–4):177–206

Eaton, J.P., Murata, K.T., 1960. How Volcanoes Grow. Science. 132(3432):925–938

Ebinger, C.J., Casey, M., 2001. Continental Breakup in Magmatic Provinces: An Ethiopian Example. Geology, 29:527–530

Edmonds, M., Gerlach, T.M., 2007. Vapor segregation and loss in basaltic melts, Geology, 35(8):751–754, doi: 10.1130/G23464A.1

Fagents, S.A., Greeley, R., 2001. Factors influencing lava-substrate heat transfer and implications for thermomechanical erosion. Bull. Volcanol., 62:519–532, doi: 10.1007/s004450000113

Fedotov, S.A., Chirkov A.M, Gusev N.A., Kovalev, G.N, Slezin, Y.B., 1980. The large fissure eruption in the region of Plosky Tolbachik volcano in Kamchatka, 1975–1976. Bull. Volcan., 43:47–60, doi: 10.1007/BF02597610

Fiske R.S., Kinoshita W.T., 1969. Inflation of Kīlauea volcano prior to its 19 67–1968 eruption. Science, 165(3891):341–9

Fiske, R.S., Koyanagi, R.Y., 1968. December 1965 eruption of Kilauea volcano, Hawaii. US Geol. Surv. Prof. Pap. 607

Fiske, R.S., Rose, T.R., Swanson, D.A., Champion, D.E., McGeehin, J.P., 2009. Kulanaokuaiki Tephra (ca. AD400–1000): newly recognized evidence for highly explosive eruptions at Kīlauea Volcano, Hawai'i. Geol. Soc. Am. Bull., 121:712–728

Fornari, D., Tivey, M., Hans, S., Perfit, M., Yoerger, D., Bradley, A., Edwards, M., Haymon, R., Scheirer, D., Von Damm, K., Shank, T., Soule, A., 2004. Submarine Lava Flow Emplacement at the East Pacific Rise 9° 50´N: Implications for Uppermost Ocean Crust Stratigraphy and Hydrothermal Fluid Circulation. AGU Geophys. Monograph, 148, doi: 10.1029/148GM08

Frey, F.A., Rhodes, J.M.,1983. Intershield geochemical differences among Hawaiian volcanoes: implications for source compositions, melting process and magma ascent paths. Phil. Trans. Roy. Soc., 342(1663):121–136, doi: 10.1098/rsta.1993.0009

Gerlach, T.M., Graeber, E.J.,1985. Volatile budget of Kilauea volcano. Nature, 313:273–277, doi:10.1038/313273a0

Gerlach, T.M., McGee, K.A., Elias, T., Sutton, A.J., Doukas, M.P., 2002. Carbon dioxide emission rate of Kīlauea Volcano: Implications for primary magma and the summit reservoir. J. Geophys. Res., 107:2189–2204, doi: 10.1029/2001JB000407

Giberti, G., Wilson, L., 1990. The influence of geometry on the ascent of magma in open fissures. Bull. Volcanol. 52:515–521

Goehring, L., Morris, S.W., 2008. Scaling of columnar joints in basalt. J. Geophys. Res., 113:B10203, doi: 10.1029/2007JB005018

Goehring, L., Morris, S.W., Lin, X., 2006. Experimental investigation of the scaling of columnar joints. Phys. Rev. E., 74(3):036115–036127, doi: 10.1103/PhysRevE.74.036115

Gonnermann, H.M., Manga, M., 2007. The fluid mechanics inside a volcano. Ann. Rev. Fluid Mech., 39:321–356

Gonnermann, H.M., Houghton, B.F., 2012. Magma degassing during the Plinian eruption of Novarupta, Alaska, 1912. Geochem. Geophys. Geosystems, doi:10.1029/2012GC004273

Grant, J.V., Kattenhorn, S.A., 2004. Evolution of vertical faults at an extensional plate boundary, southwest Iceland. J. Structural Geol., 26:537–557

Greeley, R., Hyde, J.H., 1972. Lava tuves of the Cave basalt, Mount St. Helens, Washinton. Geol. Soc. Am. Bull., 83:2397–2418

Greeley, R., Fagents, S.A., Harris, R.S., Kadel, S.D., Williams, D.A., Guest, J.E., 1998. Erosion by flowing lava: field evidence, J. Geophys. Res., 103:27325–27346.

Gudmundsson, A., 2003. Surface stresses associated with arrested dykes in rift zones, Bull. Volcanol., 65:606–619

Hardee, H.C., 1987. Replenishment rates of crustal magma and their bearing on potential sources of thermal energy. J. Volcanol. Geotherm. Res., 28(3–4):275–296

Head, J., Wilson, L., 1989. Basaltic pyroclastic eruptions: influence of gas=release patterns and volume fluxes on fountain structure, and the formation of cinder cones, spatter cones, rootless flows, lava ponds, and lava flows. J. Volcanol. Geotherm. Res., 37(3–4): 261–271, doi: 10.1016/0377-0273(89)90083-8

Heliker, C., Swanson, D.A., Takahashi, T.J., 2003. The Pu‘u ‘Ō‘ō–Kūpaianaha Eruption of Kīlauea Volcano, Hawaiʻi: The First 20 Years. US Geol. Surv. Prof. Pap. 1676

Holcomb, R.T., 1987. Eruptive History and Long-Term Behavior of Kilauea Volcano. In: Decker, R.W., Wright, T.L., Stauffer, P.H. (Eds): Volcanism in Hawaii, US Geol. Surv. Prof. Pap., 1350(1):261–350

Holland, M., Urai, J.L., Martel, S.J., 2006. The internal structure of fault zones in basaltic sequences. Earth Plant. Sci. Lett., 246(1–2):301–315

Hon, K., Kauahikaua, J., Denlinger, R., Mackay, K., 1994. Emplacement and inflation of pāhoehoe sheet flows: Observations and measurements of active lava flows on Kilauea Volcano, Hawaii. Geol. Soc. Am. Bull., 106:351–370, doi:10.1130/0016-7606(1994)106<0351:EAIOPS>2.3.CO;2

Houghton, B.F., Wilson, C.J.N., 1989. A vesicularity index for pyroclastic deposits. Bull. Volcanol., 51(6):451–461, doi: 10.1007/BF01078811

Hui, H.J., Zhang, Y.X., 2007. Toward a general viscosity equation for natural anhydrous and hydrous silicate melts. Geochim. Cosmochim. Acta., 71:403–416.

Jaupart, C., 1996. Physical models of volcanic eruptions. Chem. Geol., 28(1–4):217–227

Jaupart, C., Vergniolle, S., 1988. Laboratory models of Hawaiian and Strombolian eruptions. Nature, 331:58–60, doi:10.1038/331058a0

Jaupart, C., Vergniolle, S., 1989. The generation and collapse of a foam layer at the roof of a basaltic magma chamber. J. Fluid Mech., 203:347–380, doi: 10.1017/S0022112089001497

Jenness, M.H., Clifton, A.E., 2009 . Controls on the geometry of a Holocene crater row: a field study from southwest Iceland, Bull. Volcanol., 71:715–728

Johnson, D.J., 1995. Molten core model for Hawaiian rift zones. J. Volcanol. Geotherm. Res., 66:27–35

Johnson, M.C., Anderson, A.T., Rutherford, M.J., 1994. Pre-Eruptive Volatile Contents of Magmas, In: Carroll, M.R., Holloway, J.R., (Eds.), Volatiles in Magmas. Rev. Min., 30:281–330

Kamenetsky, V.S., Pompilio, M., Metrich, N., Sobolev, A.V., Kuzmin, D.V., Thomas, R., 2007. Arrival of extremely volatile-rich high-Mg magmas changes explosivity of Mount Etna. Geology, 35:255–258

Kauahikaua, J., Cashman, K.V., Mattox, T.N., Heliker, C.C., Hon, K.A., Mangan, M.T., Thornber, C.R., 1998. Observations on basaltic lava streams in tubes from Kilauea volcano, Hawaii. J. Geophys. Res., 103:27303–27324

Klug, C., Cashman, K., Bacon, C., 2002. Structure and physical characteristics of pumice from the climactic eruptions of Mount Mazama (Crater Lake) Oregon. Bull. Volcan., 64(7):486–501, doi:10.1007/s00445-002-0230-5

La Delfa, S., Patane, G., Clocchiatti, R., Joron, J.L., Tanguy, J.C., 2001. Activity of Mount Etna preceding the February 199 fissure eruption: inferred mechanism from seismological and geochemical data. J Volcanol. Geotherm. Res., 105(1–2):121–139

Lautze, N.C., Houghton, B.F., 2005. Physical mingling of magma and complex eruption dynamics in the shallow conduit at Stromboli volcano, Italy. Geology, 33(5):425-428, doi: 10.1130/G21325.1

Lautze, N.C., Houghton, B.F., 2006. Linking variable explosion style and magma textures during 2002 at Stromboli volcano. Bull. Volcanol. 69:445–460

Lautze, N., Houghton, B.F., 2007. Linking variable explosion style and magma textures during 2002 at Stromboli volcano, Italy. Bull. Volcanol., 69(4):445–460, doi:10.1007/s00445-006-0086-1.

Lejeune, A.M., Richet, P., 1995. Rheology of crystal-bearing silicate melts: an experimental study at high viscosities. J. Geophys. Res., 100(B3):4215–4229, doi: 10.1029/94JB02985

Llewellin, E.W., Manga, A., 2005. Bubble suspension rheology and the implications for conduit flow. J Volcanol. Geotherm. Res., 143(1–3):205–217

Lockwood J.P., Tilling, R.I., Holcomb, R.T., Klein, F., Okamura, A.T., Peterson, D.W., 1999. Magma Migration and resupply during the 1974 summit eruptions of Kilauea Volcano, Hawai'i. US. Geol. Surv. Prof. Pap. 1613:1–43

Macdonald, G.A., Eaton, J.P., 1957. Hawaiian volcanoes during 1954. US. Geol. Surv. Bull., 1061(B):17–72

Macdonald, G.A., Abbott, A.T., Peterson, F.L., 1983. Volcanoes in the sea: the geology of Hawaii, 2nd edn. University of Hawaii Press, Honolulu

Mangan, M.T., Cashman, K.V., 1996. The structure of basaltic scoria and reticulite and inferences for vesiculation, foam formation, and fragmentation in lava fountains. J. Volcanol. Geotherm. Res., 73(1–2):1–18

Mangan, M.T., Cashman, KV., Newman, S., 1993. Vesiculation of basaltic magma during eruption. Geology, 21(2):157–160, doi: 10.1130/ 0091-7613 021<0157:VOBMDE> 2.3.CO;2

Manga, M., Castro, J., Cashman, K., Lowenberg, M., 1998. Rheology of bubble bearing magmas. J Volcanol. Geotherm. Res., 87:15–28

Métrich, N., Allard, P., Spilliaert, N., Andronico, D., Burton, M., 2004. 2001 flank eruption of the alkali- and volatile-rich primitive basalt responsible for Mount Etna's evolution in the last three decades. Earth Planet. Sci. Lett., 228:1–17, doi: 10.1016/ j.epsl.2004.09.036

Mitchell, K.L., 2005. Coupled Conduit flow and shape in explosive volcanic eruptions. J. Volcanol. Geotherm. Res., 143(1–3):187–203 doi: 10.1016/j.volgeores.2004.09.017

Moritra, P., Gonnermann, H.M., Houghton, B.F., Giachetti, T., 2013. Relating vesicles shapes in pyroclasts to eruption styles. Bull Volcanol., 75(2):691

Moore JG, Koyanagi RY (1969) The Octover 1963 eruption of Kilauea volcano, Hawaii. US. Geol. Surv. Prof. Pap. 614–c

Montgomery-Brown, E.K., Sinnett, D.K., Poland, M., Segall, P., Orr, T., Zebker, H., Miklius, A., 2010. Geodetic evidence for en echelon dike emplacement and concurrent slow slip during the June 2007 intrusion and eruption of Kilauea volcano, Hawaii. J. Geophys. Res., 115:B07405, doi: 10.1029/2009JN006658

Moore, J.G., Koyanagi, R.Y., 1969. The October 1963 eruption of Kīlauea volcano, Hawaii. US. Geol. Surv. Prof. Pap. 614–c

Moore, J.G., Phillips, R.L., Grigg, R.W., Peterson, D.W., Swanson, D.A., 1973. Flow of lava into the sea, 1969–1971, Kīlauea Volcano, Hawaii. Geol. Soc. Am. Bull., 84(2):537–546, doi: 10.1130/0016-7606(1973)84<537:FOLITS>2.0CO;2

Moore, J.G., Clague, D.A., 1992. Volcano Growth and Evolution of the Island of Hawaii. GSA Bull., 104(11):1471–1484, doi: 10.1130/0016-7606(1992)

Morris, AR, Anderson, F.S., Moughinis-Mark, P.J., Haldermann, A.F.C., Brooks, B.A., Foster, J., 2008. Roughness of Hawaiian volcanic terrains. J. Geophys. Res., 113:E12007, doi: 10.1029/2008JE003079

Moune, S., Sigmarsson, O., Schiano, P., Thordarson, T., Keiding, J.K., 2012. Melt inclusion constraints on the magma source of Eyjafjallajokull 2012 flank eruption. J. Geophys. Res., 117:B00C07, doi:10.1029/2011JN008718

Namiki, A., Manga, M., 2005. Response of a bubble bearing viscoelastic fluid to rapid decompression: Implications for explosive volcanic eruptions. Earth Planet. Sci. Lett., 236:269–284

Namiki, A., Manga, M., 2006. Influence of decompression rate on the expansion velocity and expansion style of bubbly fluids. J. Geophys. Res., 111:B11208, doi:10.1029/2005JB004132

Namiki, A., Manga, M., 2008. Transition between fragmentation and permeable outgassing of low viscosity magmas. J. Volcanol. Geotherm. Res., 169:48–60

Pal, R., 2003. Rheological behavior of bubble-bearing magmas. Earth Planet. Sci. Lett., 207: 165–179

Papale, P., 1999. Strain-induce magma fragmentation in explosive eruptions. Nature, 397:425–428.

Papale, P., 2005. Determination of total H2O and CO2 budgets in evolving magmas from melt inclusion data, J. Geophys. Res., 110:B03208, doi: 10.1029/2004JB003033

Papale, P., Moretti, R., Barbato, D., 2006. The compositional dependence of the saturation surface of H_20+CO_2 fluids in silicate melts. Chem. Geol., 229:78–95

Parcheta, C., Houghton, B.F., Swanson, D.A., 2012. Hawaiian Fissure Fountains 1: decoding deposits - episode 1 of the 1969–1974 Mauna Ulu eruption, Bull. Volcan., 74(7):1729–1743, doi: 10.1007/s00446-012-0621-1

Parcheta, C., Houghton, B.F., Swanson, D.A., 2013. Contrasting patterns of vesiculation in low, intermediate, and high Hawaiian fountains: A case study of the 1969 Mauna Ulu eruption, J. Volcanol. Geotherm. Res., 255:79–89, doi: 10.1016/j.jvolgeores.2013.01.016

Parfitt, E.A. 2004. A discussion of the mechanisms of explosive basaltic eruptions. J. Volcanol. Geotherm. Res., 134(1–2):77–107, doi: 10.1016/j.jvolgeores.2004.01.002

Parfitt, E. A., Wilson, L., 1994. The 1983–86 Pu'u 'O'o eruption of Kilauea Volcano, Hawaii: a study of dike geometry and eruption mechanisms for a long-lived eruption. J. Volcanol. Geotherm. Res., 59(3):179–205

Parfitt, E.A., Wilson, L., 1995. Explosive volcanic eruptions—IX. The transition between Hawaiian-style lava fountaining and Strombolian explosive activity. Geophys. J. Int., 121(1):226–232

Parfitt, E.A., Wilson, L., Neal, C.A., 1995. Factors influencing the height of Hawaiian lava fountains: implications for the use of fountain height as an indicator of magma gas content. Bull. Volcan., 57(6):440–450, doi: 10.1007/BF00300988

Petcovic, H.L., Dufek, J.D., 2005. Modeling magma flow and cooling in dikes: implication sfor emplacement of Columbia River flood basalts. J. Geohpys. Res., 110:B10201, doi:10.1029/2004JB003432

Peterson, D.W. 1969. Kilauea volcano eruption. Bull. Volcanol. Erupt. Volcanol. Soc. Jap., 10:11

Peterson, D.W., Swanson, D.A., 1974. Observed formation of lava tubes during 1970–1971, Kīlauea volcano, Hawaii. Stud. Speleol., 2:209–222

Peterson, D.W., Holcomb, R.T., Tilling, R.I., Christiansen, R.L., 1994. Development of lava tubes in the light of observations at Mauna Ulu, Kīlauea Volcano, Hawaii. Bull. Volcanol., 56:343–360

Pietruszka, A.J., Garcia, M.O., 1999. A Rapid Fluctuation in the Mantle Source and Melting History of Kilauea Volcano Inferred from the Geochemistry of its Historical Summit Lavas (1790–1982). J. Pet., 40(8):1321–1342, doi: 10.1093/petroj/40.8.1321

Polacci, M., Corsaro, R.A., Andronico, D., 2006. Coupled textural and compositional characterization of basaltic scoria: Insights into the transition from Strombolian to fire fountain activity at Mount Etna, Italy. Geology, 34(3):201–204, doi: 10.1130/ G22318.1

Poland, M.P., Miklius, A., Sutton, A.J., Thornber, C.R., 2012. A mantle-driven surge in magma supply to Kilauea volcano during 2003–2007. Nature Geoscience, 5:295–300, doi: 10.1038/NGEO1426

Pollard, D.D., 1987. Elementary fracture mechanics applied to the structural interpretation of dykes. In: Halls, H.C., Fahrig, W.F., (Eds.), Mafic Dike Swarms, Geol. Assoc. Canada Special Pap. 34:5–24

Pollard, D.D., Muller, O.H., 1976.The effect of gradients in regional stress and magma pressure on the form of sheet intrustions in cross section. J. Geophys. Res., 81:975–984

Pollard, D.D., Aydin, A., 1988. Progress in understanding jointing over the past century. Geol. Soc. Am. Bull., 100(8):1181–1204, doi: 10.1130/0016-7606(1988)100<1181:PIUJOT>2.3.CO;2

Pollard D.D., Segall, P., Delaney, P.T., 1982. Formation and interpretation of dilatants echelon cracks. Geol. Soc. Am. Bull. 93(12):1291–1303, doi: 10.1130/0016-7606(1982)93<1291:FAIODE>2.0.CO;2

Pyle, D.M., 1989. The thickness, volume, and grainsize of tephra fall deposits. Bull Volcanol 51(1):1–15

Richter, D.H., Eaton, J.P., Murata, K.J., Ault, W.U., Krivoy, H.L., 1970. Chronological narrative of the 1959–60 eruption of Kilauea Volcano, Hawaii, US. Geol. Surv. Prof. Pap. 537–E:E1–E73

Ripepe, M., Marchetti, E., Ulivieri, G., Harris, A., Dehn, J., Burton, M., Caltabiano, T., Salerna, G., 2005. Effusive to explosive transition during the 2003 eruption of Stromboli volcano. Geology, 33(5):341–344, doi: 10.1130/G21173.1

Ryan, M.P., Sammis, C.G., 1978. Cyclic fracture mechanisms in cooling basalt. Geol. Soc. Am. Bull., 89(9):1295–1308, doi:10.1130/0016-76-6(1978)89<1295:CFMICB>2.0.CO;2

Saar, M.O., Manga, M., Cashman, K.V., Fremouw, S., 2001. Numerical models of the onset of yield strength in crystal-melt suspensions. Earth Planet. Sci. Lett., 187:367–379

Sable, J., Houghton, B.F., Del Carlo, P., Coltelli, M., 2006. Changing conditions of magma ascent and fragmentation during the Etna 122 BC basaltic plinian eruption: evidence from clast microtextures. J. Volcan. Geotherm. Res., 158:333–354

Sable, J.E., Houghton, B.F., Wilson, C.J.N., Carey, R.J., 2007. Complex proximal sedimentation from Plinian plumes: the example of Tarawera 1886. Bull. Volcanol., 69:89–103

Sable, J.E., Houghton, B.F., Wilson, C.J.N., Carey, R.J., 2009. Eruption mechanisms during the climax of the Tarawera 1886 basaltic Plinian eruption inferred from microtextural characteristics of the deposits. In: Thordarson, T., Self, S., Larsen, G., Rowland, S.K., Hoskuldsson, A. (Eds.), Studies in Volcanology: The Legacy of George Walker. Special Publications of IAVCEI, Geological Society, London, 2:129–154

Sahagian, D.L., Proussevitch, A.A., 1998. 3D particle size distributions from 2D observations: stereology for natural applications. J. Volcanol. Geotherm. Res., 84:173–196

Sharp, W.D., Clague, D.A., 2006. 50–Ma initiation of Hawaiian-Emperor bend records major change in Pacific Plate motion. Science, 313(5791):1281–1284. doi: 10.1126/science.1128489

Shea, T.,Houghton,B.F.,Gurioli, L., Cashman, K.V.,Hammer, J.E.,Hobden, B.J., 2010. Textural studies of vesicles in volcanic rocks: an integrated methodology. J. Volcanol. Geotherm. Res., 190:271–289

Sigurdsson, H., 2000. Introduction In: Sigurdsson, H., Houghton, B.F., McNutt, S.R., Rymer, H., Stix, J. (Eds.), Encyclopedia of Volcanoes. Academic Press, San Diego, pp 1–13

Slezin, Y., 2003. The mechanism of volcanic eruptions (a steady state approach). J. Volcanol. Geotherm. Res., 122(1–2):7–50

Sommer, E., 1969. Formation of fracture "lances" in glass. Eng. Fract. Mech., 1:539–546

Spieler, O., Kennedy, B., Kueppers, U., Dingwell, D.B., Scheu, B., Taddeucci, J., 2004. The fragmentation threshold of pyroclastic rocks. Earth Planet. Sci. Lett., 226:139–148

Spilliaert, N., Allard, P., Métrich, N., Sobolev, A.V., 2006. Melt inclusion record of the conditions of ascent, degassing, and extrusion of volatile-rich alkali basalt during the powerful 2002 flank eruption of Mount Etna (Italy). J. Geophys. Res., 111:B04203, doi: 10.1029/2005JB003934

Stearns, H.T., 1946. Geology of the Hawaiian Islands. Hawaii Division of Hydrography. Honolulu, Hawaii

Stevens, N.F., Murray, J.B., Wadge, G., 1997. The volume and shape of the 1991–1993 lava flow field at Mount Etna, Sicily. Bull. Volcanol., 58(6):449–454

Stovall, W.K., Houghton, B.F., Harris, A.J.L., Swanson, D.A., 2008. A frozen record of density-driven crustal overturn in lava lakes: the example of

Kilauea Iki, 1959. Bull. Volcanol. 71(3):313–318, doi: 10.1007/s00445-008-0225-y

Stovall, W.K., Houghton, B.F., Gonnermann, H., Fagents, S.A., Swanson, D.A., 2011. Eruption dynamics of Hawaiian-style fountains: the case study of episode 1 of the Kīlauea Iki 1959 eruption. Bull. Volcanol., 73(5):511–529

Stovall, W.K., Houghton, B.F., Hammer, J., Fagents, S.A., Swanson, D.A., 2012. Vesiculation of high fountaining Hawaiian eruptions: episodes 15 and 16 of 1959 Kīlauea Iki. Bull. Volcan., 74(2):441–455

Sumner, J.M., 1998. Formation of clastogenic lava flows during fissure euption and scoria cone collapse: the 1986 eruption of Izu-Oshima volcano, eastern Japan. Bull. Volcanol. 60(3):195–212

Swanson, D.A., 1972. Magma supply rate at Kīlauea Volcano 1952–1971. Science, 175(4018):169–170

Swanson, D.A., 1974. Pahoehoe flows from the 1969–1971 Mauna Ulu Eruption, Kīlauea Volcano, Hawaii. Geol. Soc. Am. Bull., 84(2):615–626. doi: 10.1130/0016-7606(1973)84<615:PFFTMU>2.0.CO;2

Swanson, D.A., Duffield, D.A., Jackson, D.B., Peterson, D.W., 1979. Chronological narrative of the 1969–1971 Mauna Ulu Eruption of Kilauea volcano, Hawaii, US. Geol. Surv. Prof. Pap. 1056

Swanson, D.A., Jackson, D.B., Duffield, D.A., Peterson, D.W., 1971. Mauna Ulu eruption, Kilauea volcano. Geotimes, 16(5):12–16

Swanson, D.A., Rose, T.R., Fiske, R.S., McGeehin, J.P., 2012. Keanakako'i Tephra produced by 300 years of explosive eruptions following collapse of Kīlauea 's caldera in about 1500 CE. J. Volcanol. Geotherm. Res., 215–216:8–25, doi: 10.1016/j.jvolgeores.2011.11.009

Taddeucci, J., Spieler, O., Kennedy, B., Pompilio, M., Dingwell, D. B., Scarlato, P., 2004. Experimental and analytical modeling of basaltic ash explosions at Mount Etna, Italy, 2001. J. Geophys. Res., 109:B08203, doi: 10.1029/2003JB002952

Tarduno, John A.; et al. 2009. The Bent Hawaiian-Emperor Hotspot Track: Inheriting the Mantle Wind. Science, 324:50–53, doi: 10.1126/science.1161256

Tilling, R. I., 1987. Fluctuations in surface height of active lava lakes during 1972–1974 Mauna Ulu Eruption, Kilauea Volcano, Hawai'i. J. Geophys. Res., 92(B13):13721–13730, *doi: 10.1029/JB092iB13p13721.*

Tilling, R.I., Dvorak, 1993. Anatomy of a basaltic volcano. Nature, 363:125–133

Tilling, R.I., Christiansen, R.L., Duffield, W.A., Endo, E.T., Holcomb, R.T., Koyanagi, R.Y., Peterson, D.W., Unger, J.D., 1987. The 1972–1974 Mauna Ulu eruption, Kilauea Volcano: an example of quasi steady-state magma transfer. US. Geol. Surv. Prof. Pap. 1350:405–469

Toramaru, A., 1995. Numerical study of nucleation and growth of bubbles in viscous magmas. J. Geophys. Res., 100(B2):1913–1931, doi: 10.1029/94JB02775

Valentine, G.A., Krogh, K.E.C., 2006. Emplacement of shallow dikes and sills beneath a small basaltic volcanic center–the role of pre-existing structure (Paiute Ridge, southern Nevada, USA). Earth Planet. Sci. Lett., 246:217–230

Vergniolle, S., Jaupart, C., 1986. Separated two-phase flow and basaltic eruptions. J. Volcan. Geotherm. Res., 91:12842–1286

Vergniolle, S., Jaupart, C., 1990. Dynamics of degassing at Kīlauea Volcano, Hawaii. J. Geophys. Res., 95(B3):2793–2809

Vergniolle, S., Mangan, M.T., 2000. Hawaiian and Strombolian eruptions. In: Sigurdsson, H., Houghton, B.F., McNutt, S.R., Rymer, H., Stix, J. (Eds), Encyclopedia of Volcanoes. Academic Press, San Diego, pp 447–462

Walker, G.P.L., 1973. Explosive volcanic eruptions—a new classification scheme. Int. J. Earth. Sci., 62(2):431–446, doi: 10.1007/BF01840108

Wallace, P.J., 2005. Volatiles in subduction zone magma: concentrations and fluxes based on melt inclusion and volcanic gas data. J. Volcanol. Geotherm. Res., 21:61–78

Webb, S.L., Dingwell, D.B., 1990. The onset of non-newtonian rheology of silicate melts–a fiber elongation study. Phys. Chem. Min., 17:125–132

Williams, D.A., Kadel, S.D., Greeley, R., Lesher, C.M., Clynne, M.A., 2004. Erosion by flowing lava: geochemical evidence in the Cave Basalt, Mount St. Helens, Washington. Bull. Volcanol., 66:168–181, doi: 10.1007/s00445-003-0301-2

Wilson, J.T., 1963. A possible origin of the Hawaiian Islands. Canadian J. Phys., 41:863–870, doi: 10.1139/p63-094.

Wilson, L., 1980. Relationships between pressure, volatile contents, and ejecta velocity in three types of volcanic explosions. J. Volcanol. Geotherm. Res., 8(2–4):297–313

Wilson, L., 1999. Explosive volcanic eruptions–X. The influence of pyroclast size distributions and released maga gas contents on the eruption velocities of pyroclasts and gas in Hawaiian and Plinian eruptions. Geophys. J. Int., 136(3):609–619, doi: 10.1046/j.1365-246x.1999.00750.x

Wilson, L., Head, J., 1981. Ascent and eruption of basaltic magma on the Earth and Moon. J. Geophys. Res., 86(B4):2871–3001

Wilson, C.J.N., Houghton, B.F., 2000. Pyroclastic transport and deposition. In: Sigurdsson, H., Houghton, B.F., McNutt, S.R., Rymer, H., Stix, J. (Eds.), Encyclopedia of volcanoes. Academic, San Diego, pp 545–554

Wolfe, C.J., Solomon, S.C., Laske, G., Collins, J.A., Detrick, R.S., Orcutt, J.A., Bercovici, D., Hauri, E.H., 2011. Mantle P-wave velocity structure beneath the Hawaiian hotspot. Earth Planet. Sci. Letts., 303:267–280, doi: 10.1016/j.epsl2011.01.004

Wolfe, E.W., Neal, C.A., Bamks, N.G., Duggan, T.J., 1988. The Puʻu ʻŌʻō eruption of Kilauea volcano, Hawaii: episodes 1 through 20, January 3, 1981 through June 8, 1984. US. Geol. Surv. Prof. Pap. 1463

Wolfenden, E., Ebinger, C., Yirgu, G., Deino, A., Ayalew, D., 2004. Evolution of the northern Main Ethiopian rift: Birth of a triple junction, Earth Planet. Sci. Letts., 224:213–228

Wolff, J.A., Sumner, J.M., 2000. Lava fountains and their products. In: Sigurdsson, H., Houghton, B.F., McNutt, S.R., Rymer, H., Stix, J. (Eds.), Encyclopedia of Volcanoes. Academic Press, San Diego, pp. 321–330

Wylie, J.J., Helfrich, K.R., Dade, B., Lister, J.R., Salzig, J.F., 1999. Flow localization in fissure eruptions. Bull. Volcanol., 60(6):432–440

Yang, x., Davis, P.M., Delaney, P.T., Okamura, A.T., 1992. Geodetic analysis of dike intrusion and motion of the magma reservoir beneath the summit of Kilauea Volcano, Hawaii: 1970–1985. J. Geophys. Res., 97:3305–3324

Zhang, X.Y., 1999. A criterion for the fragmentation of bubbly magma based on brittle failure theory. Nature, 402:648–650